Polarisation Observables in Neutral Pion Photoproduction with MAMI

Simon Gardner

A thesis presented for the degree of
Doctor of Philosophy

Nuclear Physics Group
School of Physics and Astronomy
University of Glasgow

September 2016

For Lizzy

Polarisation Observables in Neutral Pion Photoproduction with MAMI

Simon Gardner

Submitted for the degree of Doctor of Philosophy
September 2016

Abstract

This thesis presents new high statistics measurements of polarisation observables in neutral pion photoproduction from experiments carried out with the Crystal Ball at the Mainzer Microtron (MAMI) in Mainz. The polarisation observable Σ has been measured in the $\gamma p \to \pi^0 p$ reaction in the region between the $\Delta(1232)$ and second resonance region. Measurements of observables Σ, I^s and I^c in the $\gamma p \to 2\pi^0 p$ reaction have been made from the $2\pi^0$ threshold, a lower energy than previously measured.

All measurements produced for this thesis have been sent to partial wave analysis groups where they will be used to provide constraints to their models. In particular, the $2\pi^0$ measurements are expected to have an impact on our understanding of the poorly constrained properties of the N(1440) resonance, such as the branching ratios of its decay through intermediate meson or Δ pathways.

The ${}_s\mathcal{P}lot$ technique has been used for the first time in photoproduction experiments with advantages over other techniques discussed. The development of the technique for such analysis as this will be key for the extraction of many observables from future measurements.

Declaration

The work in this thesis is based on research carried out at the Nuclear Physics Group, School of Physics & Astronomy, University of Glasgow, UK. No part of this thesis has been submitted elsewhere for any other degree or qualification and it all my own work unless referenced to the contrary in the text.

Acknowledgements

I am indebted to a many people for their support throughout my PhD and cannot acknowledge everyone personally here.

Without the supervision provided by Ken, Derek, Douglas and David Hamilton I wouldn't have got far. The support they provided was invaluable in building the project into this interesting thesis. I'm know there were many days my knocking on doors at 16:55 was less than ideal but I was always met with friendly guidance.

I have to thank my office cohabitees over the years; Stef, Bruno, Roddy and Kieran for keeping me in a reasonable balance between sanity and chair spinning folly. Other activities such as Gashball^{TM} and amassing large coffee debts helped make the group working environment both comfortable and stimulating.

Running through the forests, mountains and bogs of Scotland provided a necessary reprise from work. I need to thank the Glasgow orienteering community who have helped and supported both my personal endeavours and the formation of the university club.

As ever my family have been my family, providing probably normal family type support. My mother, Nicola, selflessly suffered the reading of my mistake riddled first draft. My fiancé Lizzy has without a doubt been the most caring and encouraging influence in my life having helped me through darker days with great patience and been my adventure buddy, alarm clock, supplier of cheese and constant best friend.

Cheers.

Contents

List of Figures

List of Tables

Chapter 1

Introduction

Beam asymmetry measurements of the $\gamma p \rightarrow \pi^0 p$ and $\gamma p \rightarrow 2\pi^0 p$ reaction channels have been made using the Crystal Ball detector at the Mainzer Microtron (MAMI) in Mainz. The results have high statistical precision and have provided valuable input to current models which seek to describe the spectrum of nucleon resonances, and ultimately to understand the strong force which binds hadronic matter. This chapter explains the motivation for this work, building from a historic perspective to our modern understanding of hadron physics.

1.1 Nucleons

Protons and neutrons, along with electrons, are the core components from which atoms are formed. The description of the electromagnetic force, which governs charge interactions between particles, is believed to be complete. However the strong force, which guides the interactions of protons, neutrons and their quark components, is relatively poorly understood, with models unable to accurately predict experimental measurements. The work described here aims to expand our knowledge of the strong force by contributing to the world pool of data on the proton resonance spectrum.

Protons were discovered in the Rutherford scattering experiment in 1919[1] where

atoms were determined to have a non-uniform charge distribution, with the positive charge concentrated at the centre. The neutron was not detected until 1932[2], when it was determined to have the same mass as the proton but with a neutral charge.

The similar properties of the proton and neutron do not end with their masses, the strength of interaction between the particles was determined to be independent of the charge states. This led to postulations that protons and neutrons were the same particle, called the nucleon, in a different charge state and the quantum number *isospin* (I) was introduced to differentiate particles described this way[3].

The next few decades welcomed an explosion of new particle discoveries, which seemed to require more quantum numbers to describe their properties. The baryon quantum number separates baryons (B=1) from mesons (B=0), while the strangeness quantum number (S) accounts for particles with a *strangely* longer lifetime[4, 5]. The quantum number *hypercharge* (Y) is a sum of the baryon and strangeness quantum numbers.[1] An order was given to the collection of discovered particles, described by the *Eightfold Way*[6, 7], where particles with the same spin and parity were grouped together.

The organisation of the Eightfold Way can be described by SU(3) symmetry formalism, this lead to the interpretation that hadronic particles could be formed of three quarks, now known as the up (u), down (d) and strange (s) quarks[8, 9]. Diagrams in figure 1.1 show the two multiplets of particles relating to particles made of the light quarks where the constituent quark spins are aligned and where one of the quarks spins is anti-aligned.

[1] With understanding of the quark components of hadrons and discovery of the heavy quarks the definition of hypercharge was revised to be Y=B+S+C+B'+T. Where S, C, B' and T refer to the number of strange, charm, bottom and top quarks respectively forming the hadron.

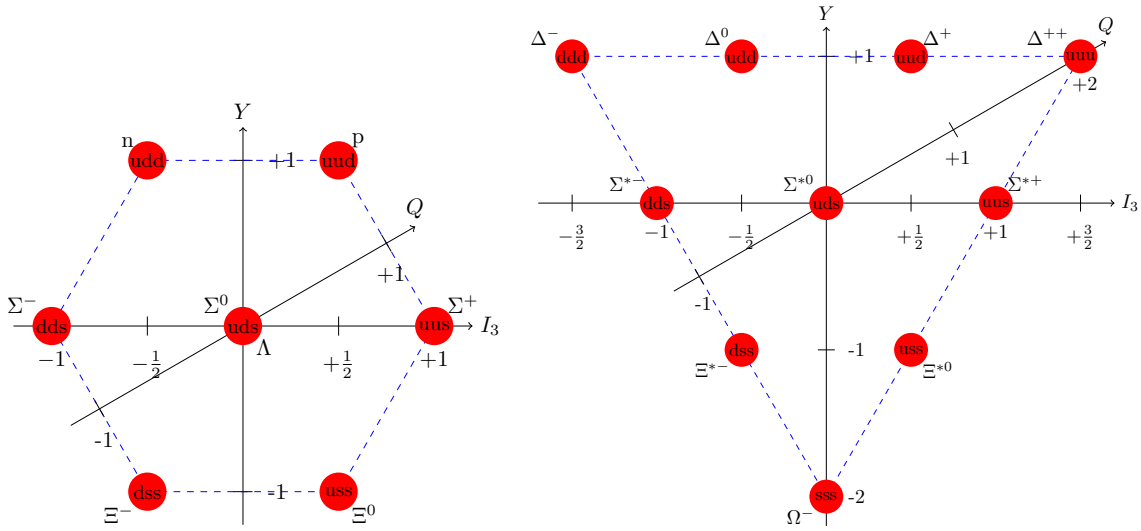

(a) $J^P = \frac{1}{2}^+$ Baryon Octet (b) $J^P = \frac{3}{2}^+$ Baryon Decuplet

Figure 1.1: Multiplet diagrams showing the organisation of baryons. The * in the decuplet diagram represents an excited state of the particle. Three axes are shown where Q is the charge of the baryon, Y is the hypercharge and I_3 is the isospin projection onto the z-axis.

Nucleons are the only stable hadrons found in nature where the neutron will decay unless found in a stable atomic nucleus. Consisting of three valence quarks the proton is formed from *uud* and the neutron formed from *ddu*. As with any bound system the nucleon can be excited, quark model predictions anticipate a series of resonant states relating to the excitation of different degrees of freedom.

1.2 N^* and Δ Resonances

The work described in this thesis aims to develop our understanding of the nucleon resonance spectrum. Early approaches to modelling the nucleon relied on the symmetric quark model where the three quarks were given identical freedoms. This model predicts harmonic resonances from a $SU(6) \bigotimes O(3)$ symmetry[10, 11, 12], which match the measured properties of the resonances with low invariant masses. In the higher invariant mass regime there are many resonances predicted by the model which have not been experimentally verified, these are termed *missing resonances*. A model where the nucleon constituent quarks are modelled as a tightly

Particle	Mass (MeV/c^2)	Constituents	Constituents mass (MeV^2)
u	2.3	NA	NA
d	4.8	NA	NA
proton	938	uud	9.4
neutron	939	ddu	11.9

Table 1.1: Quark and nucleon masses.

bound pair and one free to resonate, called the diquark model[13, 14], was also able to explain certain measurements, however still not fully describe the observations[15, 16]. The *missing resonance* problem remains a main focus of the nucleon spectroscopy field.

Modern nucleon models have progressed beyond the symmetric quark model, able to better match experimental measurements[17]. It is now understood that nucleons are formed from more than just the three valence quarks, with additional quark-antiquark pairs and gluons forming a sea of particles. As shown in table 1.1, the mass of the valence quarks only makes up about 1% of the nucleon mass with the remainder needing to be accounted for by the interactions of the sea of particles.

Most of the original measurements of resonances were from experiments scattering $\pi^{\pm}$ beams off protons. The hadronic interaction of the $\pi^{\pm}$N was predicted to couple only weakly to some resonances making them impossible to identify from the cross section of resonances with larger coupling amplitudes. Experiments which probed the nucleon with high energy photon beams were proposed in order to circumvent this resonance bias of $\pi^{\pm}$ beams, and determine the electromagnetic transition amplitudes of the γN reaction. Advances in accelerator technology in the 1980s allowed the production of continuous electron beams which in turn were used to generate continuous stable high energy photon beams; along with the development of 4π detector systems, conducting γN (photoproduction) experiments became feasible.

Photoproduction experiments have become the basis of many current and future experimental programs and are seen as necessary to furthering our understanding of the nucleon resonance spectrum. However, they are not without complications - for instance, the scattering cross section of the γN reaction is of the order 10^{-3} compared to that of the $\pi^{\pm}$N reaction meaning a higher beam current is required. Also there

are additional background contributions to the cross section of the photoproduction reaction which come from non-resonant processes, meaning more advanced models are required when interpreting measurements.

With further technological developments, stable polarised photon beams and targets[18] began to be used alongside recoil polarimeters. These introduced the possibility of measuring polarisation observables. Different polarisation observables are sensitive to partial waves, providing essential information necessary for the unambiguous decomposition of signals from different resonances.

A successful model of the nucleon and the strong interaction should be able to both predict the measured masses and widths of N^* and Δ^* resonances as well as the amplitude of their couplings with different decay channels. This has proved difficult as experiments have not yet provided precise enough measurements to unambiguously identify partial wave contributions. Current partial wave models are able to successfully fit experimental results but the free parameters in the fit are not well enough constrained and extrapolations beyond the range of measurements can vary wildly.

In order to refine our theoretical models of the nucleon, additional measurements need to be made to better constrain the properties and amplitudes of resonances. The current experimental program is focused on measuring photoproduction polarisation observables in order to constrain the partial wave contributions from different N^* and Δ^* resonances[19, 20].

Table 1.2 shows the current state of the nucleon resonances detected in experiments, as provided by the Particle Data Group (PDG)[21].

The discrepancy between the baryon resonance predictions of the quark model[16] and experimental measurements is displayed in figure 1.2.

The analysis carried out for this thesis focused on the π^0 and $2\pi^0$ final states and the formalism developed in the next chapter relates closely to the simpler case of the single π^0 final state.

The remainder of the thesis is laid out as follows: Chapter 2 describes how nucleon

resonances are modelled through partial waves. Different theoretical approaches to predicting measurable properties of the proton are discussed in chapter 3 along with previous measurements of the analysis conducted for this work. The experimental approach taken for these measurements is given in chapter 4 with the methods used to calibrate the experiment in chapter 5. The procedure used to extract the results is outlined in chapter 6. Final results are presented in chapter 7 before a few concluding remarks, regarding the importance of the work to a wider investigation into the fundamental questions of hadron physics, are discussed in chapter 8.

N^*	J^P	L_{2I2J} (pπ)	Status	Δ^*	J^P	L_{2I2J} (pπ)	Status
N(938)	$1/2^+$	P_{11}	****				
N(1440)	$1/2^+$	P_{11}	****	$\Delta(1232)$	$3/2^+$	P_{33}	****
N(1520)	$3/2^-$	D_{13}	****	$\Delta(1600)$	$3/2^+$	P_{33}	***
N(1535)	$1/2^-$	S_{11}	****	$\Delta(1620)$	$1/2^-$	S_{31}	****
N(1650)	$1/2^-$	S_{11}	****	$\Delta(1700)$	$3/2^-$	D_{33}	****
N(1675)	$5/2^-$	D_{15}	****	$\Delta(1750)$	$1/2^+$	P_{31}	*
N(1680)	$5/2^+$	F_{15}	****	$\Delta(1900)$	$1/2^-$	S_{31}	**
N(1700)	$3/2^-$	D_{13}	***	$\Delta(1905)$	$5/2^+$	F_{35}	****
N(1710)	$1/2^+$	P_{11}	****	$\Delta(1910)$	$1/2^+$	P_{31}	****
N(1720)	$3/2^+$	P_{13}	****	$\Delta(1920)$	$3/2^+$	P_{33}	***
N(1860)	$5/2^+$	F_{15}	**	$\Delta(1930)$	$5/2^-$	D_{35}	***
N(1875)	$3/2^-$	D_{13}	***	$\Delta(1940)$	$3/2^-$	D_{33}	**
N(1880)	$1/2^+$	P_{11}	**	$\Delta(1950)$	$7/2^+$	F_{37}	****
N(1895)	$1/2^-$	S_{11}	**	$\Delta(2000)$	$5/2^+$	F_{35}	**
N(1900)	$3/2^+$	P_{13}	***	$\Delta(2150)$	$1/2^-$	S_{31}	*
N(1990)	$7/2^+$	F_{17}	**	$\Delta(2200)$	$7/2^-$	G_{37}	*
N(2000)	$5/2^+$	F_{15}	**	$\Delta(2300)$	$9/2^+$	H_{39}	**
N(2040)	$3/2^+$	P_{13}	*	$\Delta(2350)$	$5/2^-$	D_{35}	*
N(2060)	$5/2^-$	D_{15}	**	$\Delta(2390)$	$7/2^+$	F_{37}	*
N(2100)	$1/2^+$	P_{11}	*	$\Delta(2400)$	$9/2^-$	G_{39}	**
N(2120)	$3/2^-$	D_{13}	**	$\Delta(2420)$	$11/2^+$	$H_{3,11}$	****
N(2190)	$7/2^-$	G_{17}	****	$\Delta(2750)$	$13/2^-$	$I_{3,13}$	**
N(2220)	$9/2^+$	H_{19}	****	$\Delta(2950)$	$15/2^+$	$K_{3,15}$	**
N(2250)	$9/2^-$	G_{19}	****				
N(2300)	$1/2^+$	P_{11}	**				
N(2570)	$5/2^-$	D_{15}	**				
N(2600)	$11/2^-$	$I_{1,11}$	***				
N(2700)	$13/2^+$	$K_{1,13}$	**				

Table 1.2: The Particle Data Group resonance table[21]; showing the N^* and Δ^* states. 4-star resonances are well founded and characterised while 1-star resonances have limited experimental evidence. The number beside each resonance relates to its invariant mass in MeV. J^P and L_{2I2J} are alternative descriptions of the resonance properties, where J is the total angular momentum of the resonance, P is the parity, L is the orbital angular momentum expressed in spectroscopic notation and I is the isospin.

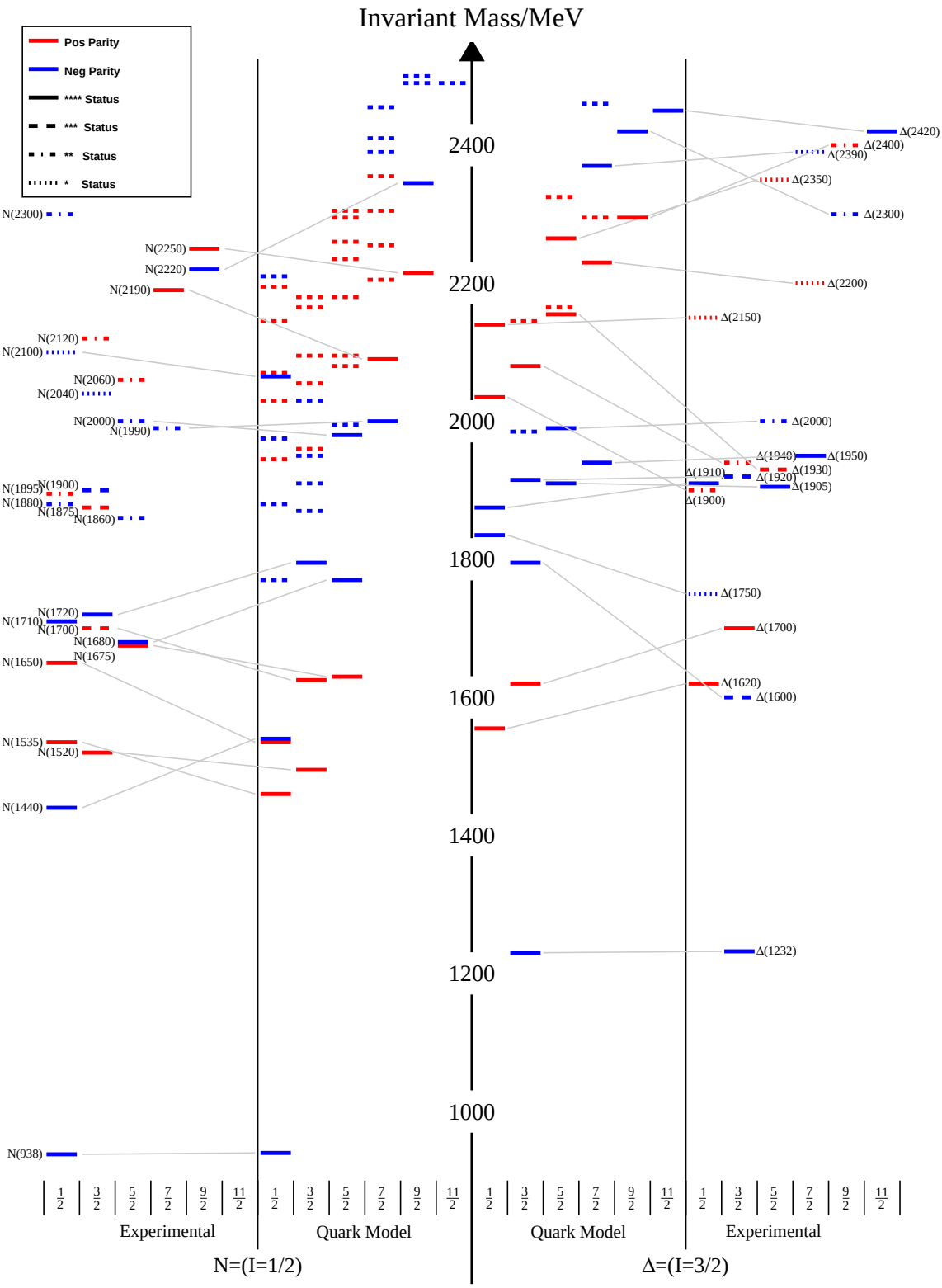

Figure 1.2: Spectrum of measured[21] and predicted[16] baryon resonances. Grey lines are tentative assignments of predicted states to those measured.

Chapter 2

Photoproduction Experiments

Photoproduction experiments use energetic real photons to probe the properties of a target particle. The aim is to expand our understanding of the properties of the nucleon excitation spectrum by determining the electric and magnetic coupling of the contributing resonances. As an electromagnetic probe, the photon is able to excite states that are forbidden, or only weakly couple with a hadron scattering interaction, and so can go beyond measurements achieved in the earlier pion beam experiments, upon which most of the current resonance understanding is based.

This chapter explores the physics of nucleons and how photoproduction experiments can be used to explore their excitation spectrum. The focus is towards the two reaction channels measured in this thesis:

$$\begin{aligned} \gamma \mathrm{p} &\rightarrow \mathrm{p}\pi^0 \\ \gamma \mathrm{p} &\rightarrow \mathrm{p}\pi^0\pi^0, \end{aligned} \tag{2.1}$$

and the observables which can be measured by using a linearly polarised photon beam.

Pions

The π meson is the lightest hadron, as such it has the lowest photoproduction threshold energy of all hadronic particles. A pion consists of a light quark anti-quark pair, coming in three charge states, π^+, π^- and π^0 respectively with quark contents $u\bar{d}$, $d\bar{u}$ and $\frac{u\bar{u}-d\bar{d}}{\sqrt{2}}$.

The π^0 has a lifetime of $8.32\pm0.02\times10^{-17}$s[22, 23] which is much shorter than the $\pi^\pm$, which decay through the weak process, with a lifetime of $2.6033\pm0.0005\times10^{-8}$s[21]. Two branches contribute to the π^0 decay:

$$\begin{aligned} \pi^0 &\rightarrow \gamma\gamma(98.8\%), \\ \pi^0 &\rightarrow e^+e^-\gamma(1.2\%), \end{aligned} \tag{2.2}$$

where the number in brackets is the branching ratio[24]. The analysis in this thesis focuses only on detecting the dominant branch, which decays to the $\gamma\gamma$ final state.

2.1 Probing Hadrons

Fundamentally a photoproduction reaction can be described as a quantum scattering experiment. The setup of such an experiment (Figure 2.1) allows an interaction between the beam (plane wave) and target to be mapped out by measuring the form of the scattered waves. Knowledge of the initial properties of the beam and target and measurement of the distribution of the final set of particles can be used to infer the nature of a reaction.

The interaction between a high energy photon and a proton is complicated, with the outgoing wave formed from a superposition of waves contributing from many reaction processes. The scattered wave can be decomposed into *partial waves* relating to each of these individual processes.

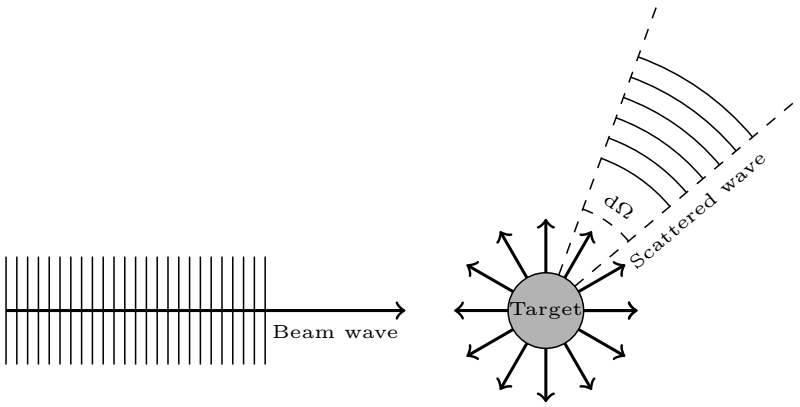

Figure 2.1: Basic setup of a scattering experiment.

2.1.1 Photoproduction Channels

In general there are many different reaction channels that contribute to the final state of a photoproduction experiment. The probability of any interaction occurring between the beam and target is characterised by the total cross section (σ_t), measured in units called barns (b)[1]. The total cross section comprises all possible reaction channels including both elastic scattering, σ_{el} and inelastic σ_{in}, photoproduction processes. With increasing beam energy, additional reaction channels open as their threshold energies are passed, for example $2\pi^0$.

Figure 2.2 shows measurements of the total hadronic photoproduction cross section off the proton[25, 26, 27]. The total cross section is shown divided into final states with the π^0 and $2\pi^0$ channels highlighted.

The structure of the cross sections as a function of energy provides evidence of nucleon resonances, however more resonances are known to contribute to the reactions than can be identified by simply counting the peaks. Hadronic resonances have a short mean lifetime ($\tau \sim 10^{-24}$ s) which is linked by Heisenberg's uncertainty principle to its mass decay width by,

$$\tau = \frac{\hbar}{\Gamma}. \tag{2.3}$$

[1]A barn is a unit of area equivalent to 10^{-28} m^2

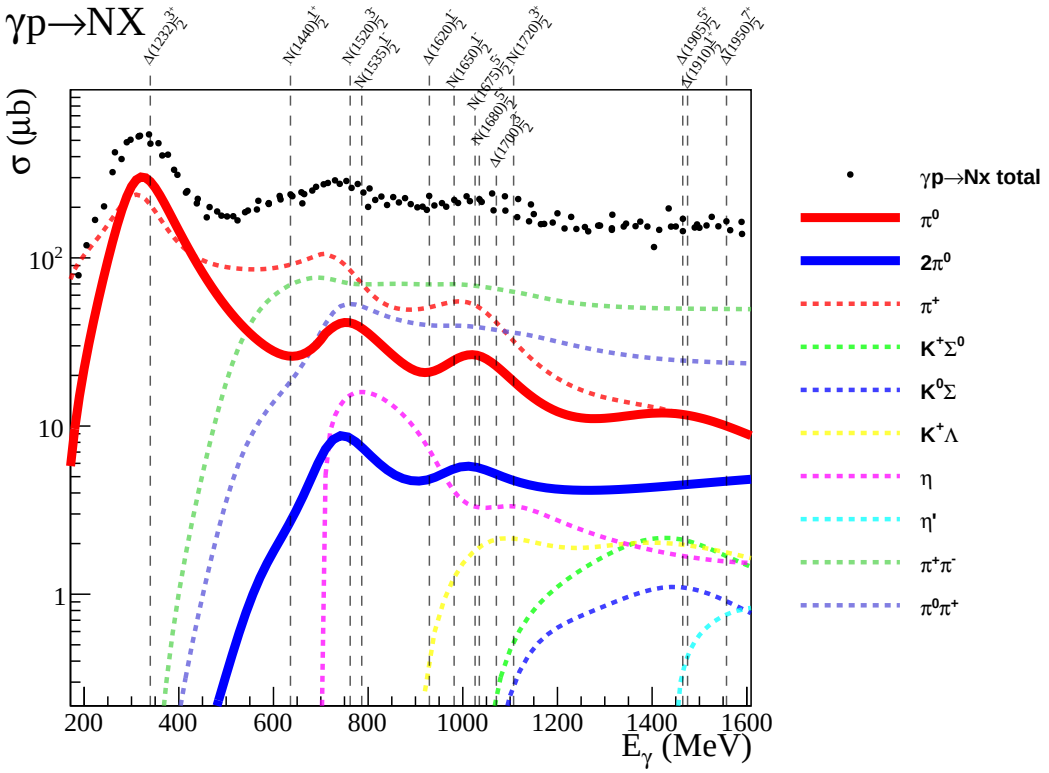

Figure 2.2: Cross section of hadronic photoproduction processes across a range of E_γ. PDG four star N* and Δ resonances are shown as dashed vertical lines[21] at the position at which E_γ provides the centre of mass energy W relating to the resonance invariant mass.

The width describes the energy dependence of a relativistic Breit–Wigner[28], relating the centre of mass energy $(W)^2$ of the reaction to the probability of exciting a resonance with a particular invariant mass. The invariant mass and width of hadron resonances are the same order of magnitude, and so often are described as *broad and overlapping* with many other resonances.

Individual decay channels couple strongly to different resonances, investigating the channels separately proves a powerful mechanism for determining resonance properties.

[2]The relationship between E_γ and W for photoproduction off the proton is simply $W=\sqrt{(m_\mathrm{p}+E_\gamma)^2-E_\gamma^2}$. Where m_p is the mass of the proton and the speed of light (c) which would normally appear in the relationship is set to 1 so is absent.

2.1.2 Decay Mechanisms

The final state of a photoproduction experiment is a superposition of a variety of reaction mechanisms. Feynman diagrams of the first order π^0 production pathways are displayed in figure 2.3. Non-resonant background processes are Born channels[29] where the γ directly couples to the nucleon and ρ/ω vector meson exchange.

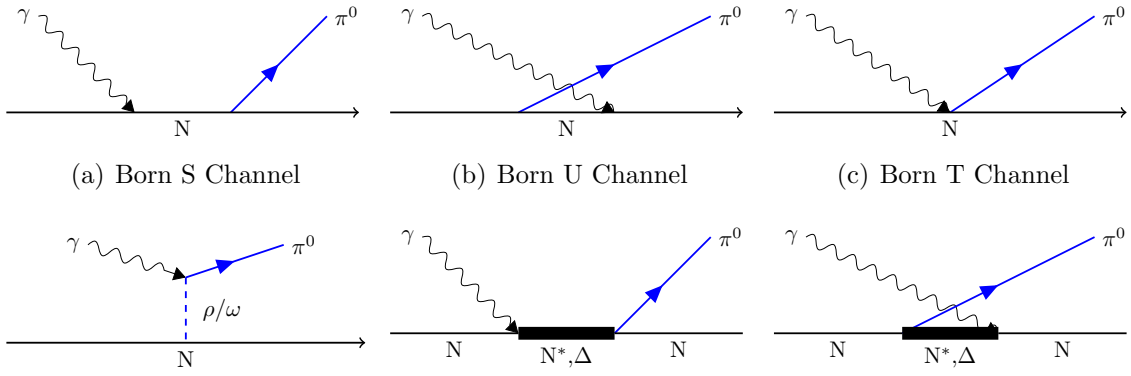

(a) Born S Channel (b) Born U Channel (c) Born T Channel

(d) Vector Meson Exchange (e) Resonant Process S (f) Resonant Process U

Figure 2.3: Processes resulting in the photoproduction of a single π^0. Processes a-d and f are considered as background when searching for N* or Δ resonances.

In $2\pi^0$ photoproduction there are a larger number of potential reaction pathways. Key resonance decays of are shown in figure 2.4 where the mechanism is a two step process either with an intermediate σ meson[30] or Δ baryon. There are more background mechanisms contributing to the $2\pi^0$ final state, including background Born terms from both direct N and Δ coupling, a comprehensive selection of Feynman diagrams can be found in reference [31].

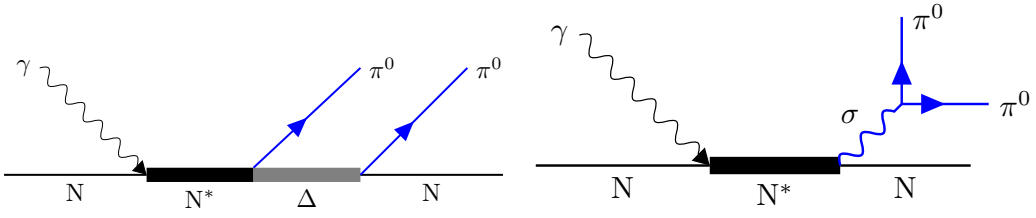

(a) Δ intermediate state (b) σ intermediate state

Figure 2.4: Resonance processes resulting in the photoproduction of $2\pi^0$s.

Many of the mechanisms allowed in $\pi^+\pi^-$ photoproduction are forbidden by the inherent symmetry of the $2\pi^0$ wave function. This makes the $2\pi^0$ decay channel a

powerful tool as reactions are cleaner with a higher sensitivity to resonances, as the contribution from vector meson production is suppressed.

Observable quantities include contributions summed from all of the reaction mechanisms. Background mechanism couplings have a predictable, smooth energy dependence[32], so any additional structure needs to be accounted for by the inclusion of resonant states. Effects of superimposing a resonance on the model are referred to as the *dressed* resonance contribution, accounting for the contribution of the resonance and interference with the background mechanisms.

An explanation of the physics of summing together contributions from each reaction mechanism is provided in the next section.

2.2 Resonance Contributions

Nucleon resonance contributions to scattering reactions can be described by harmonic multipoles, in a similar fashion to excited atomic electrons or nuclei. Unlike electrons and nuclei, the nucleon resonances are broad and overlapping, making it difficult to identify how individual resonances couple to different decays. In order to quantify the coupling of a reaction channel to resonance and background mechanisms, measurements of differential cross sections with a selection of polarisation states are needed. With accurate enough measurements, a collection of simultaneous equations can be used to find a unique solution to the resonance couplings[33].

The total cross section of a decay channel is the integral over all potential final state kinematics. The beam direction breaks the spherical symmetry of the target, providing an axis from which resonant states may align. The differential cross section $\left(\frac{\mathrm{d}\sigma}{\mathrm{d}\Omega}(\theta_{cm})\right)$ is given here as the probability of detecting a particle in the centre of mass solid angle range $\mathrm{d}\Omega$, related to the angle θ_{cm} with respect to the beam axis. There is no azimuthal dependence in the differential cross section when neither the beam nor target are polarised, and so nothing breaks the symmetry around the beam axis. Examples of the differential cross section for photoproduction processes $\mathrm{p}\gamma \rightarrow \mathrm{p}\pi^0$ and $\mathrm{p}\gamma \rightarrow \mathrm{n}\pi^+$ at different E_γ are shown in figure 2.5, where the values have been

taken from the MAID fit[34].

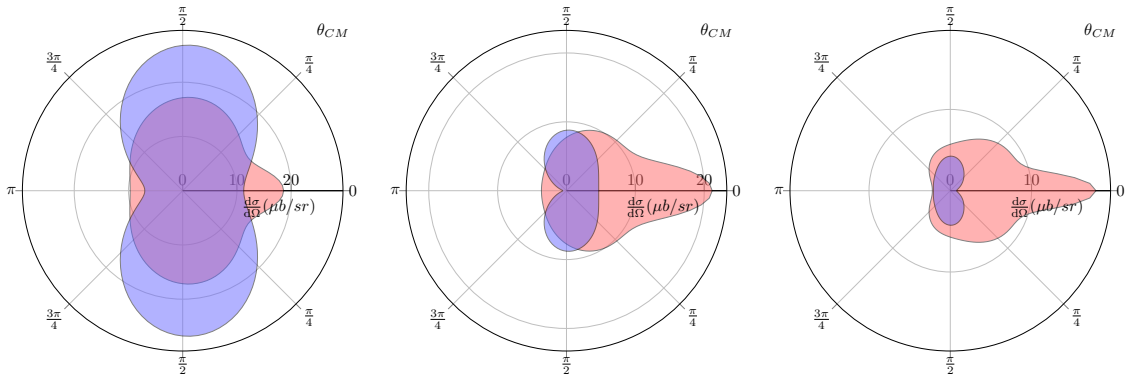

(a) $E_\gamma = 350$ MeV (b) $E_\gamma = 450$ MeV (c) $E_\gamma = 780$ MeV

Figure 2.5: Photoproduction differential cross section of π^0 (blue) and π^+ (red) off the proton produced with different E_γ. The plots show an extended θ_{cm} range, equivalent to taking a slice through the beam axis, emphasising the symmetry of the cross section. Values have been taken from the MAID fit[34].

The differential cross sections of π^+ and π^0 photoproduction are a superposition of multiple reaction mechanisms. At 350 MeV the main contributors to the differential cross section come from the $\Delta(1232)$ partial wave and the background Born channels. Multiple resonance partial waves interfere at higher energies and generate a more complex differential cross section.

Contributions from resonance and background mechanisms are described by partial waves. Partial waves are understood by further devolving the waves into a series of orthogonal harmonic multipoles.

2.2.1 Photoproduction Amplitudes

A differential cross section can be described by a series of orthogonal multipoles, called Legendre polynomials. The first five Legendre polynomials are shown as a function of $\cos\theta$ in figure 2.6.

A target nucleon couples to both electric and magnetic components of the incident photon, and the spin of the nucleon can be either parallel or anti-parallel to the relative angular momentum ℓ. This means four constants are needed to describe the coupling of a reaction with angular momentum ℓ ($E_{\ell+}$, $E_{\ell-}$, $M_{\ell+}$ and $M_{\ell-}$), where

$$
\begin{aligned}
P_0 &= 1 \\
P_1 &= \cos\theta \\
P_2 &= \frac{1}{2}(3\cos^2\theta - 1) \\
P_3 &= \frac{1}{2}(5\cos^3\theta - 3\cos\theta) \\
P_4 &= \frac{1}{8}(35\cos^4\theta - 30\cos^2\theta + 3)
\end{aligned}
\tag{2.4}
$$

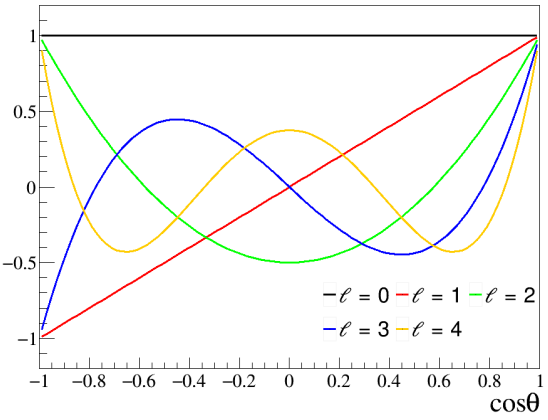

Figure 2.6: Five lowest order Legendre polynomials in terms of $\cos\theta$.

the $\pm$ subscript implies the nucleon spin is orientated parallel or anti-parallel to the angular momentum.

The formalism used here to describe the connection between the coupling constants and measurable quantities originates in references [35, 33]. First the multipole couplings are expressed in relation to reaction amplitudes of different helicity spin configurations. In π^0 photoproduction there are four possible spin configurations shown in figure 2.7.

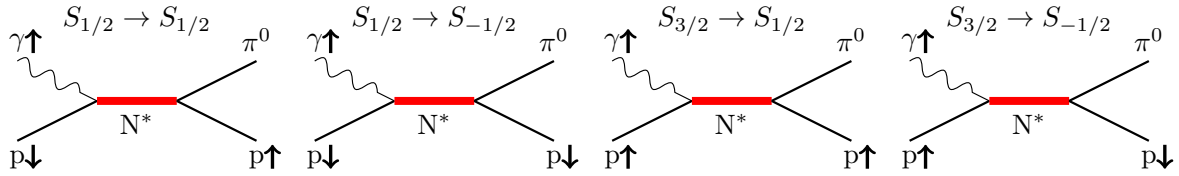

(a) N - No spin flip (b) S_A - Anti-parallel spin flip (c) S_P - Parallel spin flip (d) D - Double spin flip

Figure 2.7: Spin flip configurations relating to helicity amplitudes N, S_A, S_P and D. Spin is denoted by the arrow beside the γ, initial and final state protons. Spins are either parallel or anti-parallel to each other. The photon is a boson with spin given by $s_\gamma = \pm 1$ while the proton is a fermion with spin $s_\mathrm{p} = \pm 1/2$.

The four helicity amplitudes can be expressed as sums of the electric and magnetic

coupling constants ($E_{\ell\pm}, M_{\ell\pm}$), and Legendre polynomials[36, 35]

$$
\begin{aligned}
N &= \frac{1}{\sqrt{2}}\cos\left(\frac{\theta}{2}\right)\sum_{\ell=0}^{\infty}\left[(\ell+2)\,E_{\ell+} + \ell M_{\ell+} + \ell E_{(\ell+1)-} - (\ell+2)M_{(\ell+1)-}\right]\left(P'_{\ell} - P'_{\ell+1}\right)\\
S_A &= \frac{1}{\sqrt{2}}\sin\left(\frac{\theta}{2}\right)\sum_{\ell=0}^{\infty}\left[(\ell+2)\,E_{\ell+} + \ell M_{\ell+} - \ell E_{(\ell+1)-} + (\ell+2)M_{(\ell+1)-}\right]\left(P'_{\ell} + P'_{\ell+1}\right)\\
S_P &= \frac{1}{\sqrt{2}}\cos\left(\frac{\theta}{2}\right)\sin\theta\sum_{\ell=1}^{\infty}\left[E_{\ell+} - M_{\ell+} - E_{(\ell+1)-} - M_{(\ell+1)-}\right]\left(P''_{\ell} - P''_{\ell+1}\right)\\
D &= \frac{1}{\sqrt{2}}\sin\left(\frac{\theta}{2}\right)\sin\theta\sum_{\ell=1}^{\infty}\left[E_{\ell+} - M_{\ell+} + E_{(\ell+1)-} + M_{(\ell+1)-}\right]\left(P''_{\ell} + P''_{\ell+1}\right),
\end{aligned}
\tag{2.5}
$$

where P'_{ℓ} and P''_{ℓ} are the first and second order derivatives of the Legendre polynomials. The total cross section can then be given as,

$$
\sigma = N^2 + S_A^2 + S_P^2 + D^2. \tag{2.6}
$$

The four helicity amplitudes can be converted to four complex transversity amplitudes,

$$
\begin{aligned}
b_1 &= \frac{1}{2}\left[(S_P + S_A) + i(N - D)\right]\\
b_2 &= \frac{1}{2}\left[(S_P + S_A) - i(N - D)\right]\\
b_3 &= \frac{1}{2}\left[(S_P - S_A) - i(N + D)\right]\\
b_4 &= \frac{1}{2}\left[(S_P - S_A) + i(N + D)\right]
\end{aligned}
\tag{2.7}
$$

The transversity amplitude formalism is used as it is intuitively linked to transverse polarisation states that can be accessed in experiments, these are described in section 2.3. The four complex amplitudes can be expressed as eight real numbers, four magnitudes and four phases. The transversity amplitudes can be combined in

ways that are accessible through experiment, describing cross sections and polarisation observable profile functions. To determine the magnitude and phase of the transversity amplitudes with eight unknown real numbers a series of at least seven simultaneous equations are needed.

The cross sections and polarisation profile functions are expressed in terms of transversity amplitudes,

$$\begin{aligned}
\frac{\mathrm{d}\sigma}{\mathrm{d}\Omega} &= |b_1|^2 + |b_2|^2 + |b_3|^2 + |b_4|^2 \\
\check{P} = P\frac{\mathrm{d}\sigma}{\mathrm{d}\Omega} &= |b_1|^2 - |b_2|^2 + |b_3|^2 - |b_4|^2 \\
\check{\Sigma} = \Sigma\frac{\mathrm{d}\sigma}{\mathrm{d}\Omega} &= |b_1|^2 + |b_2|^2 - |b_3|^2 - |b_4|^2 \\
\check{T} = T\frac{\mathrm{d}\sigma}{\mathrm{d}\Omega} &= |b_1|^2 - |b_2|^2 - |b_3|^2 + |b_4|^2 \\
\check{G} = G\frac{\mathrm{d}\sigma}{\mathrm{d}\Omega} &= 2\,\mathrm{Im}(b_1 b_3^* + b_2 b_4^*) \\
\check{H} = H\frac{\mathrm{d}\sigma}{\mathrm{d}\Omega} &= -2\,\mathrm{Re}(b_1 b_3^* - b_2 b_4^*) \\
\check{E} = E\frac{\mathrm{d}\sigma}{\mathrm{d}\Omega} &= -2\,\mathrm{Re}(b_1 b_3^* + b_2 b_4^*) \\
\check{F} = F\frac{\mathrm{d}\sigma}{\mathrm{d}\Omega} &= 2\,\mathrm{Im}(b_1 b_3^* - b_2 b_4^*)
\end{aligned} \tag{2.8}$$

2.2.2 Resonance Waves

Every resonance contributes to an electric and magnetic multipole coefficient $E_{L,p}$ and $M_{L,p}$, where p is expressed as $\pm$ defined from $2(J-L)$. The combination of quantum numbers I, J, L defines a partial wave form, determined by the ratio of the electric to magnetic coupling. Resonances with different isospins, I, can contribute to the wave multipoles but with different couplings. In addition to resonances with identical J, L, background mechanisms can also contribute to a particular multipole.

The strongest contributing resonances to the π^0 photoprodution channel in the energy range of this analysis are the $\Delta(1232)$ $3/2^+$ (P_{33}) and $N^*(1520)$ $3/2^-$ (D_{13}).

From equations 2.5 to 2.8, the properties of the these partial waves can be constructed using the measured E_{1+} and M_{1+} for the P_{33} and E_{2-} and M_{2-} for the D_{13}. The form of the partial waves of the individual coefficients to $\frac{d\sigma}{d\Omega}$ and $\check{\Sigma}$ as a function of $\cos\theta$ taken from equation 2.5 are

$$\begin{aligned}
\left(\frac{d\sigma}{d\Omega}\right)_{E_{1+}} &= 9k_{E_{1+}}\left(1+\cos^2\theta\right) \\
\left(\frac{d\sigma}{d\Omega}\right)_{M_{1+}} &= k_{M_{1+}}\left(5-3\cos^2\theta\right) \\
\left(\frac{d\sigma}{d\Omega}\right)_{E_{2-}} &= k_{E_{2-}}\left(5-3\cos^2\theta\right) \\
\left(\frac{d\sigma}{d\Omega}\right)_{M_{2-}} &= 9k_{M_{2-}}\left(1+\cos^2\theta\right),
\end{aligned} \tag{2.9}$$

$$\begin{aligned}
\check{\Sigma}_{E_{1+}} &= -9k_{E_{1+}}\sin^2\theta \\
\check{\Sigma}_{M_{1+}} &= 3k_{M_{1+}}\sin^2\theta \\
\check{\Sigma}_{E_{2-}} &= -3k_{E_{2-}}\sin^2\theta \\
\check{\Sigma}_{M_{2-}} &= 9k_{M_{2-}}\sin^2\theta,
\end{aligned} \tag{2.10}$$

where k are scaling coefficients determined by each partial wave contribution. Due to the changing contribution of each resonance as a function of energy the amplitudes outlined in equations 2.5 and 2.7 are also functions of reaction energy. What remain constant are the $E_{\ell\pm}^{J^P}$ and $M_{\ell\pm}^{J^P}$ constants relating to each particular J^P resonance.

Figures 2.8 and 2.9 demonstrate the multipole contributions respective to the P_{33} and D_{13} partial waves as differential cross sections and the polarisation observable Σ. The measured ratio, $R_{EM}^{3/2+} = E_{1+}^{3/2+}/M_{1+}^{3/2+}$ (for the P_{33} resonance) is very small at -0.024 ± 0.0004[37], while the ratio for the D_{13} resonance is much larger $R_{EM}^{3/2-} = 1.37 \pm 0.2$[38]. It should be noted that this ratio does not effect the dimensionless quantity Σ.

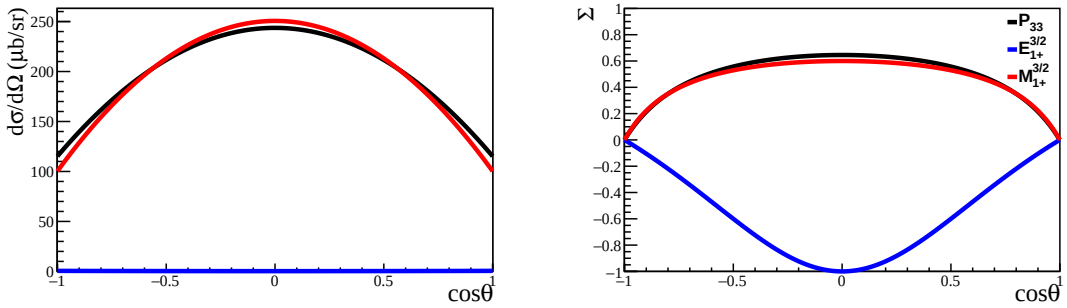

Figure 2.8: P_{33} partial wave expressed as the sum of $E_{1+}^{3/2+}$ and $M_{1+}^{3/2+}$ using experimentally measured ratio $R_{EM}^{3/2+} = -0.024 \pm 0.0004$[37]. Left - Differential cross section. Right - Σ beam asymmetry.

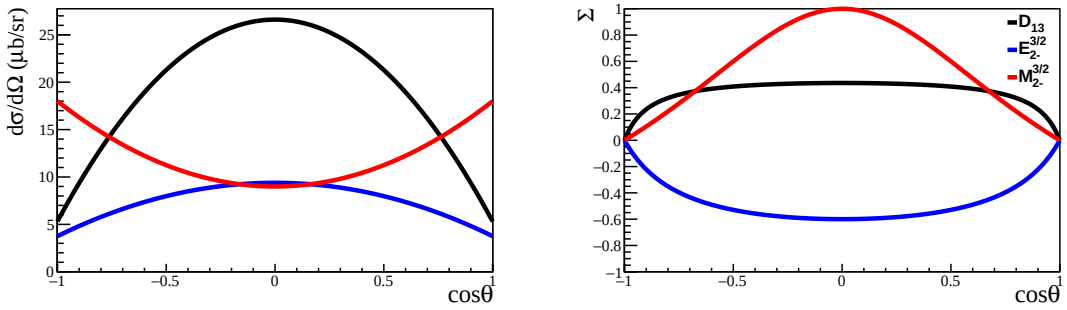

Figure 2.9: D_{13} partial wave expressed as the sum of $E_{2-}^{3/2-}$ and $M_{2-}^{3/2-}$ using experimentally measured ratio $R_{EM}^{3/2-} = -1.37 \pm 0.2$[38]. Left - Differential cross section. Right - Σ beam asymmetry.

Figure 2.10 shows the sum of the P_{33} and D_{13} partial waves at photon energy E_γ = 780 MeV, around the peak of the D_{13} mass. The resulting wave is clearly not a linear sum of the contributing partial waves. The form of the wave is now attributed to both the sum of the partial waves and interference terms.

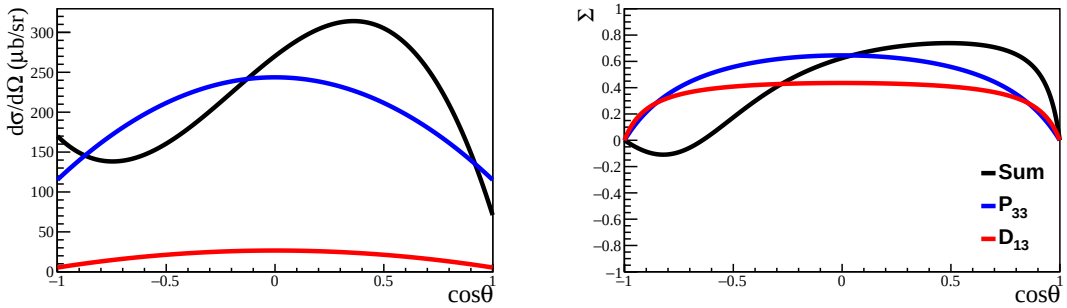

Figure 2.10: Wave resulting from the sum of the P_{33} and D_{13} resonances with relative contributions at E_γ=780 MeV taken from the MAID fit[34]. Left - Differential cross section. Right - Σ beam asymmetry.

Resonance Forms

The contributions of the resonance partial waves to the differential cross section can be calculated using E and M coefficients from MAID[34], or similar, fits. An example of these resonance contributions, taken at $E_\gamma = 780$ MeV, is shown in figure 2.11.

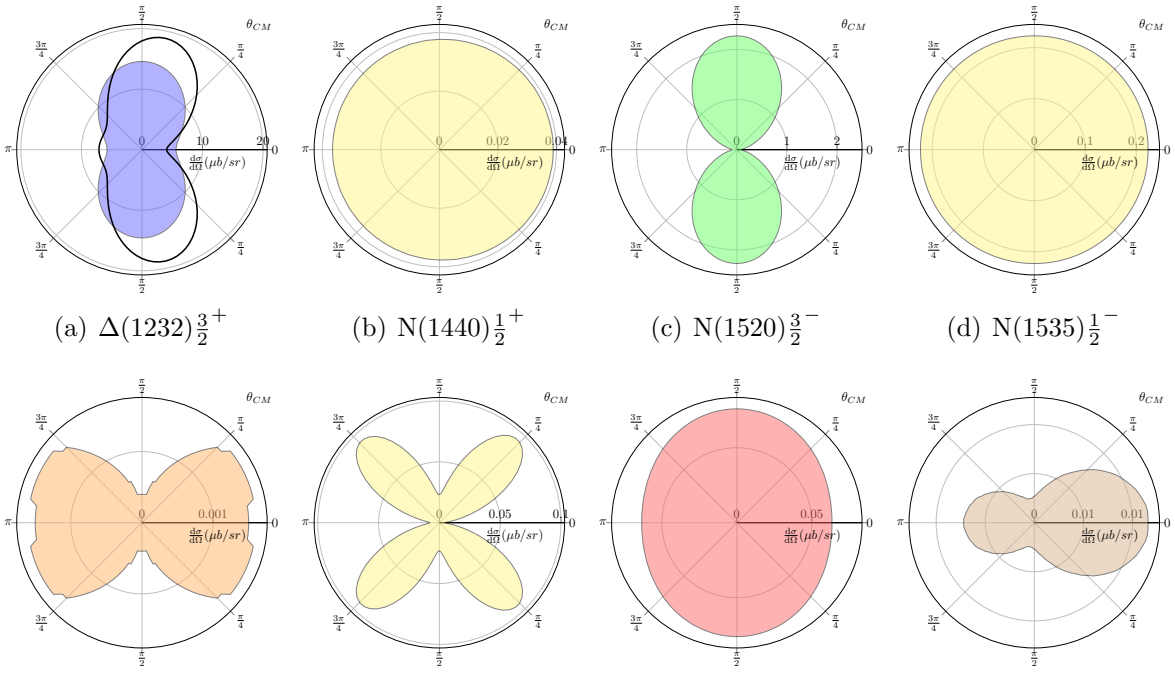

(a) $\Delta(1232)\frac{3}{2}^+$ (b) $N(1440)\frac{1}{2}^+$ (c) $N(1520)\frac{3}{2}^-$ (d) $N(1535)\frac{1}{2}^-$

(e) $N(1675)\frac{5}{2}^-$ (f) $N(1680)\frac{5}{2}^+$ (g) $\Delta(1700)\frac{3}{2}^-$ (h) $N(1720)\frac{3}{2}^+$

Figure 2.11: Contributions to the π^0 total differential cross section at E_γ=780 MeV (W=1532 MeV) from the 4-star resonances up to 1800 MeV mass (excluding resonances described by identical J^P). The black line in plot (a) represents the total resonant contribution to the differential cross section. The relative scales and distributions of the partial waves have been taken from the MAID fit[34].

Born and Meson Exchange Forms

The differential cross section form of the background partial waves is shown at different energies in figure 2.12. The direct π-N coupling is well measured[39] from pion scattering experiments. Electric and magnetic multipoles contribute to the background terms with gradually and smoothly varying magnitudes across the energy range.

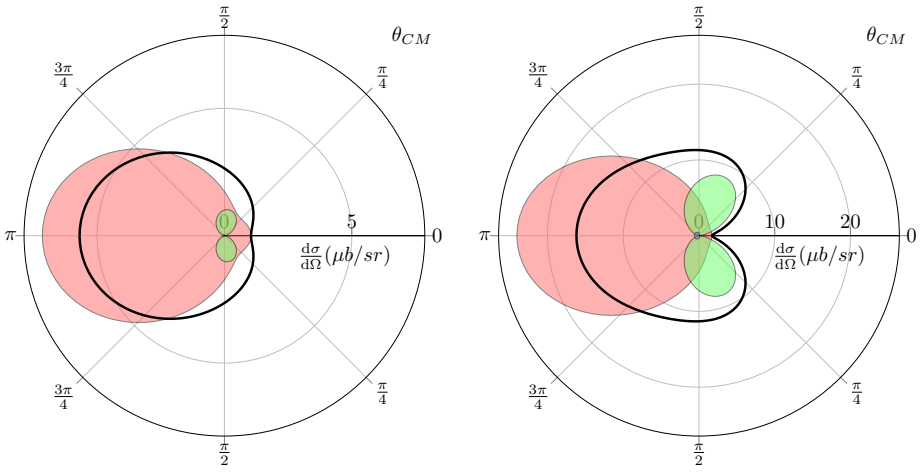

(a) $E_\gamma = 350$ MeV (b) $E_\gamma = 780$ MeV

Figure 2.12: Differential cross section contributions from Born processes (red), ω meson exchange (green), and from ρ meson exchange (blue - very small). The sum of the contributions is the thick black outline.

Total Wave

Predictions of the multipole coefficients from a fit to the world data collection of differential cross sections and polarisation observables can be used to construct the combined total wave, including both resonance and background terms. Examples for two energies are shown in figure 2.13 where it is clear that there is strong destructive interference between the resonance and Born terms.

The next section describes which measurements are required to unambiguously determine the multipole contributions for single and double π^0 photoproduction.

2.3 Experimental Measurements

Several separate measurements need to be made in order to fully determine the partial wave contributions to a decay. A complete set of experimental measurements; constraining the magnitude and phase of all of the associated decay amplitudes are described for single and double π^0 photoproduction in sections 2.3.1 and 2.3.2.

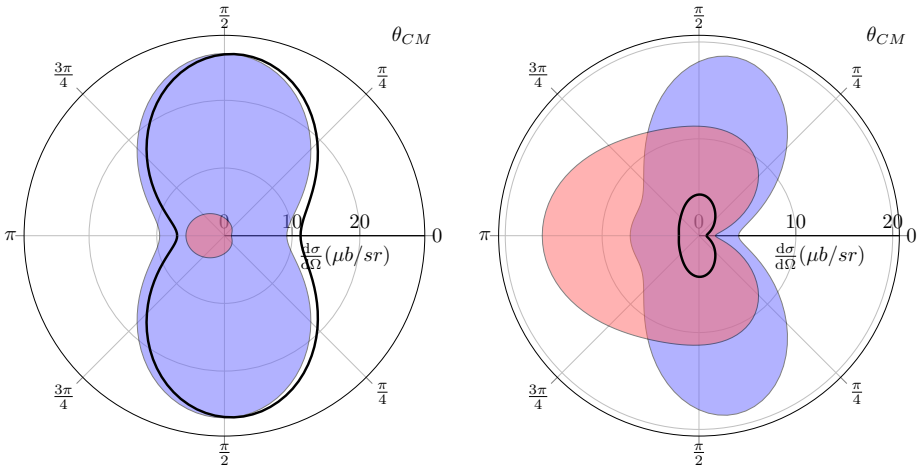

(a) $E_\gamma = 350$ MeV (b) $E_\gamma = 780$ MeV

Figure 2.13: Differential cross section contributions from background processes (red) and resonance processes (blue). The sum of the contributions is the thick black outline.

2.3.1 $\gamma p \rightarrow \pi^0 p$ measurements

There are sixteen observables that can be measured in π^0 photoproduction by using different polarisation configurations that are laid out in table 2.1. The transversity amplitudes defining the decay wave (equation 2.7) are described by eight real numbers. The observables are not independent; only a subset need to be measured to determine the amplitudes, and thereby predict the value of any observable.

Photon Beam		Target			Recoil			Target + Recoil			
					x'	y'	z'	x'	x'	z'	z'
		x	y	z				x	z	x	z
Unpolarised	σ_0		T			P		$T_{x'}$	$L_{x'}$	$T_{z'}$	$L_{z'}$
Linear	Σ	H	P	G	$O_{x'}$	T	$O_{z'}$				
Circular		F		E	$C_{x'}$		$C_{z'}$				

Table 2.1: Polarisation observables measurable in single meson photoproduction. The columns and rows define different experimental polarisations of the beam and target. σ_0 is the unpolarised differential cross section and the other observables describe the effect on σ_0 in different polarisation experiments. Note P and T may be accessed through two different experiments.

The relationship between all of the observables in table 2.1 and experimental polar-

isations is given by

$$\begin{aligned}\frac{\mathrm{d}\sigma}{\mathrm{d}\Omega} = \frac{1}{2}\sigma_0 \{ 1 &- \mathrm{P^T}\Sigma\cos 2\phi + \mathrm{P_x}\left(\mathrm{P^\odot F} + \mathrm{P^T H}\sin 2\phi\right) \\ &+ \mathrm{P_y}\left(\mathrm{T} - \mathrm{P^T P}\cos 2\phi\right) + \mathrm{P_z}\left(\mathrm{P^\odot E} + \mathrm{P^T G}\sin 2\phi\right) \\ &\sigma'_{\mathrm{x}}\left[\mathrm{P^\odot C'_x} + \mathrm{P^T O'_x}\sin 2\phi + \mathrm{P_x}\left(\mathrm{T'_x} - \mathrm{P^T L'_z}\cos 2\phi\right)\right. \\ &\left.+\mathrm{P_y}\left(\mathrm{P^T C'_z}\sin 2\phi - \mathrm{P^\odot O'_z}\right) + \mathrm{P_z}\left(\mathrm{L'_x} + \mathrm{P^T T'_z}\cos 2\phi\right)\right] \\ &\sigma'_{\mathrm{y}}\left[\mathrm{P} + \mathrm{P^T T}\cos 2\phi + \mathrm{P_x}\left(\mathrm{P^\odot G} - \mathrm{P^T E}\sin 2\phi\right)\right. \\ &\left.+\mathrm{P_y}\left(\Sigma - \mathrm{P^T}\cos 2\phi\right) + \mathrm{P_z}\left(\mathrm{P^T F}\sin 2\phi + \mathrm{P^\odot H}\right)\right] \\ &\sigma'_{\mathrm{z}}\left[\mathrm{P^\odot C'_z} + \mathrm{P^T O'_z}\sin 2\phi + \mathrm{P_z}\left(\mathrm{T'_z} + \mathrm{P^T L'_x}\cos 2\phi\right)\right. \\ &\left.+\mathrm{P_y}\left(-\mathrm{P^T C'_x}\sin 2\phi - \mathrm{P^T O'_z}\right) + \mathrm{P_z}\left(\mathrm{L'_z} + \mathrm{P^T T'_z}\cos 2\phi\right)\right] ,\end{aligned} \tag{2.11}$$

where the observables are coloured blue, the photon polarisation is coloured red with $\mathrm{P^T}$ and $\mathrm{P^\odot}$ respectively linear and circular degrees of polarisation and the proton polarisation is coloured green with $\mathrm{P_x}$ and σ'_{x} respectively the degree of polarisation of the target and the recoiling proton where the subscript describes the relative direction of the polarisation[40].

The term *complete measurement* is used in hadron spectroscopy to describe when a set of observables have been measured, from which the magnitude and phase of the amplitudes can be determined. The nature of experimental measurements means that there is an uncertainty in the amplitudes, so they can never be completely constrained.

The subset of measurements required for a complete measurement of π^0 production must include at least one observable from each of the polarisation categories described in table 2.1. For example, the eight transverse observables $\{\sigma_0, \Sigma, P, T, G, H, E, F\}$ can form the basis of a complete experiment, the relationship between these observables and the amplitudes has previously been described in equation 2.8. This set of variables consists of the differential cross section and three single polarisation observables which together can determine the magnitudes of the transversity

amplitudes, while the four double polarisation observables determine the amplitudes' complex phases.

The photon beam asymmetry observable, Σ has been measured for this thesis, and reflects the asymmetry of the pion production plane relative to the linear polarisation plane of the photon beam. A description of the kinematics involved is given in section 2.4.1.

2.3.2 $\gamma p \rightarrow 2\pi^0 p$ measurements

A full discussion of the derivation of all the polarisation observables involved in double π photoproduction is given in reference [41].

The complete experiment for $2\pi^0$ photoproduction requires 16 select measurements of 64 potential observables to determine 8 complex amplitudes. Measurements of triple polarisation observables are now required, where the beam and target are polarised and the recoiling proton polarisation is measured. It is useful to measure the observables using vectors associated more strongly with either the (N*,Δ) or meson resonance intermediate states.

The $2\pi^0$ polarisation observables Σ, I^s and I^c measured for this thesis are all accessed through polarising the photon beam linearly. For an experimental description of the variables see sections 2.4.2 and 2.4.3.

2.4 Observables With A Linearly Polarised Photon Beam

The focus of this thesis is polarisation observables accessible using a linearly polarised photon beam. This section describes the kinematics involved in measuring the observable Σ in π^0 photoproduction and the three observables; Σ, I^s and I^c, in $2\pi^0$ photoproduction.

2.4.1 Σ Observable - Single π^0

The description of the frame from which values of Σ for single π^0 photoproduction are extracted is shown in figure 2.14. In the centre of mass frame the proton and π^0 are restricted to having equal and opposite, *back-to-back* momenta. The π^0 is conventionally used to describe the θ and ϕ angles of measurements. θ is the polar angle of the π^0 from the beam axis in the reaction centre of mass frame and ϕ is the azimuthal angle between the linear polarisation plane and the reaction plane.

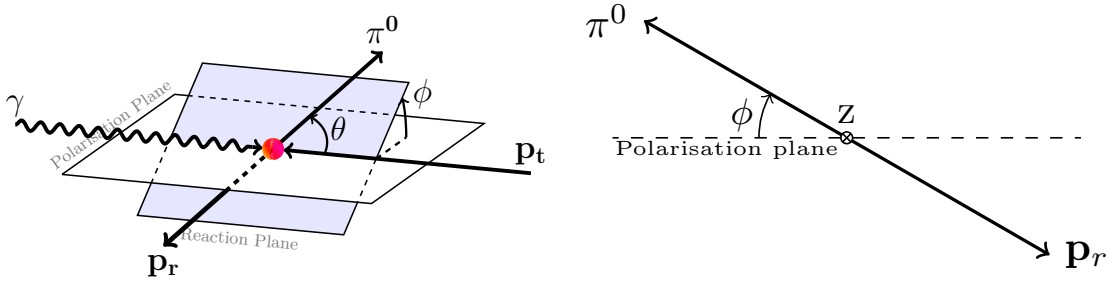

(a) π^0 reaction frame (b) π^0 projection

Figure 2.14: Left - Full kinematics of the π^0 photoproduction reaction in the centre of mass frame. Right - Projection along the beam axis of the two body system, showing the angle ϕ used to calculate Σ.

The polarisation observable Σ manifests itself as a $\cos(2\phi)$ dependence in measured differential cross section

$$\frac{d\sigma}{\mathrm{d}\Omega}(\phi) = \left(\frac{\mathrm{d}\sigma}{\mathrm{d}\Omega}\right)_0 (1 + P^T \Sigma \cos(2\phi)), \tag{2.12}$$

where Σ is the relative size of the variation in the cross section compared to its absolute magnitude and P^T is the degree of photon linear polarisation.

2.4.2 $\Sigma_{p/\pi}$ Observable - Double π^0

The $2\pi^0$ photoproduction reaction has three final state particles, this means the reaction can be described by 5 independent kinematic variables at fixed W, and so particles are no longer restricted to having back-to-back centre of mass angles. The

reaction can be simplified into quasi two-body systems by summing the 4-vectors of two particles. This reproduces a 4-vector with back-to-back momenta with the third particle. There are two distinct frames to be considered; providing two separate Σ observables.

The first system takes the vector of the recoiling proton, opposite to the sum of the two π^0 vectors, as shown in figure 2.15. An asymmetry of the polarised data sets is taken and the ϕ distribution of the recoil proton 4-vector (P_p) used to calculate the observable, given the name Σ_p.

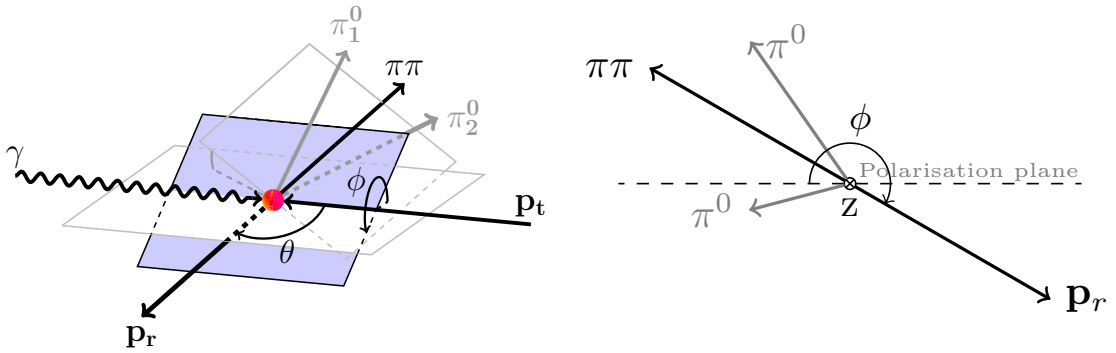

(a) Simplified $2\pi^0$ reaction frame

(b) $\pi\pi$ projection

Figure 2.15: Projection along the beam axis of the quasi two body system, showing the angle required to calculate Σ_p.

The second system is taken from the vector of one of the recoiling π^0s, opposite to the sum of the missing proton and the other detected pion, as shown in figure 2.16. Due to the indistinguishable nature of the two π^0s, they need to be treated identically. Both π^0 combinations are taken into account when making the measurement, with each 4-vector, $P_{\pi_1^0}$ and $P_{\pi_2^0}$, contributing half to the yield distributions, this is called Σ_π.

The two frames strongly relate to decay processes with either a meson or Δ intermediate state. The proton recoil frame is best used to describe a meson intermediate state, the proton emitted from the initial resonance decay is sensitive to the photo-produced resonance polarisation, otherwise described as having a strong analysing power. The π^0 recoil frame describes the Δ intermediate state, with the π^0 produced directly from the primary N* resonance containing the analysing power. Figure 2.17 shows a 2D representation of the two decay pathways, the Feynman diagrams re-

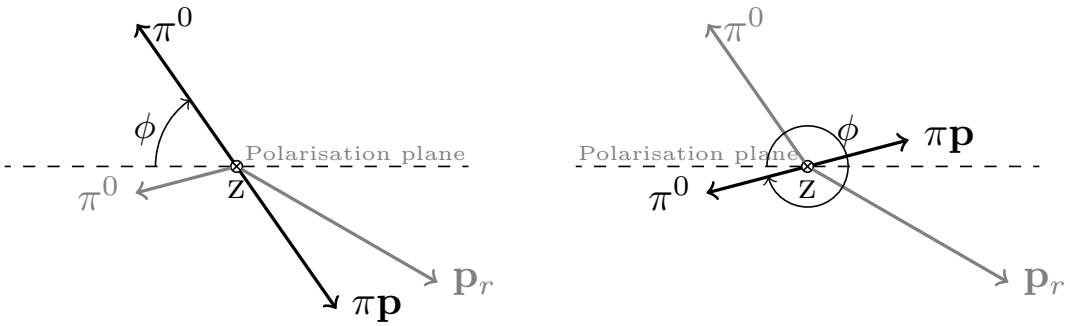

(a) First π^0 (b) Second π^0

Figure 2.16: Projection along the beam axis of the quasi two body system, showing the angle required to calculate Σ_π. Two indistinguishable configurations are both taken into account, each with half weighting.

lating to these processes are shown in figure 2.4. Because the π^0 meson is neutral there is limited final state interaction to be considered.

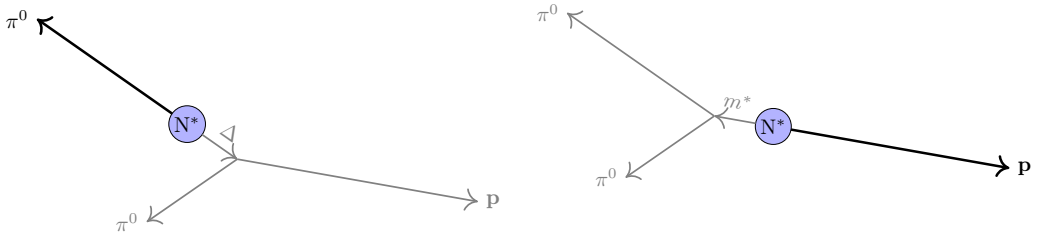

(a) Δ decay of N* (b) Vector meson decay of N*

Figure 2.17: N* decay channels contributing to the $2\pi^0$ photoproduction asymmetries. Left - The Δ intermediate state couples to the π^0 vectors. Right - The vector meson intermediate state couple to the proton vector.

2.4.3 I^s and I^c

The extension to the $2\pi^0$ decay allows the Σ observable to be decomposed into two orthogonal components, I^s and I^c, which can be considered as measurements of the sensitivity of the intermediate meson or (Δ, N*) resonance to the polarisation of the photon beam. The polarisation has been transferred from the beam to the photoproduced N* and subsequently onto the intermediate particle.

Analysis of the full three-body kinematics introduces an extra plane, the decay plane, which forms the angle Φ^* with the reaction plane as shown in figure 2.18.

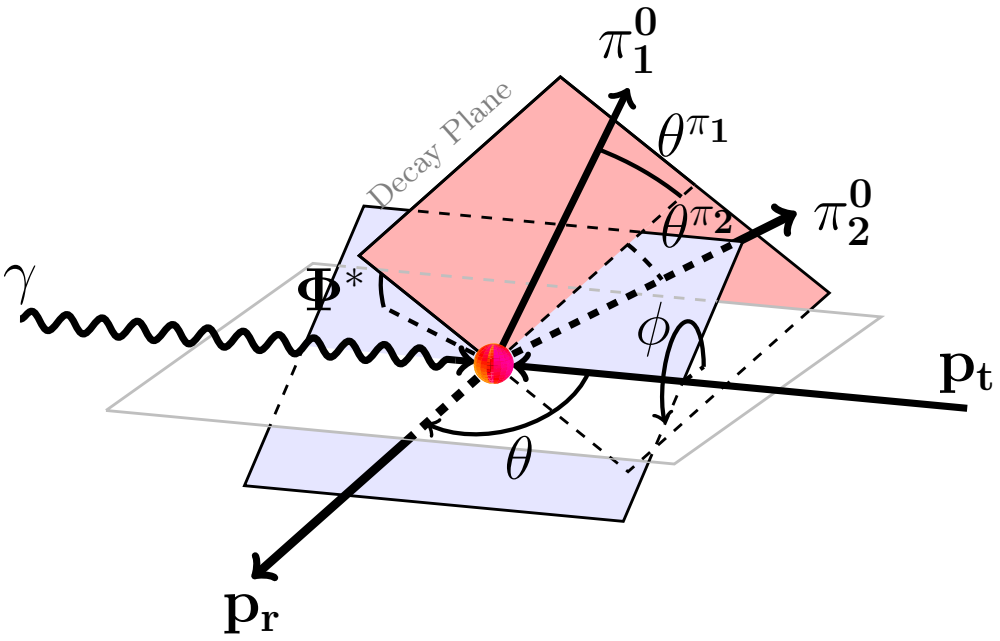

Figure 2.18: Full kinematic frame for $2\pi^0$ photoproduction off the proton in the $\pi\pi$ frame. White plane - Photon polarisation plane. Blue plane - Reaction plane, described by the proton target, recoiling proton and incident photon. Red plane - Decay plane, described by the three final state particles.

The angle Φ^* can be calculated from the vectors; $\vec{k}$, $\vec{p'}$, $\vec{p}_{\pi_1^0}$ and $\vec{p}_{\pi_2^0}$, which are respectively the 3-vectors of the tagged photon, recoiling proton and decay pions as,

$$\cos\Phi^* = \frac{\left(\vec{k}\times\vec{p'}\right)\cdot\left(\vec{p}_{\pi_1^0}\times\vec{p}_{\pi_2^0}\right)}{\left|\vec{k}\times\vec{p'}\right|\cdot\left|\vec{p}_{\pi_1^0}\times\vec{p}_{\pi_2^0}\right|} \tag{2.13}$$

with conditions such that,

$$\Phi^* = \begin{cases} \arccos(\cos\Phi^*) & \text{for} \quad \left(\vec{k}\times\vec{p'}\right)\cdot\vec{p}_{\pi_1^0} > 0 \\ -\arccos(\cos\Phi^*) & \textit{otherwise} \end{cases} \tag{2.14}$$

The previous measurement of the Σ observable is described by the integration of I^c over all Φ^* angles, where due to its anti-symmetry I^s integrates to 0.

The degrees of freedom in a 3-body system provide flexibility for all of the particles not to be restricted to having symmetry around the polarisation plane. When the

decay plane is not co-planar with the reaction plane (Angle $\Phi^* \neq 0$) a shift in the $\cos(2\phi)$ occurs. This is accounted for by the addition of the $\sin(2\phi)$ term to the differential cross section formula

$$\frac{\mathrm{d}\sigma}{\mathrm{d}\Omega}(\phi) = \left(\frac{\mathrm{d}\sigma}{\mathrm{d}\Omega}\right)_0 (1 + P^T(I^c \cos(2\phi) + I^s \sin(2\phi)), \tag{2.15}$$

where I^c and I^s now respectively define the contributions of the $\cos(2\phi)$ and $\sin(2\phi)$ terms[41]. As a function of Φ^*, observables I^c and I^s can respectively be expressed as cosine and sine series:

$$I^c(\Phi^*) = \sum_{n=0} a_n \cos(n\Phi^*) \tag{2.16}$$

$$I^s(\Phi^*) = \sum_{n=0} b_n \sin(n\Phi^*). \tag{2.17}$$

As with the Σ observable in $2\pi^0$ photoproduction, there are three reaction frames, one formed using the proton vector and two indistinguishable frames from the π^0 vectors. The angle Φ^*, defined in equation 2.13 relates to the proton vector, in the π^0 vector frames Φ^* can be calculated by circulating vectors $\vec{p'}$, $\vec{p}_{\pi^0_1}$ and $\vec{p}_{\pi^0_2}$ allowing separate measurements of both I^s and I^c to be made for the different frames. Angles θ and ϕ are taken directly from the frame vector.

Symmetry properties in I^c and I^s arise from treating the π^0s as indistinguishable. In the recoiling proton frame the π^0s have Φ^* angles 180° apart, and so each event has two valid definitions of the Φ^* angle. Both angles are weighted by half and result in a translational symmetry for $\Phi^* = \Phi^* + 180$. Taking the π^0 as the recoiling particle, the two indistinguishable frames provide events with half weights to the final distributions, there is no direct symmetry imposed in this frame.

Other symmetry properties arise from the definitions of I^s, I^c and Φ^*, independent of the frame. Under the mirror operator $\Phi^* \rightarrow -\Phi^*$,

$$I^c\left(\Phi^*\right) = I^c\left(-\Phi^*\right), \tag{2.18}$$

$$I^s\left(\Phi^*\right) = -I^s\left(-\Phi^*\right). \tag{2.19}$$

Having built an understanding of the observables measured in this analysis the next chapter covers how previous measurements of these polarisation observables have been made.

Chapter 3

Experimental Status

This chapter describes the experimental details and results of previous measurements made on the observables analysed for this thesis (section 3.1). The different approaches made by theory groups to fit the experimental partial wave measurements are covered in section 3.2.

3.1 Previous Measurements

This section discusses the previous measurements of the polarisation observable Σ for both single and double π^0 photoproduction channels and I^c and I^s in double π^0 photoproduction. For a comprehensive overview of the status of the partial wave analysis of hadrons see references [42, 17].

3.1.1 π^0 Photoproduction

Measurements of the photon asymmetry Σ in π^0 photoproduction have been investigated from as early as 1964[43]. Currently measurements have been made across a full range of polar angles with a range of photon energies from near the π^0 threshold[44] (E_γ=135 MeV), up to E_γ=6 GeV[45].

The most notable measurements of Σ which overlap with the photon energy region

of this work, 320 → 650 MeV, come from Mainz (Beck *et al.*[46, 37]) covering 240 → 440 MeV, GRAAL[47] covering 550 → 1500 MeV and Yerevan[48] covering 500 → 1100 MeV. There are additional notable measurements which complete the energy coverage from π^0 threshold (Mainz, Hornidge *et al.* 147 → 206 MeV[44]) up to the 4th resonance region (CBELSA 767 → 1680 MeV[49, 50]). The results produced in this analysis fill a gap in the previous experiments between the first and second resonance regions. The range of the measurements discussed is shown in figure 3.1.

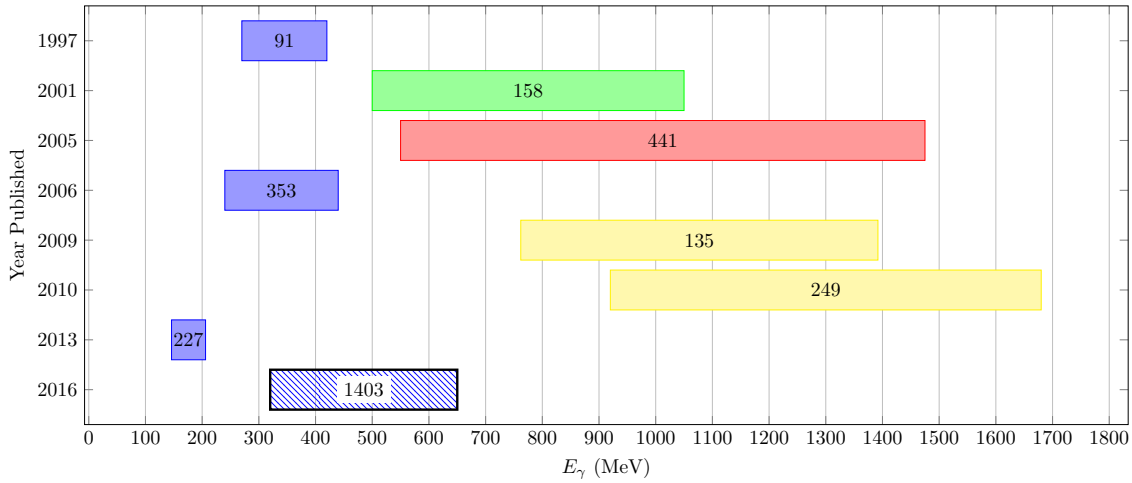

Figure 3.1: Previous measurements of the Σ observable in single π^0 photoproduction. The number in the box is the total number of measurements from the experiment. The boxes are colour coded by the facility in which the measurements were made; blue - A2 Mainz, green - Yerevan, red - GRAAL, yellow - CBELSA. The hashed box shows the range of measurements from this analysis.

Mainz - A2

The current experimental setup of the A2 experiment at Mainz is covered in detail in chapter 4. It is a coherent Bremsstrahlung facility, using an electron beam to generate high energy polarised photons from a diamond radiator (section 4.2.1). The experimental setup used in the previous measurements of Σ is laid out below.

The measurements by Beck *et al.*[46, 51] occurred prior to the MAMI C upgrade of the facility, when the detector setup in the A2 hall was configured differently. Before the upgrade, the electron beam energy was limited to 855 MeV, with the Glasgow

Tagger able to tag photons up to 800 MeV. The main detector system in the first of the two experiments was DAPHNE[52, 53] (Detecteur á grande Acceptance pour la PHysique photoNucleaire Experimentale). DAPHNE, is shown in figure 3.2 and was a multi-layered tracking detector with a full 2π azimuthal coverage with a lab polar angular acceptance of $21<\theta<159$ degrees. This experiment measured Σ at photon energies $270<E_\gamma<420$ MeV and with centre of mass polar angles $65<\theta_{cm}<125$ degrees.

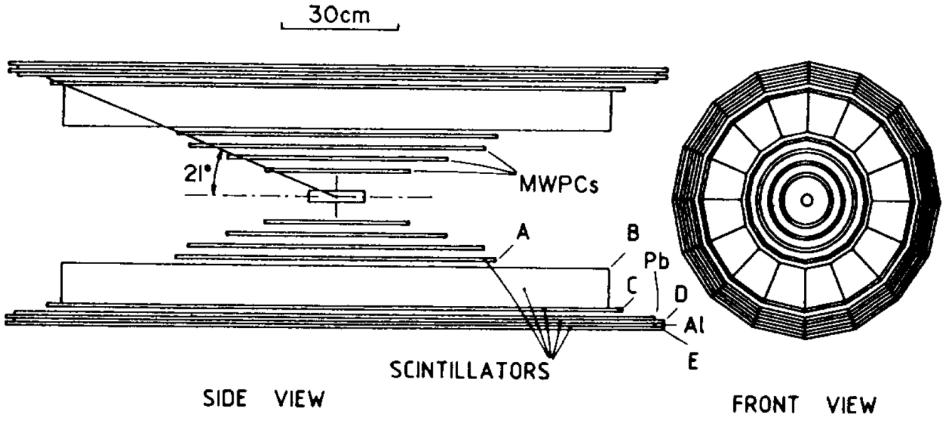

Figure 3.2: Multi-layered and segmented DAPHNE detector. Taken from reference [52].

The second Beck *et al.* experiment[51, 54] used a full BaF TAPS array, as shown in figure 3.3, see section 4.2.6 for further details. The TAPS array extended the polar angle range of the measurements $12<\theta_{cm}<170$ degrees but sacrifices the full 2π azimuthal acceptance. The measurements also improved on the photon energy range $240<E_\gamma<440$ MeV.

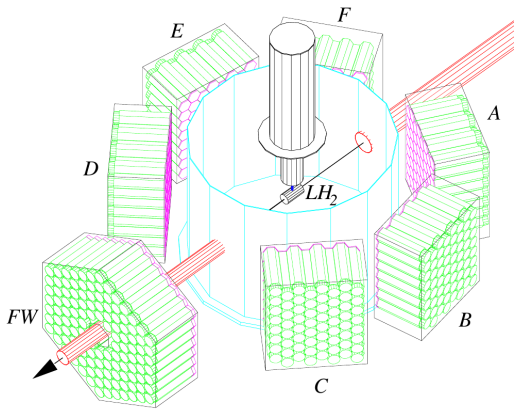

Figure 3.3: Array of BaF TAPS detectors as used in the A2 hall in 1995/1996, with results published in 2006. Taken from reference [54].

The measurements of Σ from these two previous experiments are shown in figure 3.4.

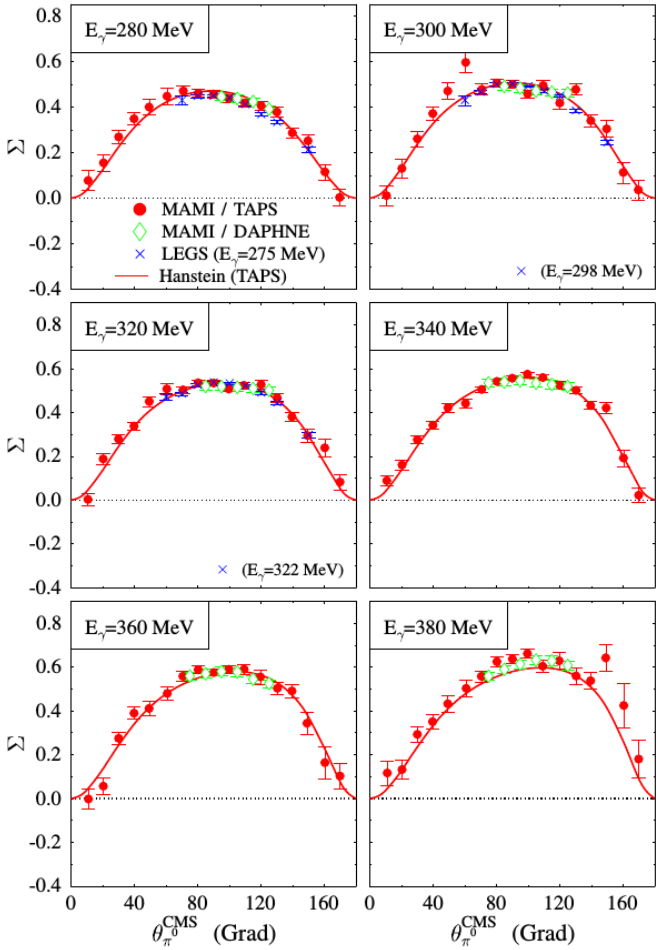

Figure 3.4: Measurements of Σ made by the TAPS and DAPHNE experiments. Taken from reference [51].

The detector configuration in the Hornidge *et al.*[44] experiment was identical to that used in the current measurement, although in covering the near π^0 threshold energy, the required electron beam energy was lower, so only the MAMI B accelerator was utilised at 855 MeV. The polarisation of the photon beam was tuned so that the coherent contribution was strongest between the π^0 threshold and 200 MeV, providing a degree of polarisation $50 \rightarrow 70\%$.

GRAAL

GRAAL (GRenoble Anneau Accélérateur Laser) uses laser back-scattering off electrons to produce high energy photons. Compton back scattering of laser photons retains their high original linear polarisation; the degree of polarisation measured at the GRAAL experiment peaks at 98%. The GRAAL detector system (figure 3.5) has 2π azimuthal acceptance and covers polar angles $0 < \theta < 155$ degrees in the lab frame.

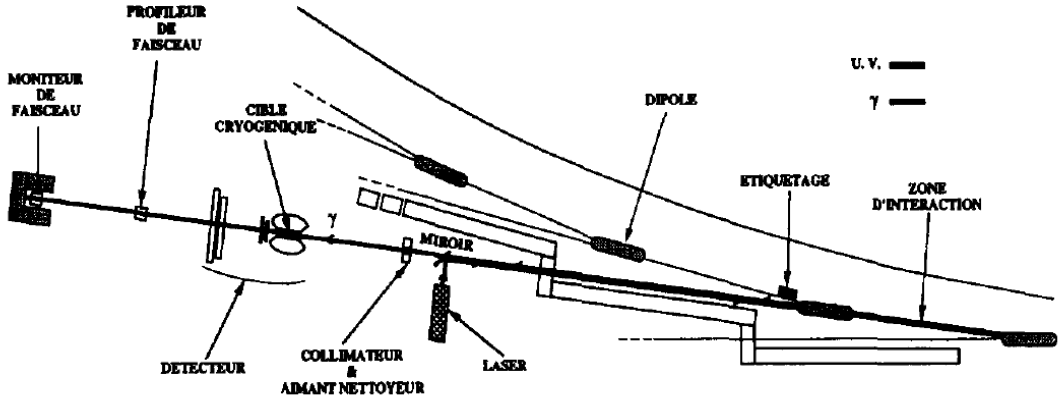

Figure 3.5: Setup of the GRAAL facility. Taken from reference [55].

The electron beam energy is 6.03 GeV, with the photons produced by two lasers, either a 514 nm, green laser or a 351 nm UV laser. The tagged range for the back scattered photons was $E_\gamma = 555 \rightarrow 1500$ MeV, matching the range of Σ measurements published in 2005[47].

Yerevan

Yerevan used a coherent Bremsstrahlung experiment, using a diamond radiator, polarised photons were created from the 4.5 GeV electron beam. Measurement of Σ from the Yerevan experiment covers the centre of mass angles $85 < \theta < 125$ in 5° bins between photon energies $0.5 < E_\gamma < 1.1$ GeV in bins of 25 MeV[48]. The limited angular acceptance compared to other discussed experiments comes from the two arm detector setup shown in figure 3.6.

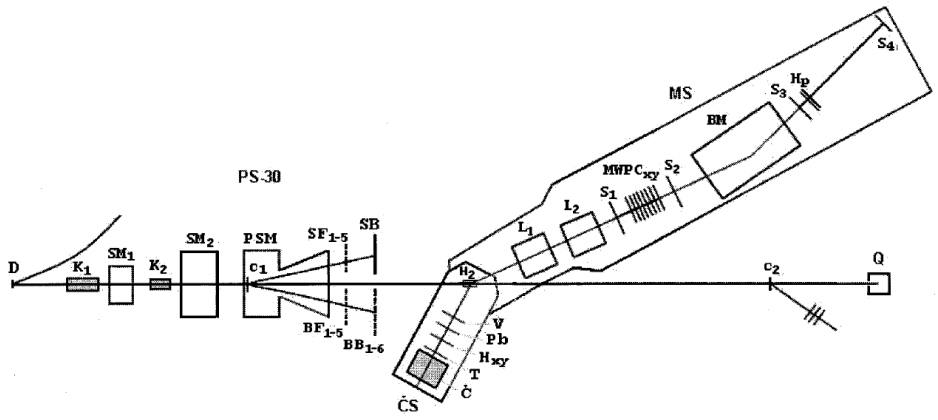

Figure 3.6: Two armed detector setup at Yerevan. Bremsstrahlung photons are produced in the diamond radiator at D; focused on the hydrogen target H_2. The forward angle arm of the detector was used to identify the recoil proton with the backwards angle Čerenkov detector identifying the π^0 decay γs. Taken from reference [48].

The Yerevan accelerator finished running in 1991 with analysis continuing for a number of years after.

CBELSA

CBELSA (Crystal Barrel at ELSA) where ELSA is the continuous beam electron accelerator located at Bonn has a setup similar to the A2 hall at Mainz. The ELSA accelerator provided a 3.175 GeV electron beam to a diamond radiator producing bremsstrahlung photons. The detector configuration is shown in figure 3.7 it consists of the crystal barrel, a highly segmented 4π calorimeter consisting of 1290 CsI crystals, and TAPS, covering the forward angles with a 528 hexagonal BaF_2 crystal array.

Two main sets of Σ measurements have been published from CBELSA, in 2009 [49] and 2010 [50] from data taken in 2003. These measurements cover the energy range $767 < E_\gamma < 1680$ MeV; helping identify and constrain the resonance contributions at energies above those presented in this thesis.

The development of additional technologies and computing power over the years has allowed experiments with increased precision and statistics to be conducted. Each

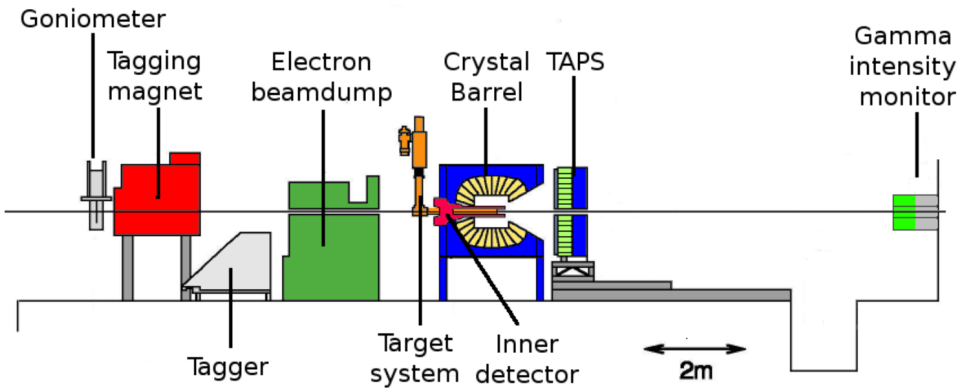

Figure 3.7: Experimental setup of the CBELSA experiment. Taken from reference [56].

additional measurement improves on the quality as well as the resolution of previous measurements.

3.1.2 Double π^0 Photoproduction

The $2\pi^0$ channel is more complicated to analyse. Only recently have accelerator and detector technologies made it viable to produce the statistics required to accurately measure polarisation observables from this channel. The first analyses of the $2\pi^0$ channel focused mainly on the total and differential cross sections of the process[57, 58, 59].

There are two experiments that have currently published values for the $2\pi^0$ photon asymmetry Σ; GRAAL[60] and CBELSA[61], with CBELSA also presenting values of I^s and I^c. Both of these experiments cover polarised photon energies higher than those covered in this work with GRAAL (2003) covering 650 $\rightarrow$ 1450 MeV and CBELSA (2015) covering 970 $\rightarrow$ 1650 MeV. Figure 3.8 is diagram of the current $2\pi^0$ measurements of Σ. The fine energy and theta binning presented for the π^0p decay channel can not be replicated with the same statistical accuracy in $2\pi^0$p decay measurements due to the significantly lower cross section.

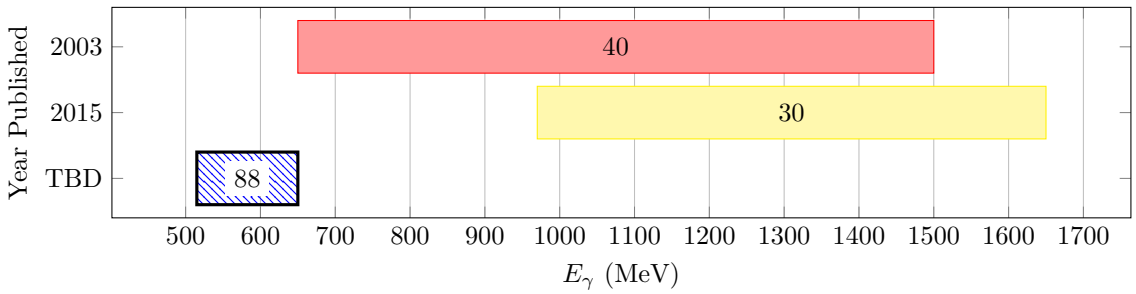

Figure 3.8: Measurement coverage of the Σ observable in double π^0 photoproduction. The number in the box is the total number of measurements from the experiment. The boxes are colour coded by the facility in which the measurements were made; blue - A2 Mainz, red - GRAAL, yellow - CBELSA. The hashed box shows the range of measurements from this analysis.

GRAAL

The GRAAL measurements of Σ[60] cover energies $E_\gamma = 650 \rightarrow 1450$ MeV, in four energy bins, with a full angular acceptance $0 < \theta_{cm} < 180$ degrees, divided into ten equal bins.

The results for the GRAAL analysis are presented in figure 3.9.

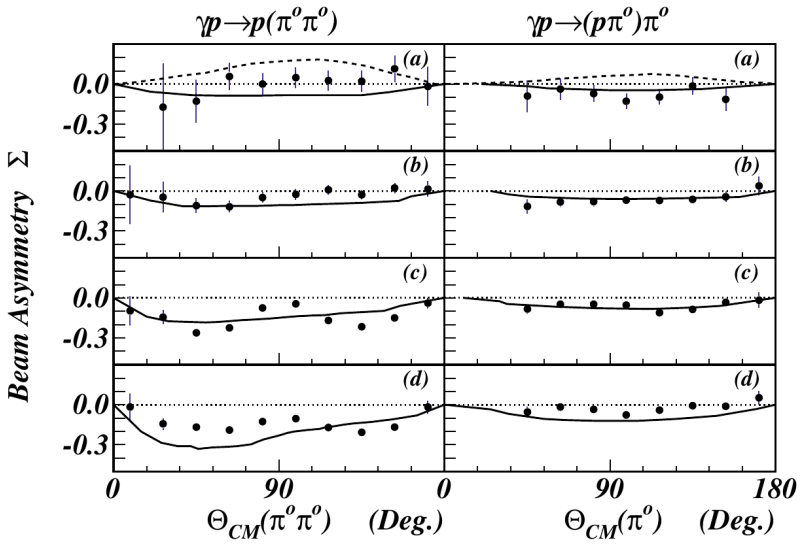

Figure 3.9: Σ measurements from the GRAAL analysis of the $2\pi^0$ reaction at beam energies: (a) 650-780 MeV, (b) 780-970 MeV, (c) 970-1200 MeV, (d) 1200-1450 MeV. Solid curve - predictions from an extension to the Laget model [62] discussed in reference [60]. Dashed curve - prediction of the Valencia model [63]. Taken from reference [60].

CBELSA

Results of the CBELSA $2\pi^0$ analysis are presented for Σ in figure 3.10 and I^s and I^c are shown in figure 3.11. The BnGa fit shown alongside the figures is discussed further in section 3.2.3. The measurements are presented in three energy bins across the range $E_\gamma = 970 \rightarrow 1650$ MeV, the values in the lower two bins are in good agreement with the previous measurements from the GRAAL analysis.

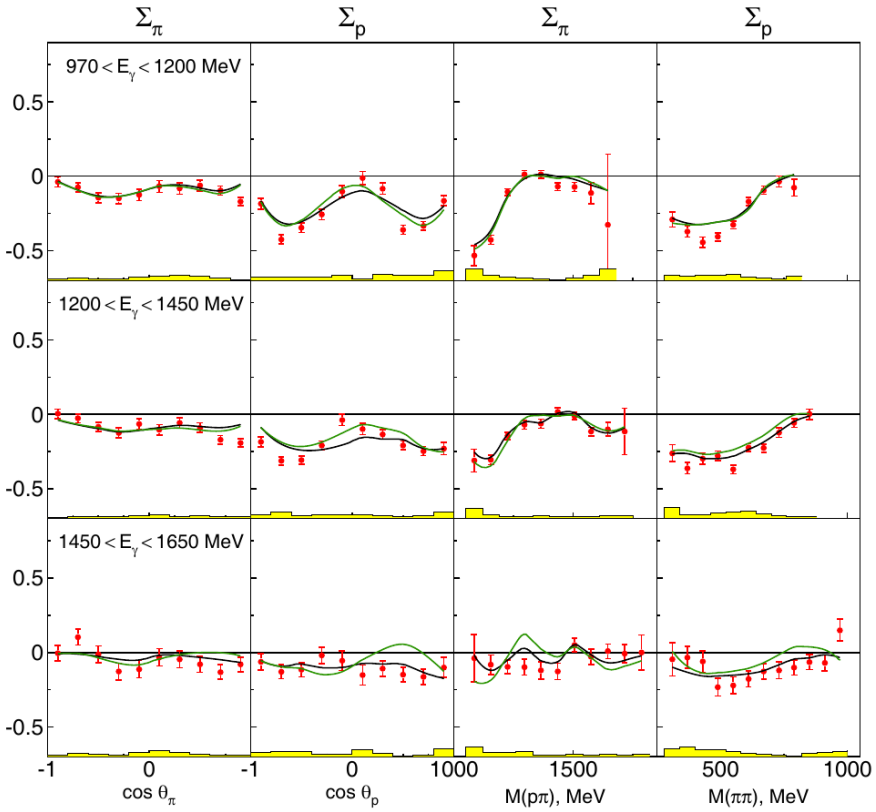

Figure 3.10: Σ measurements as a function of $\cos\theta$ and the invariant mass of particle pairs, from the CBELSA analysis of the $2\pi^0$ reaction. Black curve - BnGa PWA fit. Red curve - BnGa PWA fit without N(1900)$3/2^+$. Taken from reference [61].

Note the values of Σ_p in figure 3.10 have been presented as a function of the polar angle of the proton whereas in the results of the GRAAL analysis (figure 3.9) they were presented as a function of the polar angle of the $\pi\pi$ system.

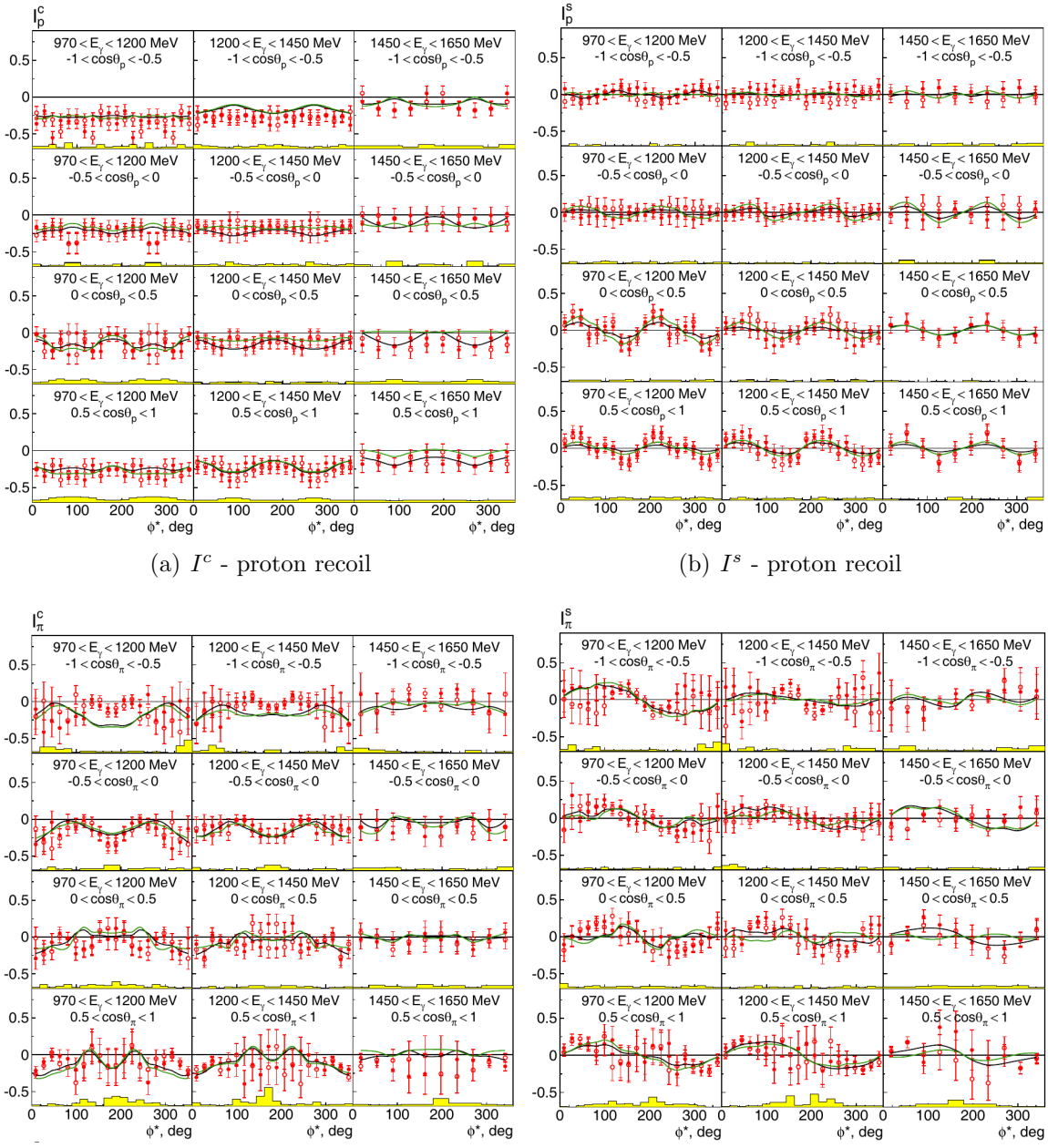

(a) I^c - proton recoil

(b) I^s - proton recoil

(c) I^c - π recoil

(d) I^s - π recoil

Figure 3.11: I^c and I^s measurements as a function of $\cos\theta$ from the CBELSA analysis of the $2\pi^0$ reaction. Black curve - BnGa PWA fit. Red curve - BnGa PWA fit without N(1900)$3/2^+$. Taken from reference [61].

The next section discusses how experimental cross section data and polarisation observables are used to build predictive models of the nucleon resonance spectrum.

3.2 Experimental Interpretations

Different approaches can be taken to estimating the amplitudes and resonance contributions of the complex reaction wave. Partial Wave Analysis (PWA) groups have conducted multipole fits to the experimental results. This then allows the behaviour of the multipoles as a function of centre-of-mass energy to be determined; subsequently producing a model which describes the relative resonance contributions.

3.2.1 MAID

The MAID collaboration uses an unitary isobar model[64, 34] to approximate the excitation spectrum of the nucleon. The model uses the well measured 4-star N^*/Δ resonances from the PDG database[21] up to a mass of 1.8 GeV.

A resonance's quantum numbers describe its partial wave form with the energy dependence of its magnitude modelled by a Relativistic Breit–Wigner. The pole position energy and width of resonances are taken from the PDG database. MAID fits the Breit–Wigner dependent partial waves to measurements of differential cross sections and polarisation observables.

The model provides predictions for reaction differential cross sections and polarisation observables in both single π^0 photo- and electro-production[34] along with double π^0 photoproduction [31]. The published MAID models are of limited use having not been updated for many years, with the single π^0 fits carried out in 2007, and the $2\pi^0$ model in 2004.

The $2\pi^0$ fit was carried out with no polarisation observable measurements and only limited total cross section data available. The only free parameter in the fit was included to account for final state interactions (FSI), all other coupling mechanisms were taken from the MAID single π^0 fit or the PDG database. Figure 3.12 shows the results of the fit, demonstrating there was need for further improvement of the model even at the time it was carried out.

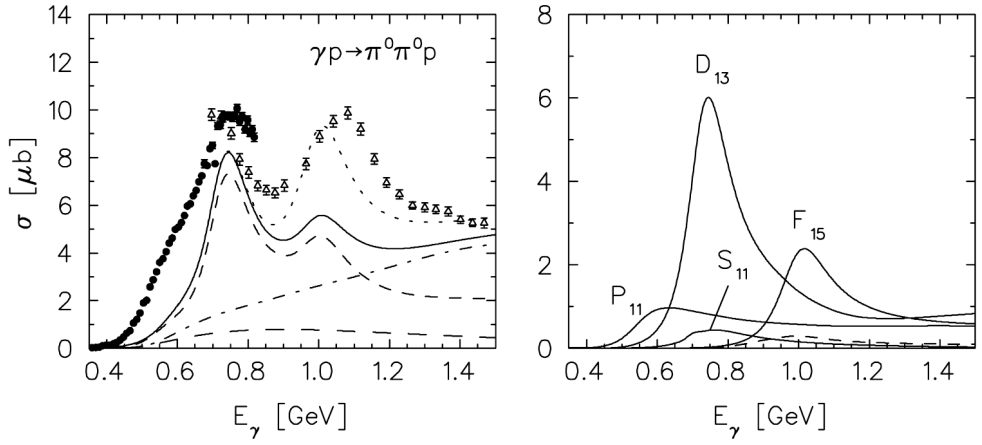

Figure 3.12: Left - MAID Prediction for the total cross section for $\gamma p \rightarrow \pi^0\pi^0 p$, experimental data is shown as points and contributions from different Feynman diagrams are shown as lines. Right - Resulting resonance contributions. Additional details can be found in the original source[31].

Both MAID predictions are accessible from a web interface. The fits presented along with the results have been produced with an updated version of the $2\pi^0$ code[65] which slightly changes a couple of the observable predictions.

3.2.2 SAID

SAID (Scattering Analysis interactive dial-in) is a partial wave analysis, directly fitting contributions that can be attributed to partial waves of resonance multipoles to measurements. A partial wave analysis has the advantage of being model independent with resonance positions and widths not used as inputs, instead, resonances become apparent from peaks in the continuous distributions of the partial waves described as a function of centre-of-mass energy

The SAID PWA is fitted using the world dataset of older πN scattering measurements, as well as more recent measurements coming from photoproduction of pions.

The most recent SAID fit *PR15*[66] was published in 2015 alongside measurements of the $\gamma p \rightarrow \pi^0 p$ differential cross section which were measured in A2 at Mainz. Figure 3.13 shows the values of partial wave coefficients resulting from the fit, coming from equation 7.2 used to fit the results for this thesis. It should be noted that the

values of the lowest coefficients are well constrained and in good agreement between predicted models while there is a larger degree of uncertainty in the higher order terms.

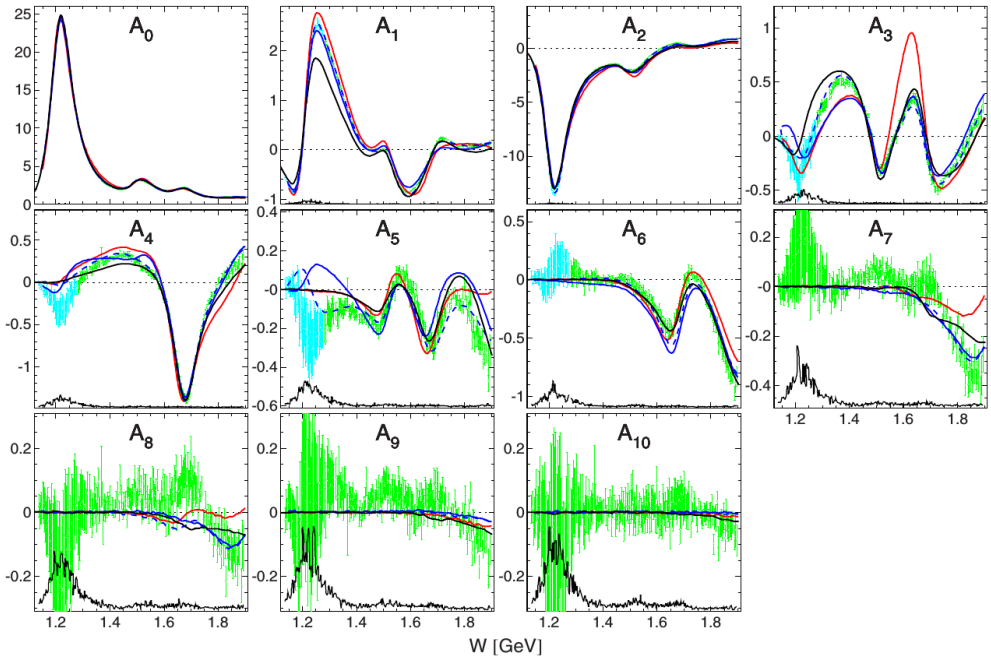

Figure 3.13: Partial wave coefficients from the SAID fit to π^0 polarisation observable and differential cross section measurements. Points - cyan shows the fit of Legendre polynomial up to order six, green shows the fit of Legendre polynomial up to order 10. Lines show predictions from SAID (blue), MAID (red) and Bonn-Gatchina (Black). A full descriptions of the different lines and points can be found in the original source[66].

SAID PWA predictions can be accessed via their web interface[67] where there is also a database of previous experimental measurements of polarisation observables and differential cross sections. SAID does not provide predictions for $2\pi^0$ photoproduction reactions.

3.2.3 Bonn-Gatchina

The Bonn-Gatchina fit, like SAID, is a partial wave analysis constrained by the world dataset of differential cross sections and polarisation observable measurements. Whereas the SAID fit uses mainly measurements from πN scattering and π photoproduction, the Bonn-Gatchina PWA is a coupled channel fit using measurements

from additional reactions to constrain the parameters of the fit[68, 42].

The most recent fit from the Bonn-Gatchina group is the BG2014-02[56] fit, this simultaneously provides predictions for both π^0 and $2\pi^0$ photoproduction channels.

The data collected for this thesis provides a statistical accuracy beyond any of the previous measurements and so is expected to help further constrain the PWA models. The details of the detector setup, which was used in the production of the data, is discussed in the next chapter.

Chapter 4

Experimental Setup

Approved by the Mainz PAC in 2005, this experiment ran between 16th of September to the 6th of October 2008 in the A2 Hall at MAMI. The experimental proposal originally targeted making measurements of double-polarisation observables $C_{x'}$[69] and $O_{x'}$, single-polarisation observables P and T for the first time as well as measurements of Σ with a significantly improved statistical accuracy than previously determined for π^0 production. The experiment has a high degree of linear polarisation at the tagged photon energies which coincide with the threshold for $2\pi^0$ production, this allows measurements of linear polarisation observables in $2\pi^0$ photoproduction to be made in a previously unexplored region.

This chapter outlines the accelerator facilities at Mainz, the setup in the A2 Experimental Hall including the production and tagging of the photon beam, the hydrogen target, and the main CB and TAPS detectors with a brief description of the subdetectors used for particle identification. Calibration of the detectors is discussed in chapter 5.

4.1 MAMI Facility

The MAinzer MIcrotron (MAMI)[70, 71, 72] is located in the Institut für Kernphysik at Johannes Gutenberg University Mainz. MAMI is capable of providing a

continuous-wave electron beam with energies up to 1.6 GeV to four experimental halls.

Originally built in 1979, MAMI has undergone a number of upgrades before reaching its current configuration. The most recent refurbishment in 2005 saw the accelerator nearly double in energy, moving from an endpoint electron energy of 855 MeV to energies of up to 1.6 GeV. The layout of the MAMI accelerator facility and experimental halls is shown in figure 4.1.

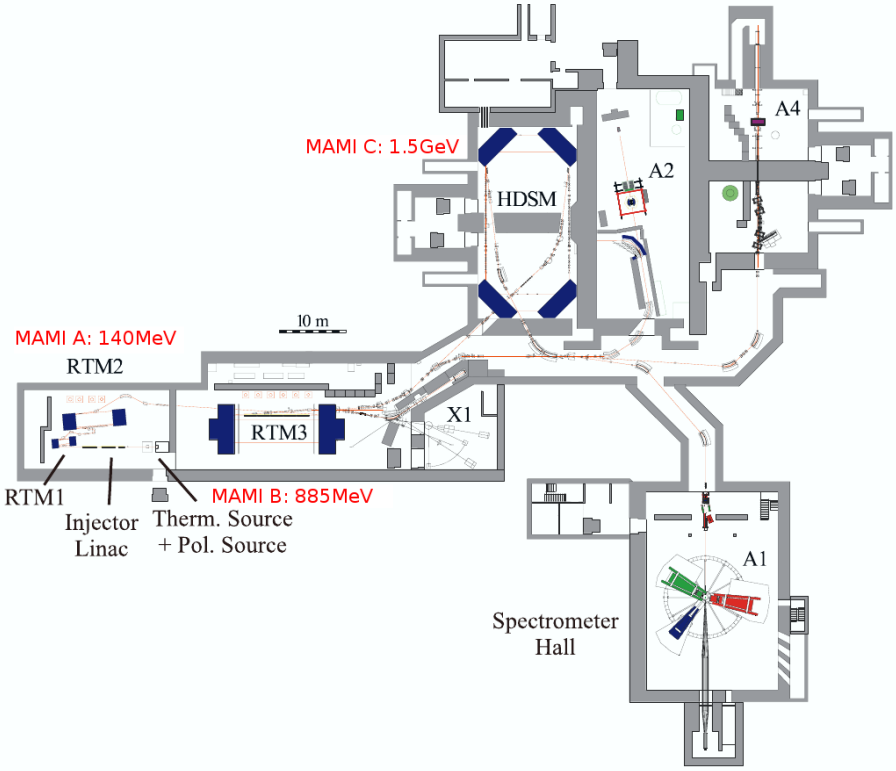

Figure 4.1: The MAMI accelerator facility. MAMI A, MAMI B and MAMI C make up the continuous-wave electron accelerator. Experimental halls A1, A2, A4 and X1 are supplied by the multistage electron accelerator. Taken from reference [71].

The accelerator consists of three main modules, MAMI A, MAMI B and MAMI C providing a tunable, mono-energetic, continuous electron beam. A summary of the main components that make up MAMI is laid out in table 4.1.

MAMI A is the first stage of the accelerator; it consists of a highly polarised electron source[73], injector Linac (LINear ACcelerator) and two RTMs (RaceTrack Microtrons[74]) MAMI A1 and MAMI A2. Polarised electrons are evaporated off a

Accelerator	Component	Field Strength (T)	Endpoint Energy (MeV)
MAMI A	Polarisation Source		0.511 (m_{e^-})
	Injector Linac		3.97
	A1 RTM	0.1026	14.86
	A2 RTM	0.5550	180.1
MAMI B	B RTM	1.2842	855
MAMI C	HDSM	1.53-0.95	1500

Table 4.1: Summary of MAMI accelerator modules.

GaAsP cathode illuminated with a Xenon light source which has been monochromatic wavelength selected and circularly polarised. The evaporated electrons are then accelerated by the injector linac into the RTM rings where they are further accelerated.

MAMI B consists of a single RTM accelerating the beam up to 855 MeV.

A RTM consists of a linac and two magnets. The name racetrack microtron comes from the way the electron is recirculated a number of times through the linac by careful tuning of the magnetic fields. Figure 4.2 shows a simple diagram of a RTM.

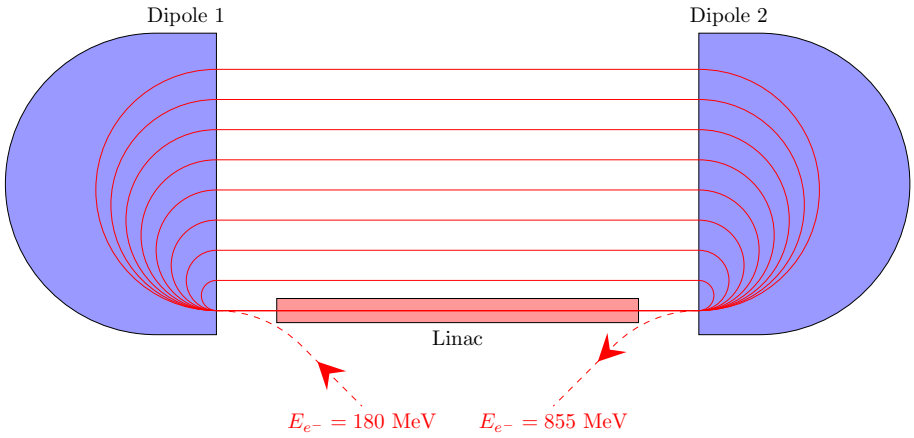

Figure 4.2: MAMI-B. Racetrack microtron, consisting of a linac and two dipole magnets.

MAMI C is the final module of the accelerator, made of an HDSM (Harmonic Double Sided Microtron) which consists of two linacs and four magnets (Figure 4.3). In order to achieve the 1.5 GeV beam energy, a RTM was no longer considered a reasonable option due to the size and strength of the magnets required to bend the high energy beam around 180°, instead, the four smaller magnets of the HDSM achieve the same effect within the restricted space.

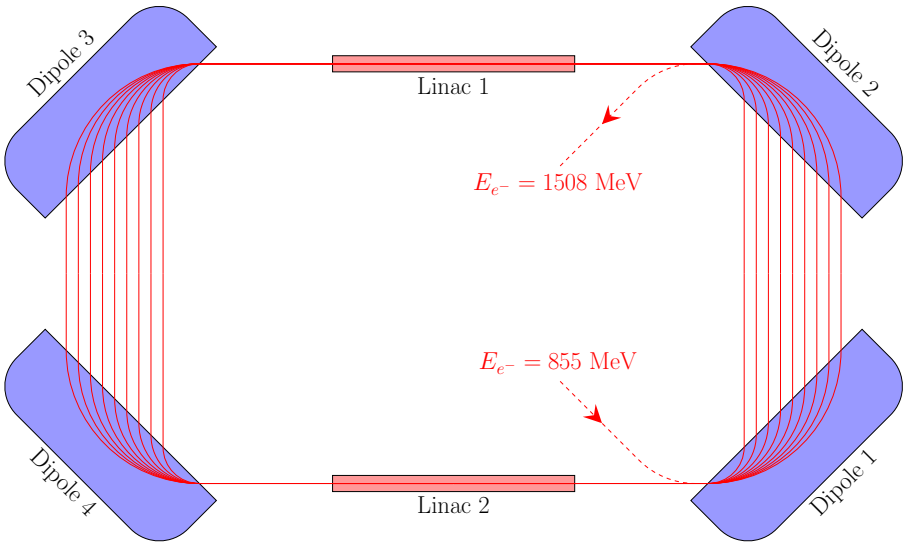

Figure 4.3: MAMI-C. Harmonic double sided microtron, consisting of two linac and four dipole magnets.

At 1.5 GeV the electron beam has a 1σ energy spread of only 110 keV propagating a small statistical energy uncertainty of $\sim$ 0.001% to experimental results. The electron beam maintains a high level of polarisation through the MAMI accelerators, arriving into the hall around 80% circularly polarised for the duration of this experiment. The electron beam polarisation however does not effect the analysis presented in this thesis so shall not be discussed further.

4.2 A2

The data were taken in the A2 Experimental Hall, which is dedicated to high precision nuclear experiments with real photons. Figure 4.4 shows the detector setup in the hall, this is focused on providing coverage of 98% of 4π acceptance in the lab frame. The components of the experiment are described in detail in the this section.

Details of how the signals from each detector are used are discussed in chapter 6.

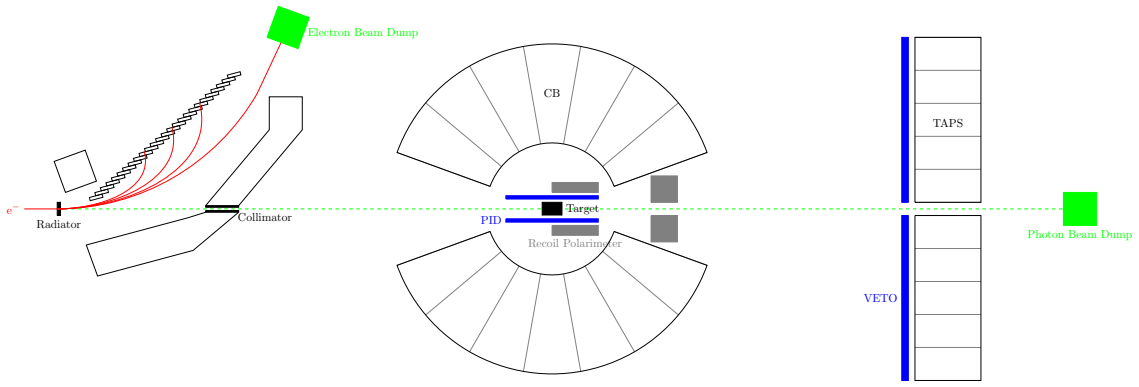

Figure 4.4: Schematic diagram of the experimental setup in the A2 hall for the current beamtime.

4.2.1 Bremsstrahlung

The A2 experiment produces high energy real photons via the bremsstrahlung process.

As the electron beam passes through a radiator, some of the electrons interact with the electromagnetic field of an atomic nucleus, deflecting them from their path (Figure 4.5). The energy lost in this interaction is emitted as a photon and termed Bremsstrahlung (*breaking radiation*).

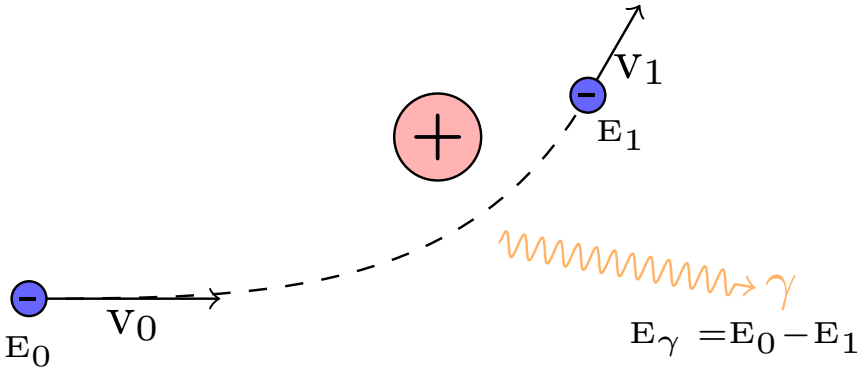

Figure 4.5: Bremsstrahlung process diagram. Bremsstrahlung (deceleration radiation) occurs when a charged particle is deflected in the nuclear field. High energy photons are created with energy equal to that lost by the decelerating electron.

The bremsstrahlung interaction is mediated by a single virtual photon via either of the processes described by the Feynman diagrams shown in figure 4.6.

The energy radiated is directly related to the energy of the beam electron and its

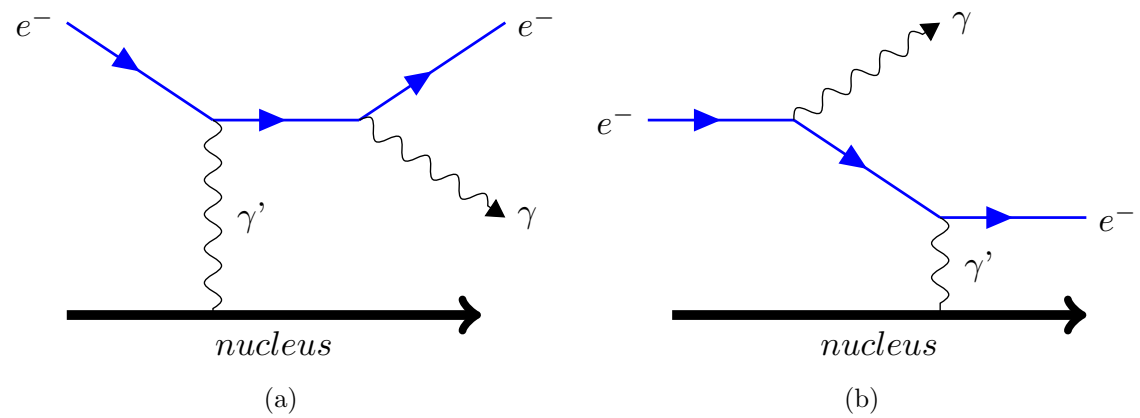

Figure 4.6: Feynman diagrams of the two main processes that produce bremsstrahlung radiation.

impact parameter(r) on the nucleus. The nucleus provides a central electromagnetic field and as such, the force felt by an electron relates to the inverse of the impact parameter $1/r$; this creates the range of energies observed from the process. The distribution of electrons interacting with impact parameter r decreases with $1/r$ leading to the approximate relation,

$$N(E_\gamma) \propto 1/E_\gamma, \tag{4.1}$$

where $N(E_\gamma)$ is the number of bremsstrahlung photons expected with energy E_γ. This gives the distinctive distribution of energies associated with bremsstrahlung radiation (Figure 4.7(a)).

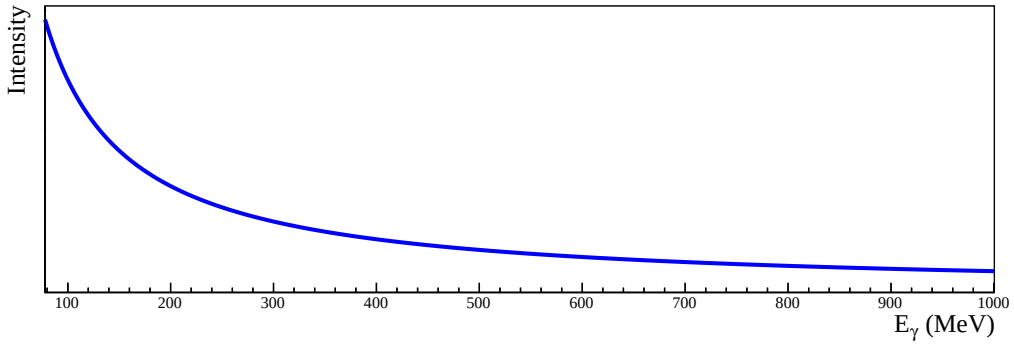

(a) Amorphous Bremsstrahlung

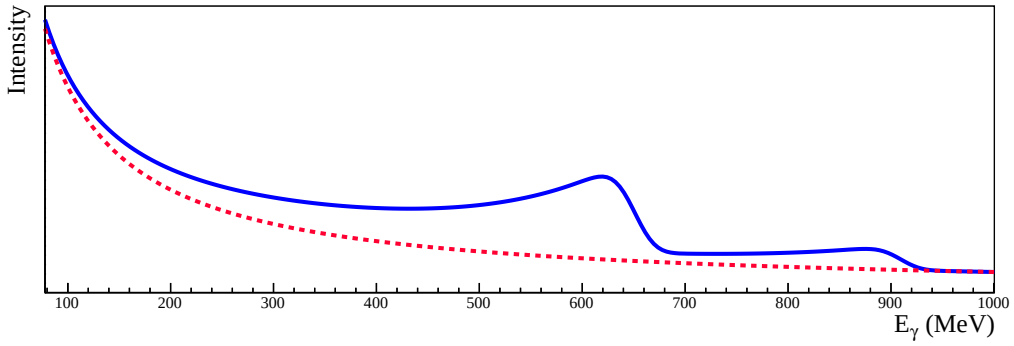

(b) Coherent Bremsstrahlung

Figure 4.7: Theoretical energy spectrum of bremsstrahlung photons produced with a 1508 MeV electron beam. Top - Using an amorphous radiator (e.g. copper). Bottom - Using an aligned coherent radiator (e.g. diamond), red signifies the incoherent contribution.

The use of a radiator with a lattice structure, such as diamond, introduces strong directional planar fields[75, 76]. Electrons have a probability of interacting with the field of one set of lattice planes (*reciprocal lattice vector*) as opposed to individual nuclei. These interactions present as an enhancement over the amorphous Bremsstrahlung spectrum. The energy at which this coherent enhancement is observed depends on the angle of impact the beam makes with the lattice plane. Figure 4.7(b) shows an example of the resulting coherent enhancement of the Bremsstrahlung spectrum.

The coherent component of the Bremsstrahlung spectrum consists of photons with a high degree of linear polarisation, from the momentum transferred with the directional field of the lattice planes opposed to the isotropic field of a single nucleus. The electric vectors of the planes of nuclei in the coherent radiator sum up to a di-

rection perpendicular to the lattice plane. Momentum transfer between the electron and radiator is preferentially perpendicular to the lattice plane. Further discussion on the calibration of the diamond to achieve high linear polarisation at particular energies is found in section 5.3.

4.2.2 Goniometer

A selection of radiators are available for the A2 experiment, these are mounted in a goniometer which allows them to be remotely swapped. The diamond radiator is mounted in the centre of the wheel and can be orientated to any angle to allow the setting of the coherent peak for beam polarisation[77]. The full selection of radiators and their functions are laid out in table 4.2 and shown in figure 4.8.

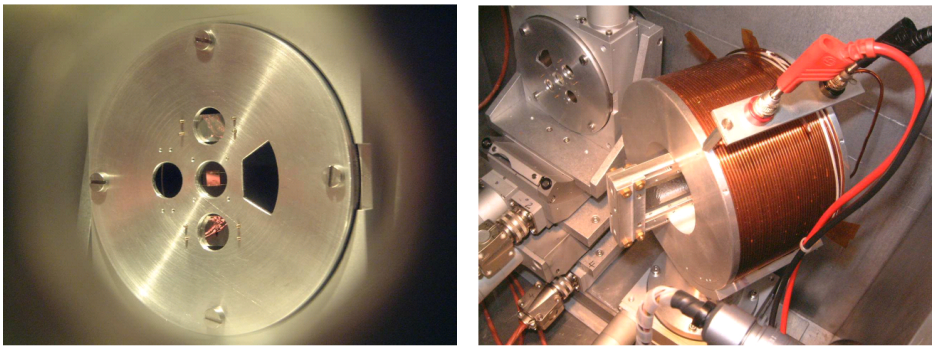

(a) Goniometer Wheel (b) Møller Coil

Figure 4.8: The goniometer contains a selection of radiators for producing photons with different properties or for performing detector tests and calibrations. Taken from reference [78].

Radiator	Thickness	Function
Copper	12 μm	Amorphous bremsstrahlung photon production
Diamond	30 μm	Linearly polarised bremsstrahlung production
Møller coil		Measuring photon circular polarisation
Blank		Beam optimisation and tests

Table 4.2: Radiators available to the A2 experiment.

4.2.3 Glasgow Tagged Photon Spectrometer

The A2 experimental setup is a tagged photon experiment in which a measurement of each photon's energy is made by detecting the corresponding degraded electron in coincidence with the photon triggered event. Measurement of energy and time of the degraded electrons is done with the Glasgow Tagging Spectrometer[79].

The tagger system (Figure 4.9) consists of a 1.8 T dipole magnet[80] and a focal plane detector (FPD) with 353 scintillators. Details of the FPD setup are discussed in 4.2.3 while its calibration is covered in section 5.2.1.

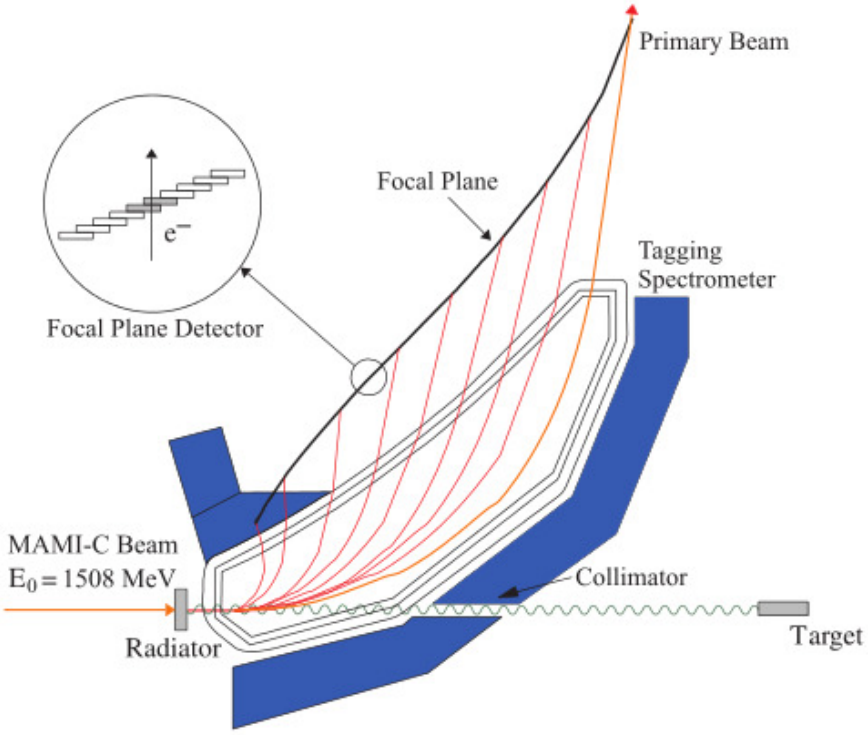

Figure 4.9: Schematic diagram of the Glasgow photon tagger systems. Taken from reference [78].

The tagger measures the electron energies after they have passed through the radiator, losing energy as bremsstrahlung. The difference between the energy of the detected electron (E_d) and the beam energy supplied by MAMI (E_0) is the energy of the bremsstrahlung photon (E_γ). This is simply given by

$$E_\gamma = E_0 - E_d. \tag{4.2}$$

Theoretical distributions of bremsstrahlung photons were shown in figure 4.7. Due to differences in the efficiency of each tagger channel, the observed spectrum does not vary so smoothly, the flux across the tagger range for diamond and copper example data files are shown in figure 4.10.

Data taken with the amorphous radiator was not used in the calculation of polarisation observables however it was key in determining the coherent enhancement, this is discussed further in section 5.2.1. Each tagger channel's efficiency can change during the course of a beamtime. In order to minimise the effects on the calculation of polarisation, periodic amorphous runs are made allowing for most accurate calculation of enhancement to be made.

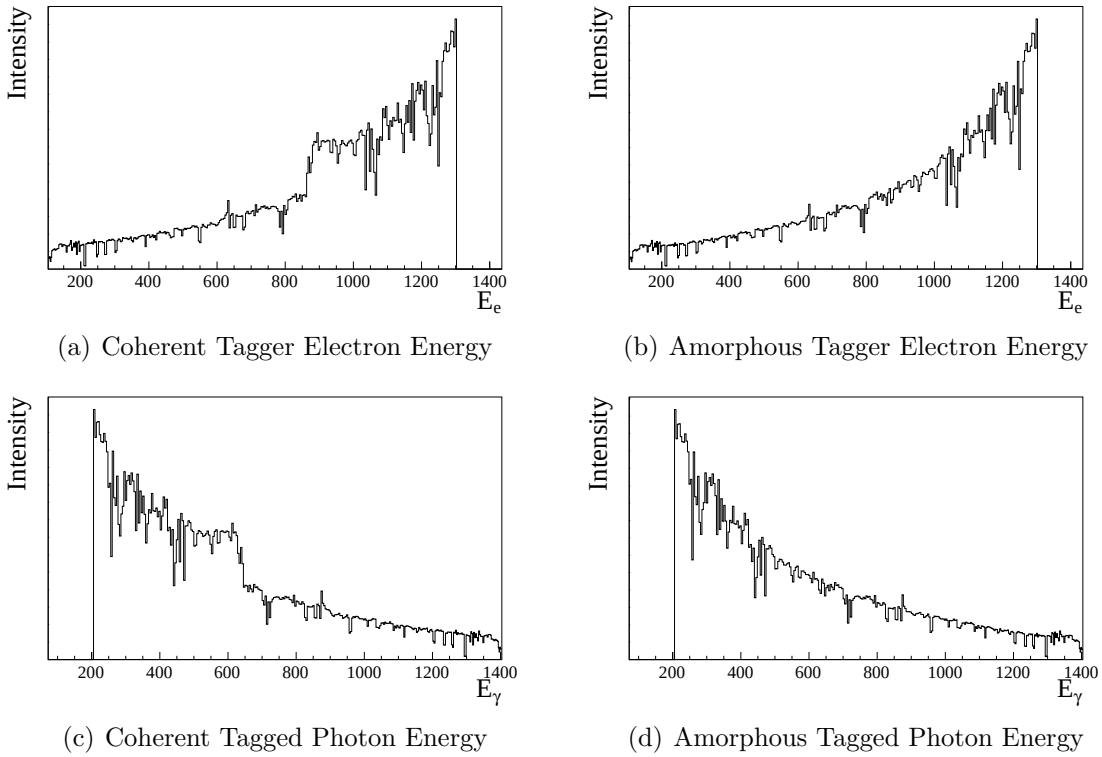

(a) Coherent Tagger Electron Energy

(b) Amorphous Tagger Electron Energy

(c) Coherent Tagged Photon Energy

(d) Amorphous Tagged Photon Energy

Figure 4.10: The flux of electrons hitting each Tagger channel in tagger channel energy (top) and in tagged photon Energy (bottom). The lowest energy channels in the tagger were turned off outside of the energy region of interest to reduce the total counts and trigger rate.

Photons which have a corresponding electron detected in the tagger, determining its energy and time, are considered to be tagged, and are recorded within a wide time window opened by the experimental trigger from the detector systems. The

beam current during production running is such that several photons will be tagged and recorded within the timing window of any triggered event. Because there are many more tagged photons than triggered reactions, multiple photons in the trigger timing window will be attributed to that event. With a large statistical sample, a clear peak can be seen in a broad timing window recorded each side of a triggered event. The peak relates to the higher probability of having tagged a photon at the time coincident to the opening of the trigger. In fact at least one tagged photon for each event is expected in the prompt peak. Figure 4.11 shows a typical calibrated timing coincidence spectrum.

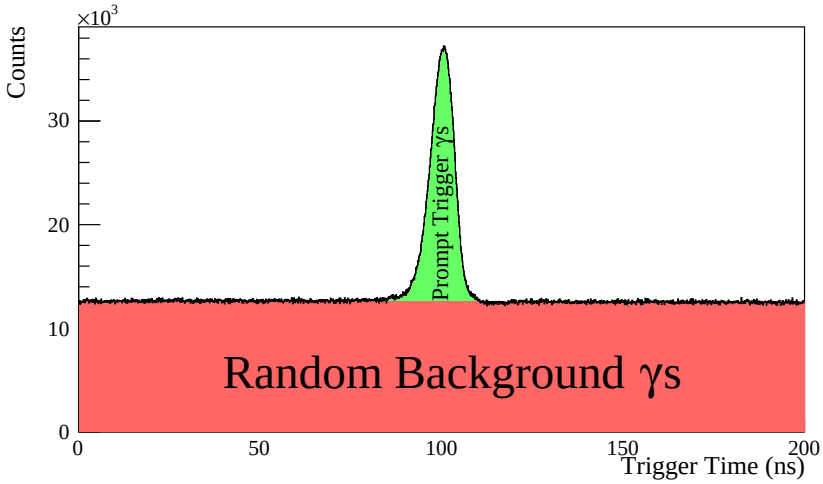

Figure 4.11: Coincidence timing between the tagger and detector trigger. The peak at 100 ns corresponds to the increased probability of having a photon tagged in the coincidence region associated with the triggered event.

A delay is created in tagger signals reaching the Data Acquisition (DAQ) compared to the detector signals. This allows a trigger window to be opened by the detectors, telling the DAQ to record tagged photons spanning the range either side of the prompt photon peak.

Processes other than single photon bremsstrahlung may also occur in the radiator and are considered background. Reactions such as Møller scattering and pair production will create multiple signals in the Tagger with no matching high energy photon, whereas multiple Bremsstrahlung scattering processes in the radiator will produce additional photons but result in a detected electron which doesn't match in energy. These additional signals from the tagger are a statistical background

and removed along with the photons that did not trigger a recorded reaction in the random coincidence subtraction (Section 6.4.1) or a missing mass fit (Section 6.4.2).

Focal Plane Detectors

The focal plane of the tagger detects the deflected beam electrons, it is built from 353 overlapping plastic scintillators each with a photomultiplier tube (PMT), giving 352 coincidence channels [79, 81]. A signal detected in two neighbouring scintillators in coincidence is taken as a hit in the tagger channel.

Figure 4.12 shows examples of signals that may be detected by the FPD with only an e^- from the tagger magnet plane producing the coincidence signal passed onto the DAQ. The coincidence required between neighbouring scintillators greatly reduces the number of signals being generated from background noise in the electronics and particles generating a signal in the scintillator from out of the tagger magnetic field plane.

The FPD can tag photons with energies spanning $\sim 5-93\%$ of E_0 with each channel covering a region of ~ 3.75 MeV at beam energy of $E_0 = 1508$ MeV.

Each scintillator is a cuboid, shown in figure 4.12(b), with a length of 80 mm, a thickness of 2 mm and a width between 9 mm and 32 mm. The width of the face that is angled towards incident electrons decreases along the focal plane so that each channel relates to an energy bin of roughly the same width.

Each detector has a PMT attached to the top, out of the focal plane to reduce radiation damage. Amplification and channel coincidence electronics are located directly at the focal plane to get the fastest time response and resolution. The timing resolution of the tagger coincidence channel has a FWHM of 0.37-0.53 ns [79].

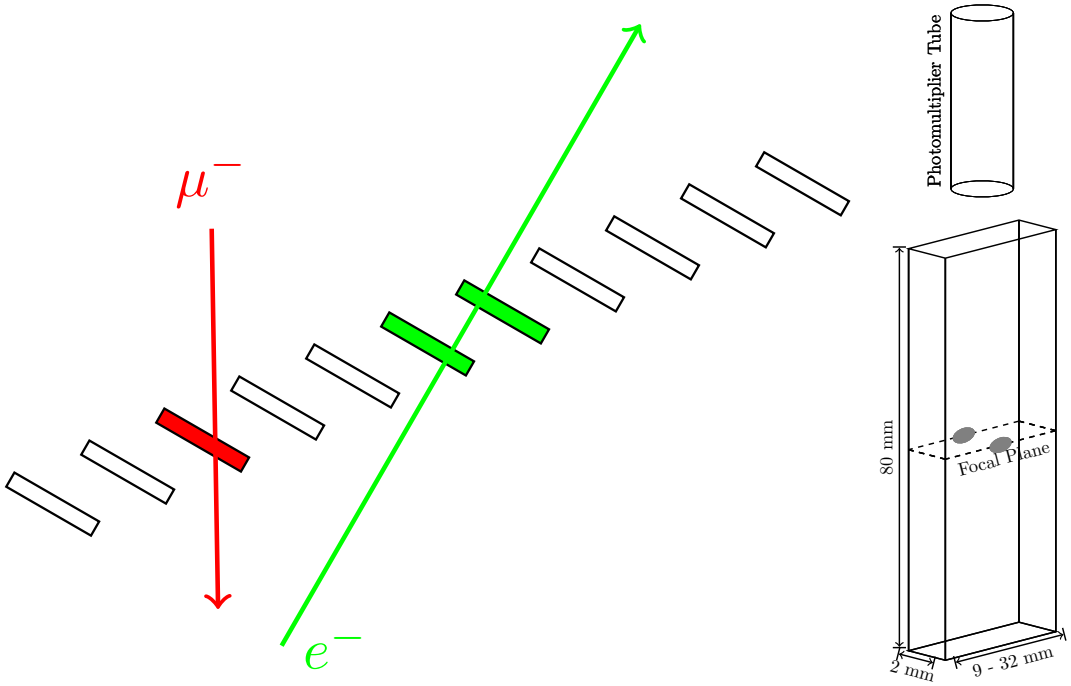

(a) Focal Plane section

(b) FPD Plastic Scintillator

Figure 4.12: Left - Focal Plane Detector section showing a coincidence event from a beam electron in green and a background event from a cosmic muon which doesn't pass a neighbouring channel coincidence. Right - Dimensions of a single plastic scintillator.

Photon Beam Collimator

The Pb collimator limits the angular spread of photons produced in the radiator that reach the target, restricting the beam to a narrow cone.

The radiation produced through coherent bremsstrahlung is more forward focused than incoherent processes; collimation of the beam helps to increase the photon beam degree of polarisation on the target[82].

The collimator for this experimental run chosen was 3 mm in diameter, sitting 3 m from the radiator and 8.3 m prior to the target. The photon beam was collimated so that the beam has a diameter of about 1.1 cm at the target, shown in figure 4.13.

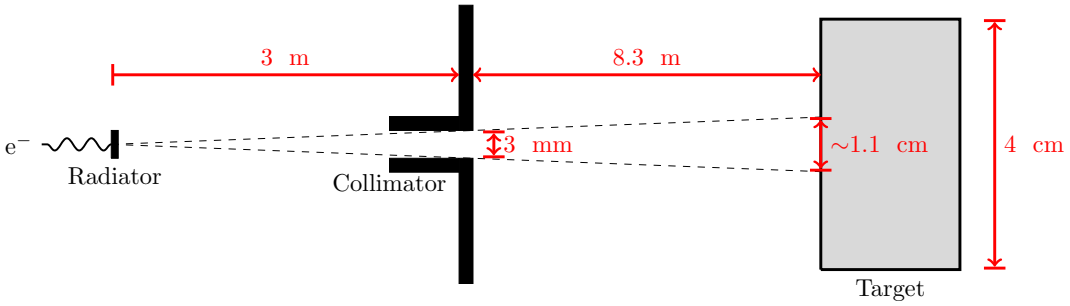

Figure 4.13: Dimensions involved in the collimation of the photon beam.

4.2.4 Liquid Hydrogen Target

The target for the experiment was a liquid hydrogen cell (LH_2) providing the reaction protons. A LH_2 target provides a clean, densely packed and stable source of protons with only negligible systematic errors in the initial momentum of the proton, arising from the molecular binding and ionisation energies.

The target cell, shown in figure 4.14 was made of from 125 μm thick Kapton, 4.8 cm in length and with a 2 cm radius. The target was positioned symmetrically around the beamline in the centre of the Crystal B detector, located 8.3 m down beam from the collimator.

Figure 4.14: Photo of the LH_2 target cell. Taken from reference [83].

The LH_2 target is pressurised to 1080 mBar at a temperature of 20 K providing a density of 4.25×10^{23} protons $\cdot$ cm^{-2}. The pressure and temperature of the target are constantly monitored and dynamically controlled in order to reduce systematic effects.

For part of the beamtime the target cell was evacuated so that data could also be taken in order to quantify the effects of background events from interactions with

the target cell during production runs.

4.2.5 Crystal Ball

The Crystal Ball (CB) provided the majority of the experiment's 4π acceptance covering the polar angles $20° < \theta < 160°$ [84, 85, 86] and full 2π azimuthal acceptance with the exception of a small region of 3.2 mm thick stainless steel along the horizontal plane where the two hemispheres of the ball are joined together. Figure 4.15 presents a photo and schematic of the Crystal Ball.

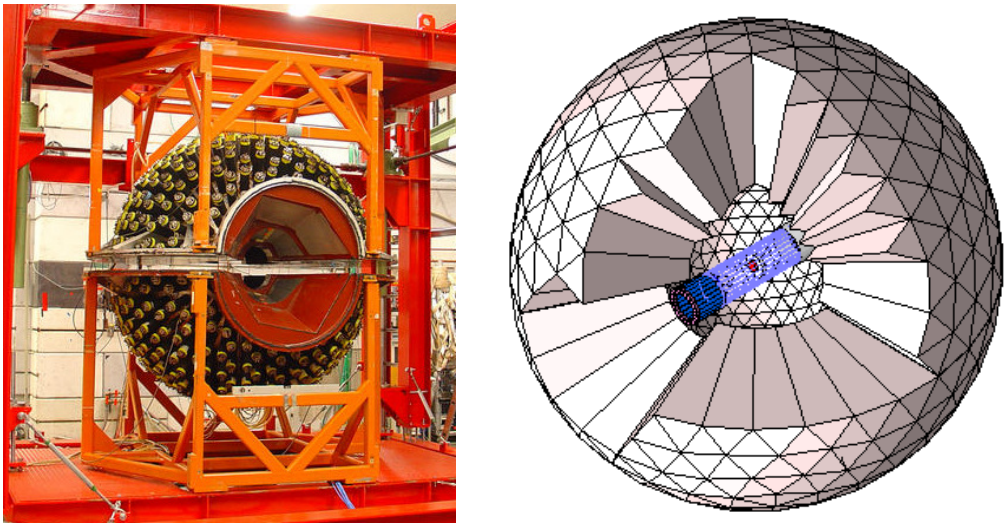

(a) CB Photo (b) CB Simulation

Figure 4.15: (Left) Picture of the Crystal Ball before installation into the A2 setup. (Right) Simulation of the Crystal Ball in Geant4. A number of crystals have been excluded from the figure to see the target (red) and PID (blue). Taken from reference [78].

The Crystal Ball is made up of 672 thallium doped sodium iodide NaI(Tl) crystals. It can be described as an icosahedron, each face of which is divided into four minor segments of 9 crystals. Each crystal is a truncated triangular pyramid, as shown in figure 4.16, which are tessellated together to form the ball. 48 crystals are removed from the full icosahedron leaving holes in both directions along the beam axis, reducing the angular acceptance. The forward angles were covered by the TAPS calorimeter, which is described in section 4.2.6.

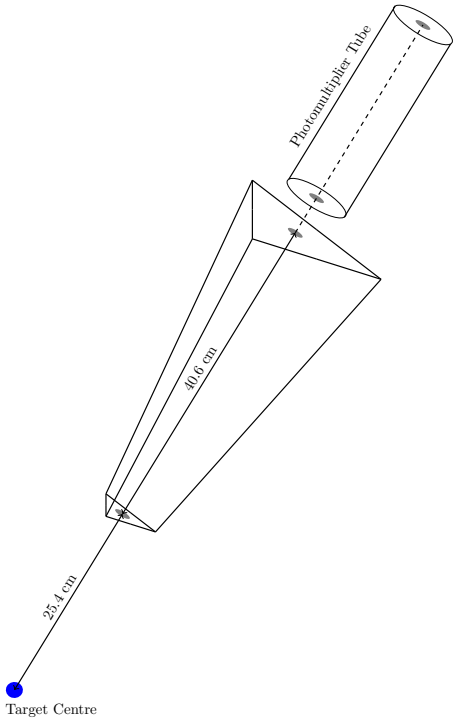

Figure 4.16: Individual NaI scintillator crystal, of which 672 make up the Crystal Ball detector.

Each NaI crystal acts as a calorimeter, measuring the energy particles deposit within it. As a charged particle moves through the scintillator, a stream of valence electrons in the crystal become excited and then decay back to their ground state, emitting photons of low energy. A small percentage of the photons are collected by a PMT which is attached to the crystal end by optical glue. Properties of NaI(Tl) crystals and how they are suited to calorimetry can be found in reference [87].

Neutral particles such as photons and neutrons must interact directly with a charged particle in the crystal before scintillation light is produced. The kinetic energy of a neutron is passed to a nucleus in a collision which passes through the material as a charged particle. A high energy photon mainly interacts with the scintillator via pair production of electron-positron pairs in the nuclear or electronic field. The pair can create a further shower of electromagnetic particles which create scintillation light as described previously.

Calibrations were performed on the crystals, as described in section 5.2.2, allowing a conversion of the signal output amplitude from the PMT to the absolute energy

deposited in the crystal by the particle. Due to the nature of the crystal and PMT, there is an inherent energy resolution of statistical origin associated with counting experiments.

Energy deposited from detected particles can be spread between a number of neighbouring crystals, this collection of crystals is described as a cluster. In order to reconstruct the original energy of a particle, the energy deposited in all crystals in the cluster needs to be summed. Further discussion of the reconstruction of clusters from CB signals can be found in section 5.2.2.

PID

The Particle Identification Detector (PID) was used to determine whether a particle exiting the target was charged. It sits in the gap between the target and the Crystal Ball and consists of 24 thin plastic scintillators, orientated azimuthally around the beam axis.

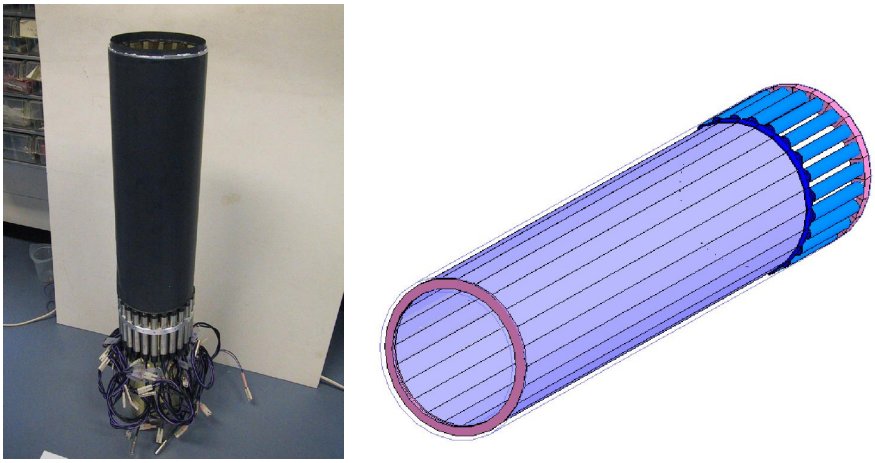

(a) PID Photo (b) PID Simulation

Figure 4.17: The Particle Identification Detector (PID). The plastic scintillators are wrapped in black tape. The PMTs and output electronics are seen at the bottom of the photo. Taken from references [78] and [88].

As a charged particle passes through the plastic, a small portion of its kinetic energy is converted to scintillation light. Furthermore the azimuthal position provided by the PID allows a signal to be matched to a subsequent cluster in the Crystal

ball. A neutral particle passing through the PID does so without producing an electromagnetic signal.

The relationship between the energy detected in the PID and the total energy of the particle deposited in the CB cluster can be used to classify the particle detected, figure 4.18 shows this relationship and is dubbed a *banana plot*. Making 2D cuts on the distribution allows us to distinguish between protons, electrons and charged pions.

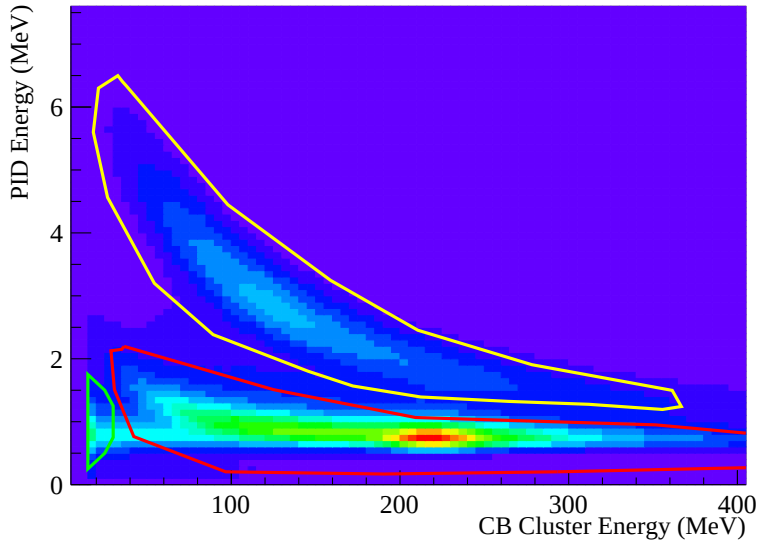

Figure 4.18: PID-Crystal Ball E-ΔE spectrum showing the energy from the PID against the energy deposited in the Crystal Ball. 2D cuts can be made to identify types of particle, here electrons (green), pions (red) and protons (yellow) can be distinguished. Taken from reference [83].

Due to the presence of the carbon recoil polarimeter during the experiment, the *banana plot* cannot be relied upon for identification of charged particles. The information provided by the PID was therefore not used in the analysis presented here. A larger proportion of background events will pass initial cuts without the use of the PID but these were subtracted in the analysis.

Recoil Polarimeter

The original experiment was run with a focus on measuring recoil polarisation observables. A carbon recoil polarimeter was placed between the PID and the crystal

ball. The polarimeter was designed to scatter protons recoiling from the reaction. The azimuthal distribution of the proton scattering angle was used to measure single meson polarisation observables O_x and T using a linear polarised photon beam and the C_x observable with a circularly polarised beam. Measurements of C_x made from this experiment have been published in reference [69].

The recoil polarimeter consisted of a tube orientated around the beam axis and an end plug, as shown in figure 4.19. The cylinder had an inner radius of 6.95 cm, an outer radius of 9.25 cm and was 20.75 cm long, positioned to cover the forward polar angles. The forward plug sat downstream, between the target and TAPS, it was a disk of radius 9.25 cm and 7.25 cm thick with a 2 cm radius hole in the middle for the beamline.

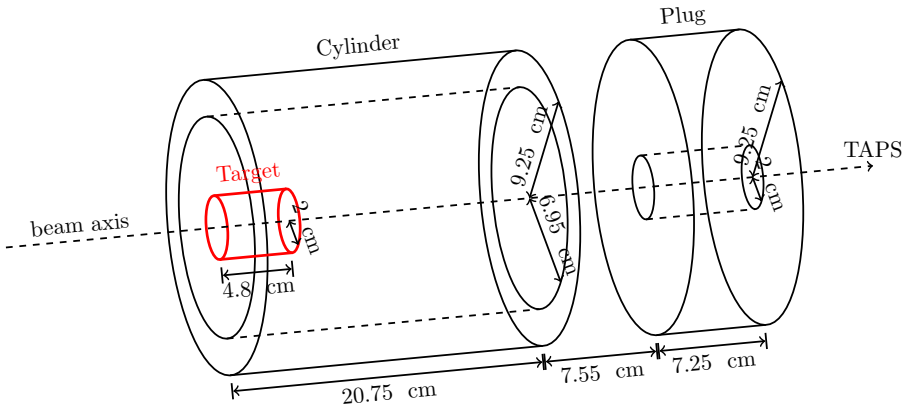

Figure 4.19: Schematic diagram of the carbon polarimeter around the target.

The recoil polarimeter was not used for the results obtained in this analysis, however its presence affected the acceptance of particles in the forward angles.

4.2.6 TAPS

TAPS (originally a Two Armed Photon Spectrometer, but now configured as a single wall) is shown in figure 4.20. The spectrometer is used to detect particles exiting the target in the range $0° < \theta < 20°$ from the target[89, 90, 91]. Due to the kinematics of a relativistic reaction, the centre of mass of a reaction is more forward boosted with increased tagged photon energy, meaning the 20° acceptance in the lab frame covers a much larger range of kinematics in the centre-of-mass frame.

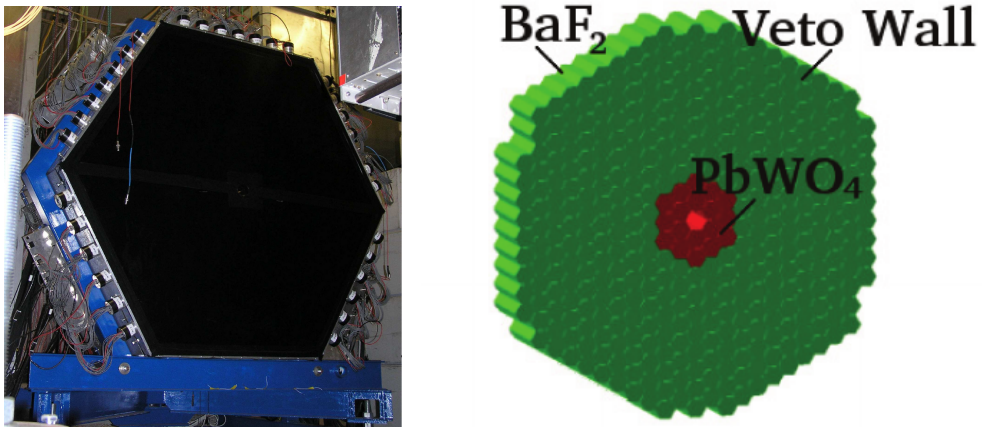

(a) TAPS Photo (b) TAPS Simulation

Figure 4.20: Photo of the TAPS array as set up in the A2 Hall. Photo taken from [83], simulation image taken from [92].

TAPS was built from an array of 384 tessellated hexagonal BaF_2 crystals (figure 4.21) providing polar and azimuthal acceptance for the most forward boosted particles. Each crystal is a regular hexagonal prism 25 cm in length with the last 2.5 cm machined into a cylinder for connection to the PMT.

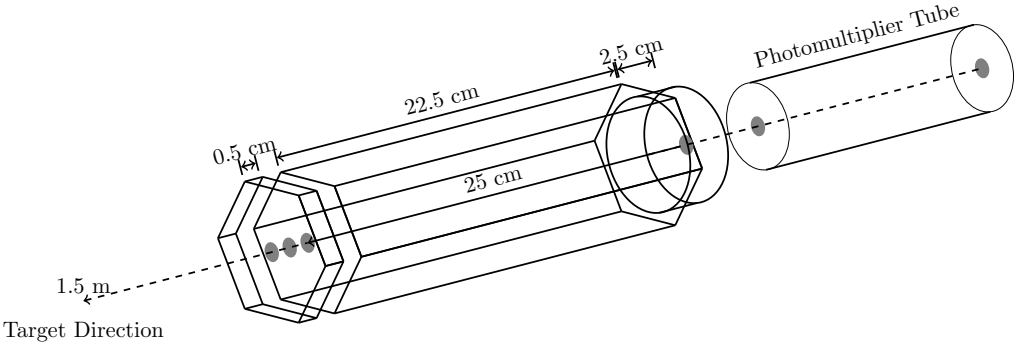

Figure 4.21: Individual BaF_2 scintillator crystal 384 of which make up TAPS. A 5 mm plastic scintillator cap (VETO) sits between the target and BaF_2 crystal providing particle charge information.

Unlike the CB, TAPS is far enough removed from the target that it can be used for particle ID based on its time-of-flight. BaF_2 crystals scintillate light with both fast and slow components with respective decay times of 0.6 ns for scintillation wavelength of 220 nm, and 620 ns for scintillation wavelength of 300 nm. Neutrons detected in TAPS will have a time delayed from that of photons. Charged particle IDs are distinguished with E-ΔE information, provided for TAPS by its VETO

detector.

VETO

Capping each crystal of TAPS on the target side is 5 mm thick plastic scintillator VETO. The VETO records scintillation energy deposited in it which is passed along wavelength shifting fibres, transporting the signal outside the TAPS plane to a PMT. Similarly to the PID for the crystal ball, TAPS can be used to distinguish between charged particles by providing E-ΔE information.

4.2.7 Trigger

The standard trigger is based on a logical combination of ORs of signals from elements of the different detector systems (E.g. PID, CB, TAPS, TAPS VETO), together with a specified number of Clusters in the CB/TAPS, and the so-called Energy Sum (ESum). The energy sum is a logic signal derived from a programmable discriminator whose input is the analogue sum of all the elements in the CB. The trigger conditions for this experiment were chosen based on the physics requirements, a summary of the conditions used is shown in table 4.3. The motivation behind the trigger is explained further, below.

Run Period	September - October 2008
Beam Energy	1508 MeV
Collimator	3 mm
Minimum Energy Sum	150 or 300 MeV
Cluster Multiplicity	M3 and M2/4
Event Rate	900 Hz
Events Recorded	750×10^6
Total Data	720 GB

Table 4.3: Experimental running conditions.

The ESum was initially required to exceed 150 MeV and this value was later increased to 300 MeV. The limit removed events with only low energy signals which were background events, impossible to produce with the kinematics of the π^0p final state reaction with the centre-of-mass energy under investigation. The change in the

ESum was made about half way through the beamtime in order to decrease the deadtime of the DAQ while also increasing the portion of recorded events corresponding to the coherent peak. The change had the indirect advantage for this analysis of increasing the percentage of recorded events coming from $2\pi^0$ decays. The two data sets were analysed together after checks were made on their compatibility.

The cluster multiplicity from CB and TAPS was set to have a lower limit of three which accounted for decay products of π^0 photoproduction off the proton; the two decay photons from a π^0 and the recoiling proton. Every fourth event detected which consisted of two clusters was also accepted, so that events where one of the decay particles was not detected could be quantified. The clustering method used by the DAQ is not as involved as that used in later analysis in order that the number of clusters can be determined quickly.

If the logic conditions were not met, the DAQ was reset, dumping the stored signals and preparing for the next event.

4.3 A2 Simulation

Simulation of detector systems and the underlying physics becomes more important as the complexity of experiments increases. A Monte Carlo simulation of the A2 setup [93] has been developed using Geant4 libraries [94, 95]. The simulation is designed to directly match the geometry of the experimental setup with physics libraries which best describe the scintillation showers and other detected signals.

The main components of the A2 simulation are the CB and TAPS, shown respectively in figures 4.15(b) and 4.20(b). Models of the other detectors are also included and the setup allows any additional detectors to be added to the setup.

The simulation is fed events with the decay particles from a particular reaction channel. Signals produced in the simulated detectors are recorded in the same way as real experimental data.

In this analysis the simulation has been used to produce events from the various

reaction channels expected to contribute to the signal and background. The shape of the missing mass from each channel has been used as a Probability Density Function (PDF) to fit the experimental missing mass distribution, the implementation of this is discussed in 6.4.2, showing the simulated distributions in figures 6.14 and 6.15.

Chapter 5

Calibration

All of the detector systems were calibrated carefully before the recorded data were used to extract meaningful and accurate measurements. As each research group specialised in different detectors, the calibration work was shared amongst the collaboration for each experimental run. The complexity of the calibration varied from detector to detector with some cross reliance between detectors.

For this experimental run most of the calibration has been carried out by others, a summary of the process for a selection of detectors is given in this chapter. A more detailed discussion has been included on the calibration and determination of the degree of linear polarisation; work carried out by myself.

Producing accurate, reliable calibration of the detectors is of great importance in producing physical results with minimal systematic uncertainties.

5.1 Timing Calibration

Modern hadron physics experiments require timing precision of the order of 10^{-9} s to separate potentially overlapping reactions. Detector elements and electronics on this scale have inherent timing resolution and delays which differ between elements of identical design. Signals from an event registering in multiple detector elements will reach the DAQ system at different times. In order to account for these effects

a number of complementary approaches were applied to align the time of signals within and between detectors.

A preliminary calibration was achieved in the hardware by testing detector electronics in order to quantify timing profiles for each component. Signals were brought into alignment to arrive at time to digital converters (TDCs) within a narrow time window by adjusting cable lengths.

Fine timing calibration was achieved offline after the experimental run. Peaks in coincidence times relating to triggered events were identified for each detector element and aligned with each other. The timing alignment of the tagger is presented as an example in figure 5.1.

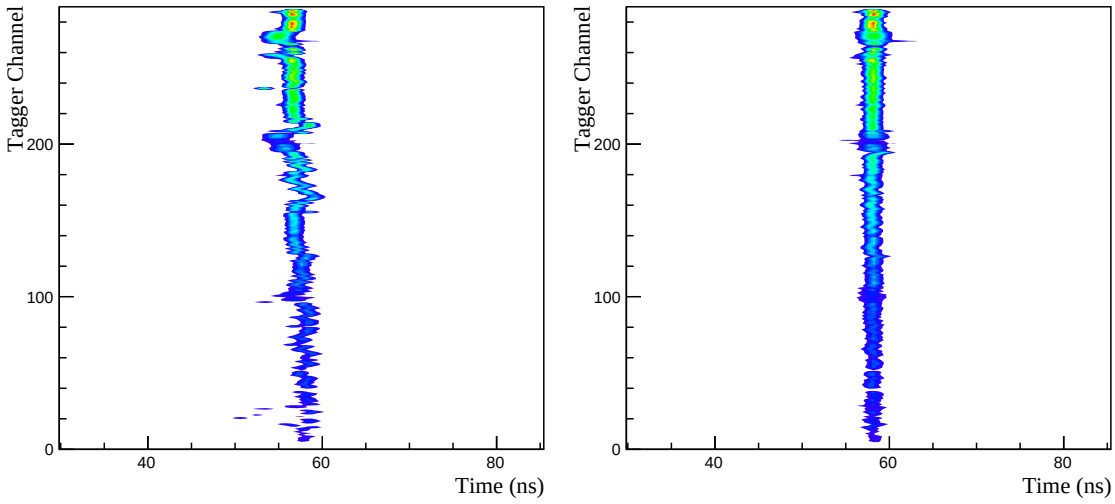

Figure 5.1: Coincidence peaks of every tagger channel were aligned to the same arbitrary time. Left - Before alignment. Right - After alignment.

Timing calibration only aligns peaks from detectors and detector elements to the same value relative to the initial trigger. The relative time between signals detected in, for example, TAPS and the CB, was more difficult to determine but is not necessary for this analysis, as very loose timing cuts ∼100 ns were applied.

It was possible to use TAPS for time-of-flight particle identification as its position is far enough down stream from the target. Signals from TAPS arrived with multiple timing peaks each associated with different particles, the earliest peak was the photon peak, which was used for the alignment of the detector elements.

5.1.1 CB Time Walk Correction

The calibration of coincidence time from a peak of all the recorded signals in a detector is not necessarily the whole picture. The response time of a detector relates to how quickly a signal passes the trigger threshold energy, detected particles of lower energy have a longer response time, this is called a *time walk*. If the time walk is not accounted for, the timing coincidence peak is widened, increasing the uncertainty in the energies detected through identification of the tagger prompt photon. The time walk calibration is made by examining the relationship between the energy and recorded time of highest energy cluster detected in the CB (Figure 5.2).

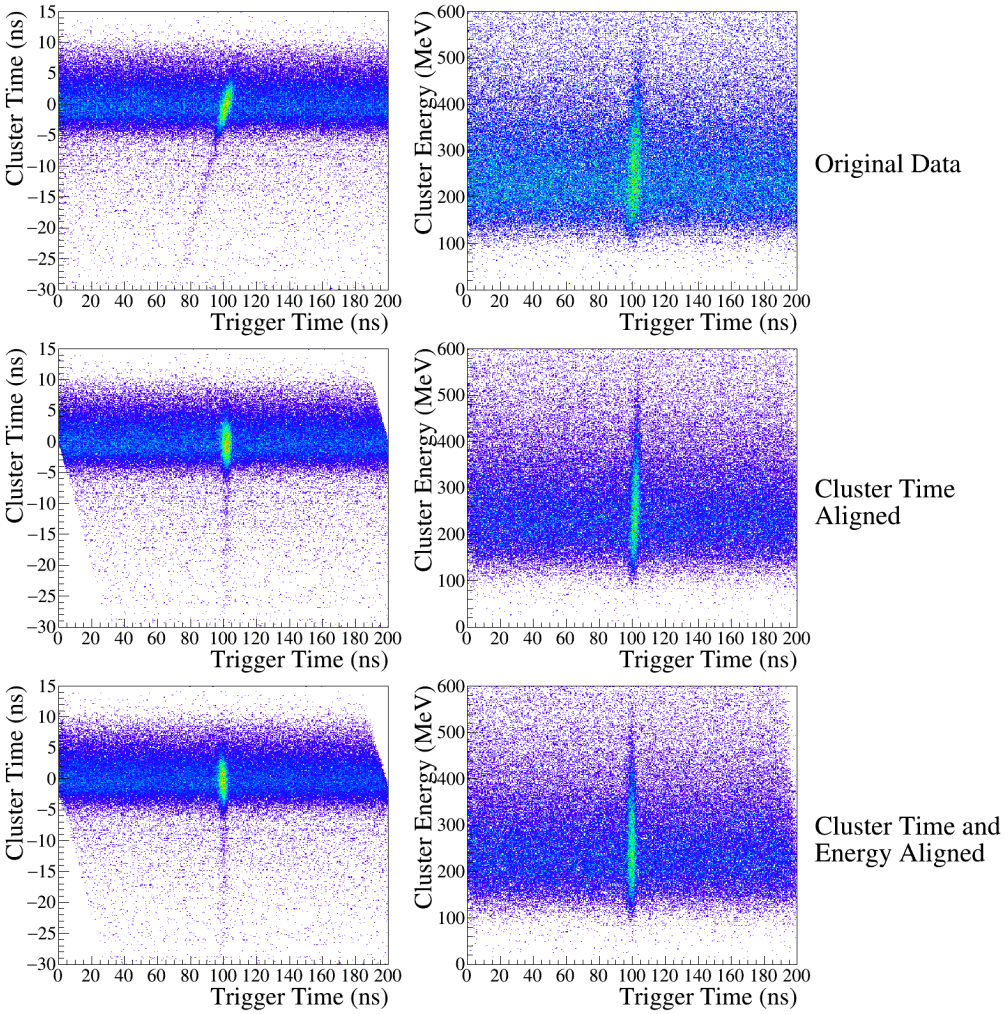

Figure 5.2: Effects of cluster time walk corrections. Left - Trigger time against highest CB energy cluster time. Right - Trigger time against CB Cluster energy.

By conducting a least squares fit to the peaks in the CB-energy and CB-time distributions the corrected time (T_{corr}) was determined to be given by:

$$T_{corr} = T_{tagg} - T_{clu} - 0.0077 E_{clu} \times T_{tagg}, \tag{5.1}$$

where E_{clu} is the cluster energy, T_{clu} is the cluster time and T_{tagg} is the arbitrary alignment time. The effects of the time walk calibration are shown in figure 5.3; the tagger timing resolution is doubled from a width of 3 ns to 1.5 ns.

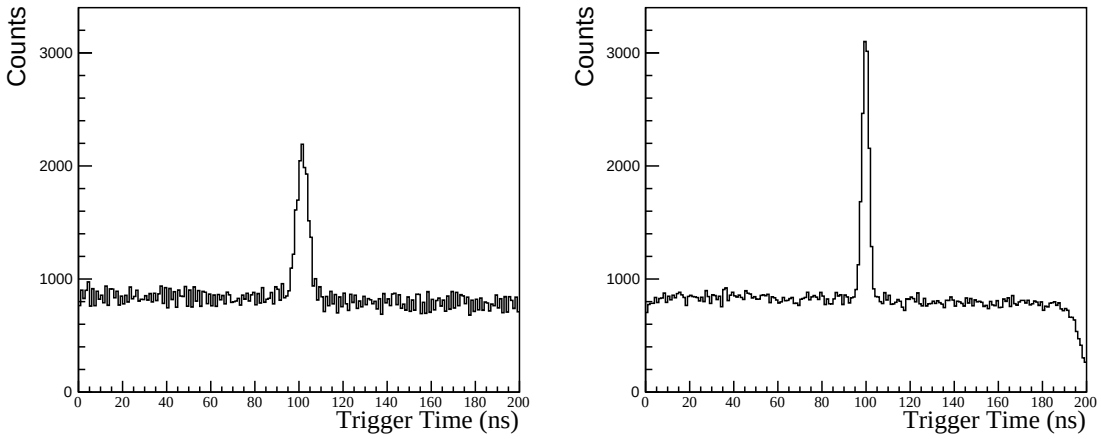

Figure 5.3: Results of the time walk corrections. Left - Before time walk corrections (FWHM = 6 ns). Right - After time walk corrections (FWHM = 3 ns).

The coincidence time walk calibration corrected for the effect of the time walk on the trigger time and therefore the tagger time. The resulting sharper coincidence peak reduced the uncertainty in the identification of the correct tagged photon.

5.2 Energy Calibrations

The energy calibration of detectors is more complex than the alignment of timing signals. The detectors use different methods of measuring energy, the tagger infers energy from the bend of an e^- in a magnetic field, while the CB and TAPS are calorimeters, relying on PMTs to count scintillation photons from their crystals.

5.2.1 Tagger

The tagger is one of the simpler detectors to calibrate for a beam time, the channels are independent, relying only on a coincidence from neighbouring scintillators to produce a digital signal.

The tagger calibration was dependent on the electron beam energy and tagger magnetic field strength, where the electron beam energy was measured by MAMI.

During calibration no radiator is used so that all electrons detected on the focal plane are of the beam energy. The field strength of the tagger magnet is tuned to direct the beam at the beamdump, this is directly measured in one location using an Nuclear Magnetic Resonance (NMR) probe. For this experiment the NMR value was 1.8319 T and the beam energy 1508 MeV.

In order to calibrate the energy of the tagger channel, seven different beam energies were used between 195.3 and 1307.8 MeV, at a low current. For each beam energy the NMR was adjusted, scanning the electron beam through a number of tagger channels. The field strengths at which the electron beam was aimed at the small triple overlap region between three scintillators were used to precisely determine the fractional channel which relates to the energy with the NMR set for production runs. The relationship between the seven different beam energies and the fractional tagger channel were fitted, assuming a uniform field strength, producing a relationship from which energies for tagger channels were extrapolated.

The scan was conducted once for each running beam energy. Small changes to the NMR from those used in the initial calibration are accounted by extrapolating values using the calibration program *ugcal* with an estimated uncertainty in the tagged photon energy of ± 0.5 MeV[79].

5.2.2 Crystal Ball and TAPS

For calorimeters, the energy of a particle detected is not described by the location of the detector. Instead it is determined by the magnitude of signals output from the

PMTs. A detected particle in the CB or TAPS can cause scintillation in a number of crystals, forming a cluster; the energy deposited in all of the crystals in a cluster is summed together to reconstruct the energy of the particle.

Each crystal and attached PMT express different inherent properties which were accounted for by the energy calibration.

There are two steps to the energy calibration of the CB and TAPS calorimeters. A low energy calibration is conducted before the experimental run using a radiation source with a known, low energy peak. The high energy calibration consists of an offline analysis of energies in crystals from events identified as the decay of $\pi^0 \rightarrow \gamma\gamma$.

Low Energy Calibration

The low energy response of the Crystal Ball is calibrated using 4.438 MeV photons from a mixed ^{241}Am/^{9}Be source placed in its centre. The decay chain resulting in the 4.438 MeV γ is as follows:

$$^{241}_{95}Am \rightarrow ^{237}_{93} Np + \alpha \tag{5.2}$$

the α from Americium decay is absorbed by Beryllium

$$^{9}_{4}Be + \alpha \rightarrow ^{13}_{6} C^* \tag{5.3}$$

the $^{13}_{6}C^*$ emits a neutron

$$^{13}_{6}C^* \rightarrow ^{12}_{6} C^* + n \tag{5.4}$$

the excited $^{12}_{6}C$ decays into the $^{12}_{6}C$ ground state by γ emission.

$$^{12}_{6}C^* \rightarrow ^{12}_{6} C + \gamma \ \text{(4.438 MeV)} \tag{5.5}$$

A charge to digital converter (QDC) relates the magnitude ot the analogue signal from the PMT into a digital channel for further processing. The QDC spectrum and alignment from the calibration decay is shown in figure 5.4.

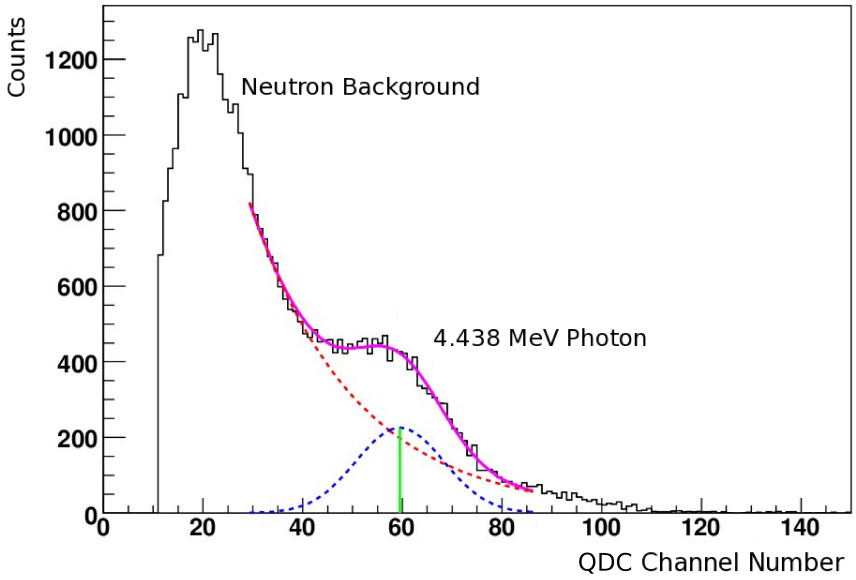

Figure 5.4: CB QDC spectrum from $^{241}Am/^{9}Be$ source. 4.438 MeV γ peak is used to align channels. Taken from reference [83].

The 4.438 MeV decay photon is of sufficiently low energy to generate a scintillation shower in only a single NaI crystal, allowing each detector element to be adjusted independently. The high voltage of each PMT was tuned to adjust the gain until each crystal has its peak aligned on the same QDC channel.

A similar calibration is performed with TAPS using cosmic muons which have a minimising ionisation peak at 37.7 MeV which relates to the average path length the muon takes through any TAPS crystal. Figure 5.5 shows the alignment of the TAPS QDC to the muon peak.

High Energy Calibration

The energy of decay photons expected in experiments are up to two orders of magnitude higher than those used in the low energy calibrations. Calibration using the QDC high voltages was no longer sufficient and so more sensitive calibrations of the main calorimeter systems were carried out. These calibrations were conducted

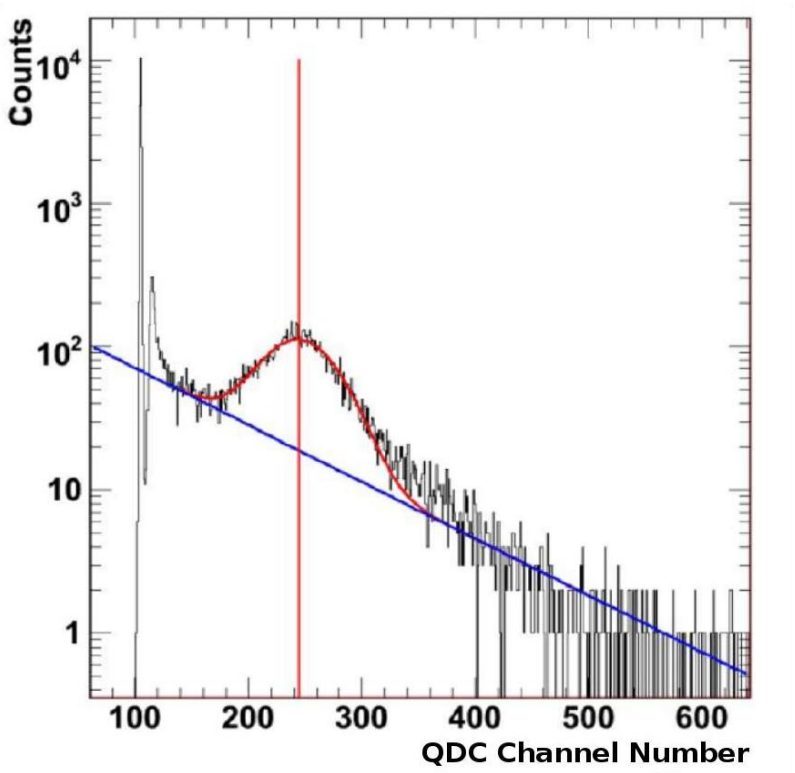

Figure 5.5: TAPS QDC spectrum from cosmic muons. The 37.7 MeV peak is used to align channels. Taken from reference [96].

offline, on the experimental production data after it was recorded, by utilising the invariant mass constraint of photons produced in the $\pi^0 \to \gamma\gamma$ decay from $\gamma p \to \pi^0 p$ reactions.

By reconstructing a particle from two decay photons, a 4-vector with a mass peak at the π^0 invariant mass is expected. A limited selection of events are used in the calibration as laid out in table 5.1.

The detection of both π^0 decay photons fully describes the kinematics of the reaction; meaning the energy of the two photons is directly related to the pair of crystals in

Tagged photon energy < 180 MeV	Eliminates potential background channels and increases the polar distribution of the decay photons.
> 70% cluster energy in central crystal	Reduces calibration dependence on surrounding crystals reducing iterations required for convergence.
$M_{\gamma\gamma} = M_{\pi^0} \pm 30$ MeV	Reduces the total number of events for processing.

Table 5.1: Event cuts for calorimeter high energy calibration.

Crystal Ball	$0.017/{E_\gamma}^{0.4}$ (GeV)
TAPS	$0.037/{E_\gamma}^{0.25}$ (GeV)

Table 5.2: Resolution of the Crystal Ball and TAPS as a function of detected photon energy.

which they are detected. For each crystal a histogram of $M_{\gamma\gamma}$ is formed, filled with events where the crystal is central to one of the detected γs. The events filling the distribution are therefore integrated over the phase space of the second γ. A gain correction g is applied to each crystal such that,

$$g = \frac{M_{\pi^0}}{\langle M_{\gamma\gamma} \rangle}. \tag{5.6}$$

The precise gain calibration of each crystal is dependent on both the calibration of other crystals in the particle cluster and the calibration of the crystal in which the second γ is detected. The cross dependence the calibration requires the procedure to be run multiple times until the gain values for all crystals converge and the 4-Vector peak sits on the π^0 mass.

The CB gain calibration is carried out independently before being utilised in the TAPS calibration. Using only tagged photons less than 180 MeV, the probability of finding both γs in TAPS is small so the calibration of TAPS crystal gains is conducted using events with one γ cluster in the CB and the second γ cluster in TAPS.

Table 5.2 shows the resolution of the CB and TAPS after calibrations as a function of energy.

5.2.3 Clustering

Clusters are formed by identifying groups of neighbouring crystals all with energy deposited in them. Figure 5.6 shows what the distribution of energies in a large CB and TAPS cluster may look like.

Several algorithms are available for use in determining what constitutes a cluster,

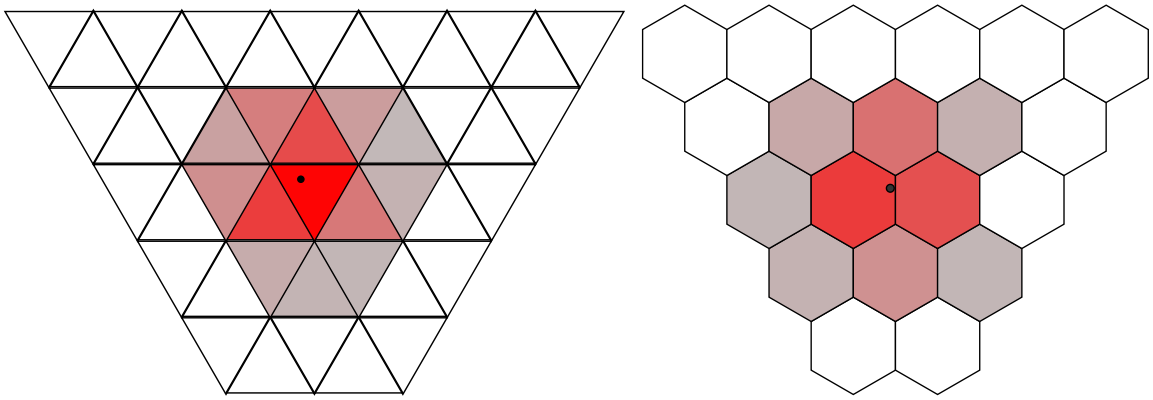

(a) CB Cluster (b) TAPS Cluster

Figure 5.6: Diagram of a particle clusters in CB and TAPS. The black dot is the particle vertex and the triangles/hexagons show individual crystals. The expected energy deposited in a crystal is shown as an intensity of red.

based on the intended analysis. The central position of a particle hit can be identified by using the mean energy weighted distribution of crystals in a cluster.

On occasion a cluster will contain a separated crystal that is not captured by the main clustering algorithm and forms a split off cluster. The energy detected in the split off cluster is necessary for accurate reconstruction of the initial particle energy. Split off clusters are accounted for by checking if any of the reconstructed clusters are within a pre-defined distance to neighbouring cluster crystals. If they are within this distance then the clusters are attributed to the same reconstructed particle.

Parameters used in determining clusters in this work were selected to maximise the number of events with 3 clusters are given by:

Max CB Clusters	15
Min CB Cluster Energy	12 MeV
Max TAPS Clusters	8
Min TAPS Cluster Energy	20 MeV
Split Off Max Separation	3

Table 5.3: Parameters chosen for cluster identification. The maximum number of reconstructed clusters allowed in both detectors is described before merging the split off clusters.

Once the energy and position of a cluster was determined, a photon 4-vector was

reconstructed. Its direction is given by the vector from the centre of the target to the cluster position and the measured energy as the photon momentum and energy.

5.3 Photon Beam Linear Polarisation

The calculation of the polarisation observables measured in this work are all dependent on the degree of linear polarisation. In order to minimise the systematic uncertainty, a precise method of measurement is needed. This section discusses the physical origin of the polarisation (section 5.3.1), how the diamond is aligned to access a high degree of polarisation at the desired photon energies (section 5.3.2) and finally how the degree of polarisation is calculated from the coherent bremsstrahlung enhancement (section 5.3.3).

5.3.1 Polarisation Origin

The coherent bremsstrahlung process produces a range of photon energies. The degree of polarisation across the energy range is dependent on the orientation of the diamond crystal planes with relation to the electron beam. A thorough explanation of the link between the beam energy, lattice orientation and polarisation is covered by Timm in reference [97].

Diamond is chosen as the crystalline radiator due to the combination of its high Debye temperature (2250 K [98]) and small lattice constant (3.567 Å). A high Debye temperature implies the material's atomic structure is highly rigid providing well defined lattice planes which in turn produce a sharper coherent spectrum.

A smaller lattice constant allows a higher range of angles between the beam and lattice plane for the production of coherent bremsstrahlung peaks in a useful range. Other materials have smaller lattice constants, however none of these match the diamond's unique Debye temperature. This combination of material properties make diamond the most suitable crystal for coherent bremsstrahlung production.

The $[0, 2, 2]$ and $[0, 2, \bar{2}]$ crystal planes of the diamond are used to produce the coherent bremsstrahlung. These planes produce the strongest enhancement as they have the highest density within the material and can be isolated from contributions from other higher order terms.

The production of bremsstrahlung from this scattering is observed with a linear polarisation perpendicular to the lattice plane.

5.3.2 Diamond Alignment

To achieve the desired clean polarisation spectrum, the relationship between the orientation of the lattice planes and coordinate system inherent to the goniometer have to be determined. Once the relationship has been determined the goniometer can now orientate the diamond so that the electron beam and lattice planes are aligned to generate the desired polarisation spectrum.

A procedural method called the stonehenge technique is used to align the diamond. Developed by Livingston[99] this procedure has built on a technique laid out by Lohman *et al.*[75]. Previous methods of precise alignment required a degree of careful mounting and pre-alignment of the diamond to less than 1° using a laser. The stonehenge calibration is performed in beam using tagger hits with no additional equipment required and has proven successful in quickly locating a calibrated set of angles for coherent bremsstrahlung production. The technique has been used in the A2 experimental setup as well as at other labs including CB-ELSA in Bonn, MAXLab in Lund, CLAS and GlueX at Jefferson Laboratory.

The stonehenge technique involves conducting a series of scans, sweeping the goniometer around a cone. With each iteration, the centre of the cone is moved until the desired accuracy is attained. Figure 5.7 shows scans before and after calibration where the coherent enhancement spectrum is displayed radially with the angle relating to the location on the cone.

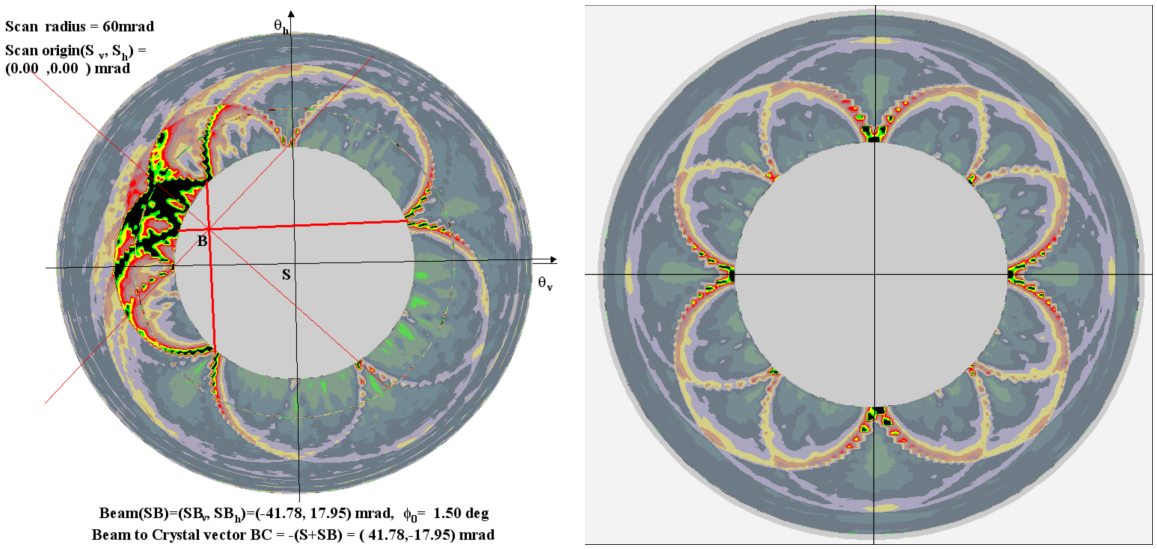

(a) Stonehenge Scan (b) Stonehenge Aligned

Figure 5.7: Shown radially as colour intensity is the coherent enhancement, the polar angle relates to the angle around the cone. Left - Initial stonehenge scan of the diamond. Right - Fully aligned diamond stonehenge plot with polarisation planes at ±45. Images taken from reference [99].

5.3.3 Degree of Polarisation Calculation

Once the diamond was aligned to generate polarised photons of particular energy, it was necessary to determine the degree to which the photons were polarised. This was achieved through measuring the enhancement across the tagged photon range and fitting this with a phenomenological function from which the polarisation could be extracted.

Figure 5.8 shows the photon energies of the tagger hit spectra for amorphous and coherent radiators, where the coherent spectrum shows an enhancement at certain energies over the amorphous spectrum.

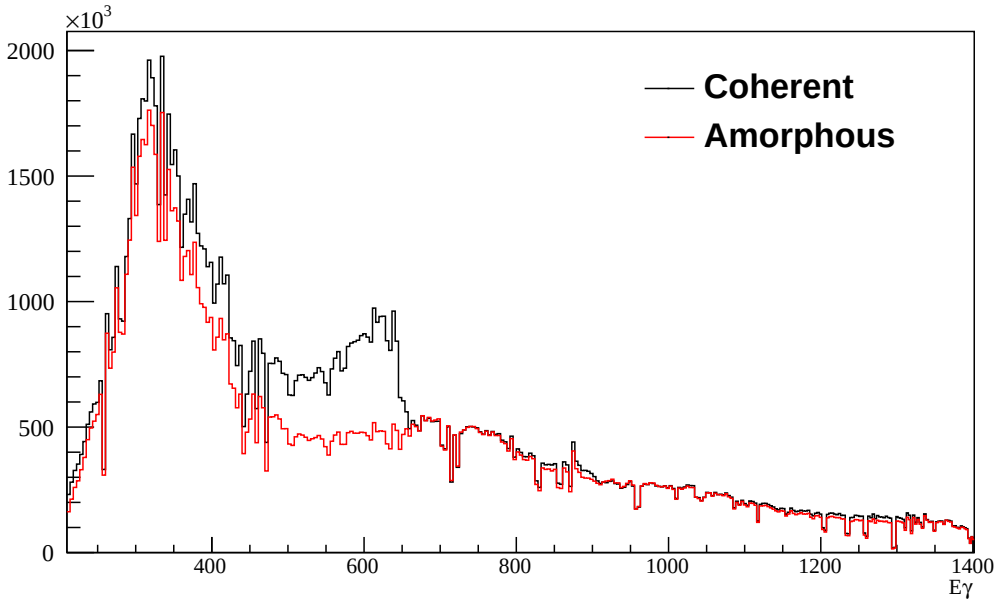

Figure 5.8: Spectrum of tagged photons responsible for a triggered reaction in the CB. Diamond (coherent) and Copper (amorphous) spectra are shown showing the enhancement arising from the polarisation from crystal planes. The figure represents a convolution of the Bremsstrahlung spectrum and photoproduction reaction cross section of events taken from production data.

The enhancement between the two spectra is then taken as the ratio of counts in the coherent to normalised amorphous data,

$$Enh\left(E_\gamma\right) = \frac{\mathrm{N_{coh}}\left(E_\gamma\right)}{\mathrm{N_{amo}}\left(E_\gamma\right)}. \tag{5.7}$$

To generate an enhancement, a tagger spectrum from an amorphous radiator was assumed to take the same form as that of the incoherent portion of the coherent spectrum. The amorphous spectrum was normalised to the coherent spectrum by choosing a region with no enhancement and scaling by the ratio of the counts in the spectra at that point. Often this is taken just above the first enhancement peak.

In the case of the Mainz experiment the collimation of the photon beam was not narrow enough to completely suppress the enhancement between the first and second peaks. An estimation of the enhancement was made in this region choosing the minimum χ^2 produced by the phenomenological fit to the enhancements made with

a range of baselines (see figure 5.10). For this experiment the enhancement in the normalisation region value was measured as 1.06, as shown in figure 5.9.

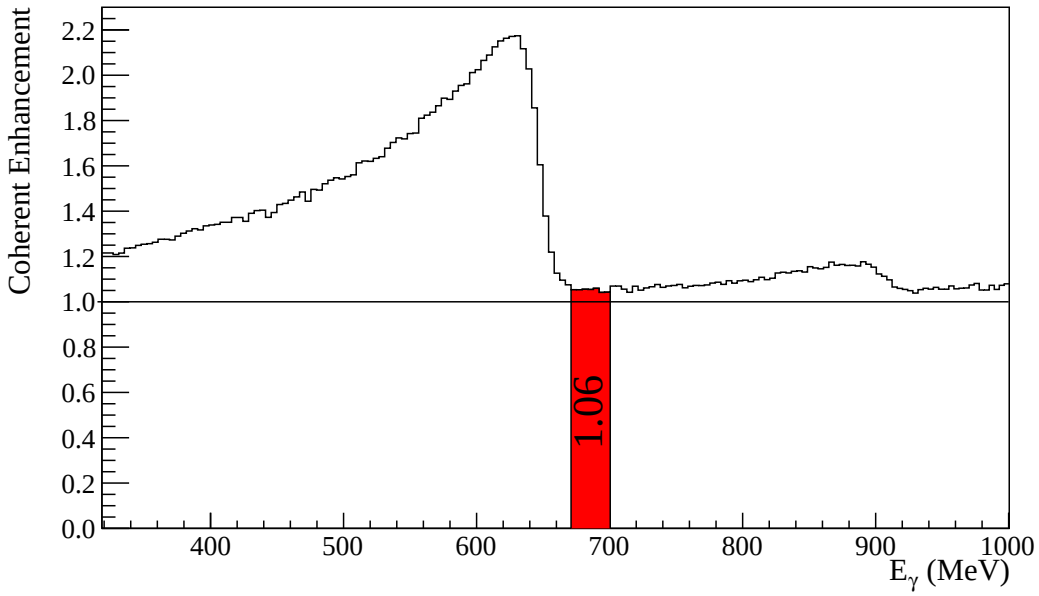

Figure 5.9: Coherent enhancement of the polarised coherent contribution of the Bremsstrahlung spectrum over the incoherent portion as measured with copper. The range used for an average baseline normalisation is filled red.

The phenomenological function that describes the enhancement spectrum from all contributing lattice planes is expected to be exceedingly complex[100]. Instead of considering all of the contributing components, the strongest contributors were aligned to produce an enhancement in a particular energy range. This allows only the 022 and 044 vectors to be considered with negligible contribution from other planes. The fit to the enhancement spectrum along with the fit parameters is shown in figure 5.10.

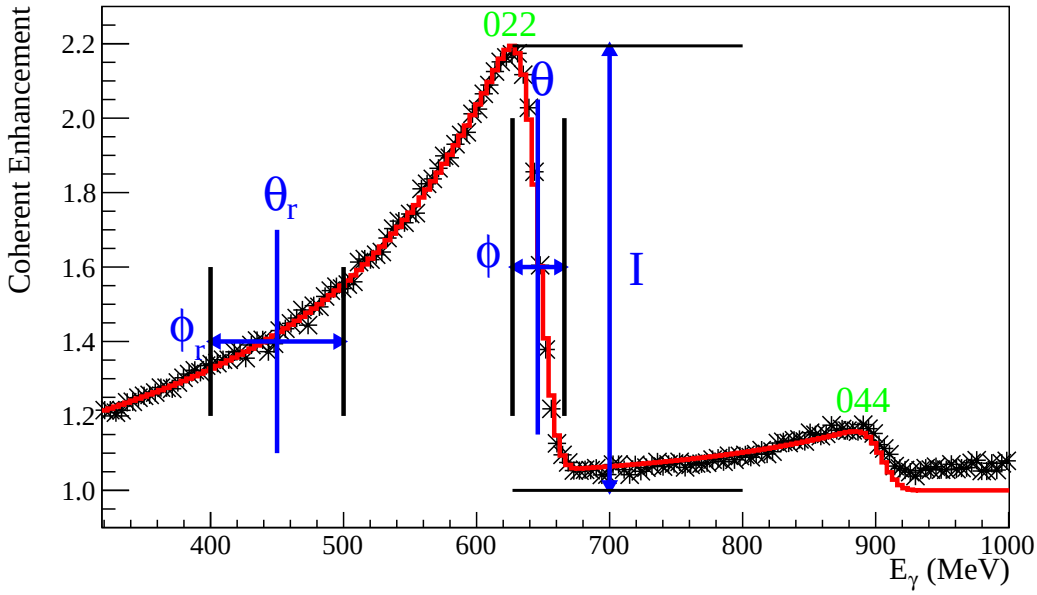

Figure 5.10: Enhancement of the polarised coherent contribution of the Bremsstrahlung spectrum over the incoherent portion measured with copper. Enhancement data (black) are overlaid with a fit (red)[101]. The free parameters in the fit for the 022 vector are shown in blue.

The function used to fit the enhancement from reference [101] has five free parameters for each lattice vector fitted, as shown in figure 5.10. The free parameters relate to the spectrum as follows; I is the maximum enhancement, θ is taken as the position at a half drop in the edge relating to the angle the beam makes with the lattice, ϕ is the spread from the peak to θ, θ_r relates to the opening angle of collimation and ϕ_r is the spread in this angle. All of the fit parameters shown in the figure have a independent duplicates for the 044 peak which has also been fitted.

The lowest energy portion of the enhancement has been excluded from the fit as there are complicated coherent effects which are not taken into account by the fit function, reference [102] discusses the related complications.

The degree of polarisation as a function of beam energy was constructed from the same parameters used to fit the enhancement. The resulting polarisation spectrum is shown in figure 5.11.

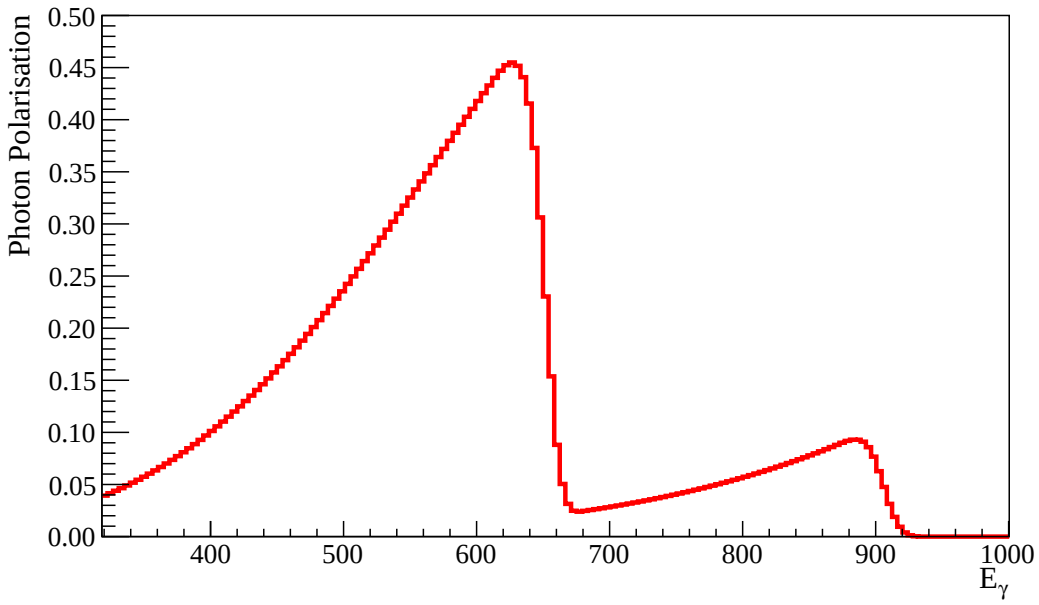

Figure 5.11: Degree of the photon polarisation over the coherent peak range.

5.3.4 Polarisation Correction

The standard procedure outlined above is usually conducted on data taken during tagging efficiency experimental runs. Tagging efficiency runs are carried out with low beam currents, triggering on signals in a Pb-glass block placed in the beam line. A failure in a RAID array of hard disks means none of the tagging efficiency runs are available so the enhancement fit was made using data from the production runs.

When calculating the degree of polarisation using production runs, the polarisation was consistently in the order of 30% lower than expected across the whole energy range. This discrepancy was measured by comparing values of single π^0 photon polarisation observable Σ against SAID and Bonn-Gatchina PWA predictions in the $\Delta(1232)$ resonance region, where the predictions were in alignment, as shown in figure 5.12. Figure 5.13 demonstrates the region of agreement between the theories and the discrepancy with the enhancement fit.

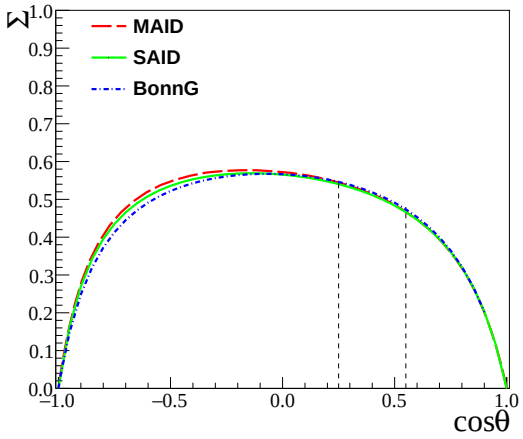

Figure 5.12: Predictions of the polarisation observable Σ from the MAID, SAID and BnGa PWA fits as a function of $\cos\theta$ at centre of mass energy W = 1232 MeV. The area between the two dashed lines is the region $0.25<\cos\theta<0.55$ which was used to normalise the degree of polarisation.

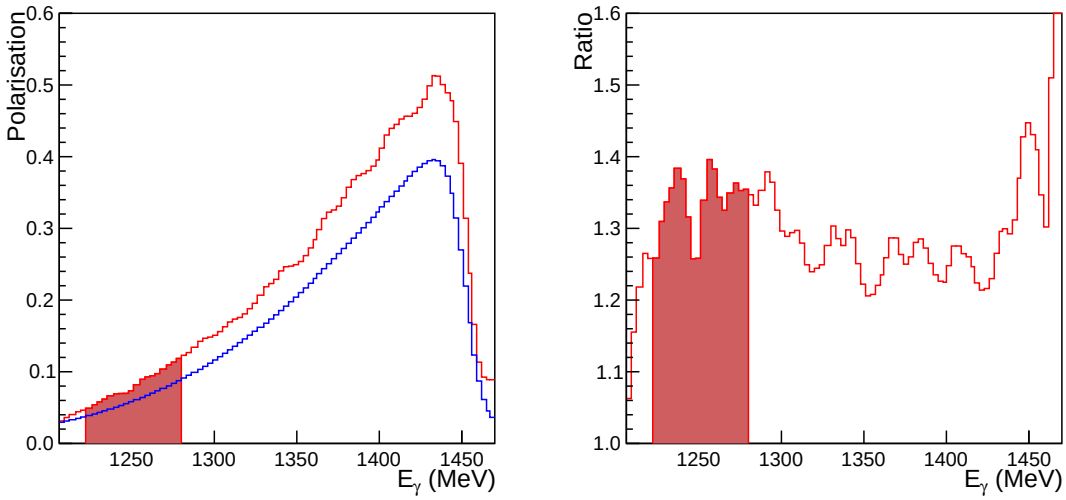

Figure 5.13: Left - Degree of the photon polarisation over the coherent peak range. Blue - From the enhancement fit. Red - Obtained by comparison with PWA fits to world data (red). Right - Ratio of calculated polarisation to that obtained from the PWA fit. The region highlighted is the Δ(1232) resonance range used to normalise the polarisation.

The origin of the discrepancy between measurements using a tagging efficiency trigger and a production trigger has been investigated. The low beam current of 8 pA used in tagging efficiency runs removes all random events in the tagger coincidence peak, also reducing the probability of multiple hits in a tagger channel within the open timing window. The beam current used with the diamond radiator was 36 nA

while for the amorphous copper radiator it was 10 nA. However the total number of bremsstrahlung photons created was of the same order. The effect came in the coherent peak range where the relative flux for the diamond was higher, meaning a larger percentage of the photons in this region were missed as a second or third hit. Including the additional photons only accounted for half of the observed difference and so a different approach was required.

In order to quantify this discrepancy, the values of the single π^0 polarisation observable Σ were utilised. Measured values for $P\Sigma$ were compared to those from PWA predictions where the value in the Δ peak has been well constrained and is consistent between the three PWA predictions (MAID, SAID and BG). The ratio $\frac{\Sigma_{observed}}{\Sigma_{expected}}$ =1.31(3) was used as a scaling factor for the polarisation. The statistical error in this scaling factor was translated into a systematic error in all values, dependent on the final degree of polarisation of 2%. Combined with an estimated additional 2% uncertainty arising from the PWA predictions[103], the total systematic uncertainty related to the polarisation is calculated as 3%.

Final values used for the polarisation for the data taken in the two polarisation planes are shown in 5.14.

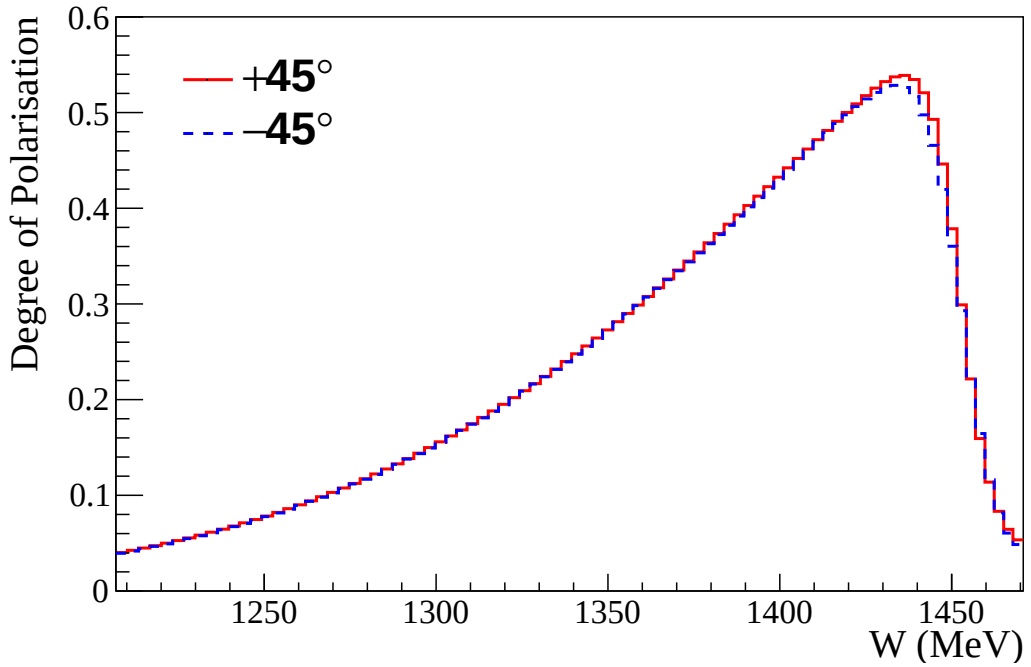

Figure 5.14: Final degree of photon polarisation over the coherent peak after scaling.

Rigorous calibrations were carried out on all the detector systems in order to minimise any associated systematic uncertainties in the final measurements. The diamond radiator was aligned to maximise the degree of photon linear polarisation at the desired photon energy. The degree of polarisation was determined by a phenomenological fit to the coherent enhancement. The uncertainty in the fitting procedure resulted in the dominant systematic uncertainty of 2% from the detector calibrations.

Chapter 6

Data Analysis

This chapter covers the methods applied in identifying events from single and double π^0 photoproduction from all recorded events.

The software packages used for simulation and analysis are briefly outlined in section 6.1, the procedure for reconstructing the reaction particles from detector signals is discussed in section 6.2. A summary of the sideband subtraction approach to removing the background dilution is given in section 6.3, and finally, how the ${}_s\mathcal{P}lot$ technique[104] has been applied and the advantages of its use in the removal of background contributions are discussed in detail in section 6.4.

Table 6.1 gives a summary of the number of events passing each step of the analysis. Of the order of 750 million events were recorded in the output from the data acquisition. The total events in each linear polarisation setting is about equal at half of the total events.

Analysis stage	π^0p candidate events	$2\pi^0$p candidate events
Calibrated signals	750×10^6	750×10^6
Cut by particle numbers	430×10^6	78×10^6
Prompt tagged photon cut	150×10^6	6×10^6
Background subtracted	120×10^6	2×10^6

Table 6.1: Events at each step of the analysis. Energy ranges for the tagged photon cut are 300< E_{tagged} <675 MeV for π^0 and 520< E_{tagged} <650 MeV for $2\pi^0$.

6.1 Software

AcquRoot [105] is specialist software developed in Glasgow to process data from experiments in the A2 Hall. It has functionality in both data acquisition and analysis, providing the framework for researchers to take raw input signals and reconstruct particle 4-vectors. Written in C++, AcquRoot utilises the ROOT [106, 107] libraries. ROOT is a framework designed to handle large data sets with easy access to advanced statistical techniques. The framework is constantly under development by the international physics community.

The main function of AcquRoot in this analysis is in applying post-run calibrations to detector signals and reconstructing particle properties from the resulting clusters. A ROOT tree is filled for each triggered event, containing all reconstructed particle 4-Vectors, along with tagger timing, photon energies and polarisation information. Most of the details of the detector calibrations conducted with AcquRoot were covered in chapter 5.

Additional software developed during this analysis is also built in the ROOT tree framework, where a tree is a structure for storing large quantities of data. The tree is designed for quick, selective, sparse scanning of data, which is often required in high energy physics experiments. The steps taken using the analysis software are described below.

6.2 Event Selection

This section covers the procedure involved in selecting events for the two reaction channels studied: $\gamma p \rightarrow \pi^0 p$ and $\gamma p \rightarrow \pi^0 \pi^0 p$. Events are selected by cutting on the number of reconstructed particles, which are all assumed to be photons, and conducting a χ^2 test on the two photon invariant mass ($M_{\gamma\gamma}$) combinations to identify the π^0 decay photons.

The initial division of events into the two reaction channels is based solely on the

number of particle clusters reconstructed in the CB and TAPS. The decay $\pi^0 \rightarrow 2\gamma$ requires two clusters for each π^0 produced, with an additional recoiling proton cluster potentially being detected. For each event, the total number of clusters detected is used to identify the reaction channel as shown in figure 6.1. Events with two or three clusters are identified as $\gamma p \rightarrow \pi^0 p$ candidates whereas events with four or five clusters are identified as candidates for $\gamma p \rightarrow \pi^0\pi^0 p$ reactions.

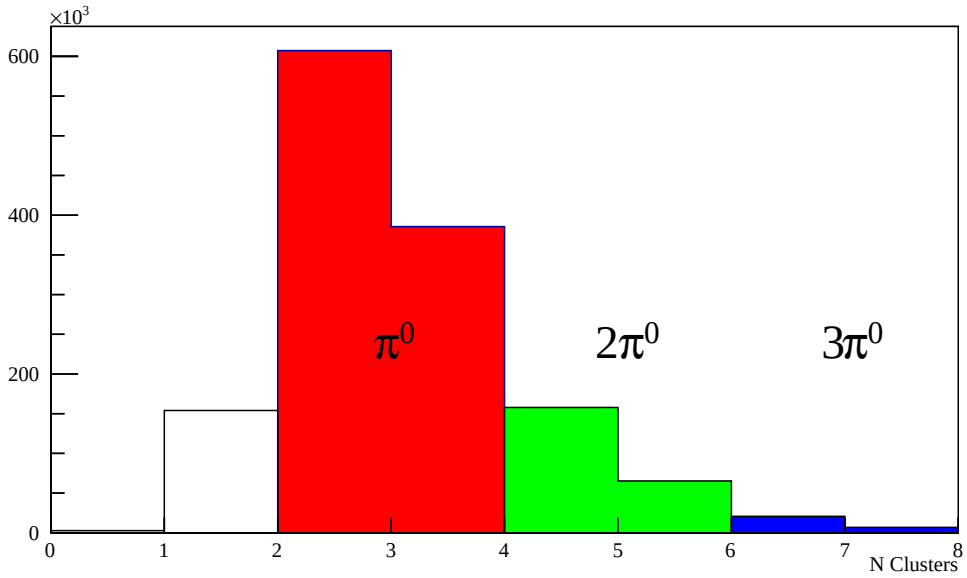

Figure 6.1: Initial event reaction ID based on the number of clusters constructed in the CB and TAPS.

The remainder of this section focuses on the more complex kinematics of the $2\pi^0$ channel with the procedure for the π^0 channel following a simpler version of the same formula.

6.2.1 Missing Proton

The $2\pi^0 p$ decay channel contains five particles in its final state; four photons and a proton. Making the assumption this is the final state allows for the explicit detection of only the photons with the properties of the proton inferred as a missing particle. Deviation in the properties of the missing particle from the properties of the proton is later used to determine the likelihood the reaction channel is correct.

One advantage of not requiring the detection of the recoil proton is that accepted events covered a larger range of kinematics. This is due to the momentum of the proton at backwards polar angles being insufficient to register in the detectors. Accepted events relating to when a detected recoiling proton is both required and not required, are shown as a function of photon energy and pion polar angle (θ_π) in figure 6.2. An additional advantage comes as a consequence of the carbon recoil polarimeter, which was designed to scatter the proton and so when a cluster is identified as a potential proton, the 4-vector of the reconstructed particle may not match the initial recoil vector.

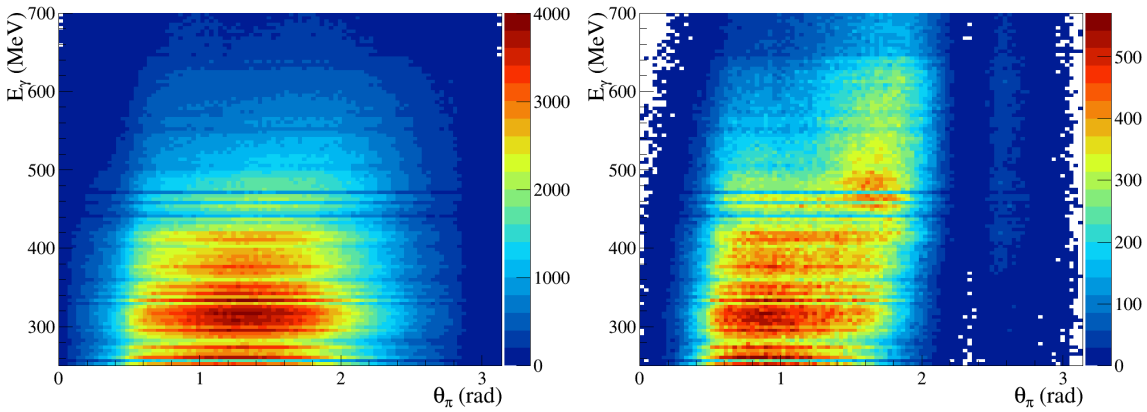

(a) No Recoil Required (b) Recoil Required

Figure 6.2: Distribution of accepted single π^0 events as a function of θ and photon energy. Left - Events with two or three clusters. Right - Events with three clusters, requiring a recoiling proton. Without the recoil required, the angular acceptance of events as well as the total number of events is greater.

In order to reconstruct the missing recoil proton $\boldsymbol{p_R}$, 4-vectors of the following incident and final state particles are required:

- Tagged bremsstrahlung photon 4-Vector. $\boldsymbol{\gamma_B} = (0,0,E_\gamma,E_\gamma)$
- Proton target 4-Vector. $\boldsymbol{p_T} = (0,0,0,M_p)$
- 4-Vectors of the two neutral pions. $\boldsymbol{\pi^0_1}, \boldsymbol{\pi^0_2}$

The coincident $\boldsymbol{\gamma_B}$ energies are provided by the tagger, each considered as possible initiators of the triggered event. The target is assumed to be a proton and so is given the proton PDG mass, stationary in the lab frame. Identifying the $\boldsymbol{\pi^0_1}$ and $\boldsymbol{\pi^0_2}$

vectors is more involved as there are several potential combinations of decay photon 4-vectors that could be used to reconstruct $\boldsymbol{\pi^0}$ candidates. A fairly simple approach is made based on $M_{\gamma\gamma}$, discussed below.

π^0 Reconstruction

From the array of detected particles it is necessary to identify the combination that best fitted the kinematics of the $2\pi^0$p decay channel. This is achieved by reconstructing π^0 candidates from two decay photon 4-vectors and testing the mass of the resulting particle against the PDG invariant mass of the π^0.

After decay, particles are reconstructed by summing together the vectors of their decay products.

$$\mathbf{p_{init}} = \sum_{i=1}^{n} \mathbf{p_i}, \tag{6.1}$$

where $\mathbf{p_{init}}$ denotes the 4-momentum of the mother particle and $\mathbf{p_i}$ the 4-momentum of each daughter particle. In the case where there are only two daughter particles, the mother particle's invariant mass is given by

$$m_{inv} = \sqrt{(\mathbf{p_1} + \mathbf{p_2})^2} = \sqrt{m_1^2 + m_2^2 + 2(E_1 E_2 - \overrightarrow{p_1} \cdot \overrightarrow{p_2})}, \tag{6.2}$$

where m_{inv} is the mother particle's reconstructed mass, $m_{1,2}$, $E_{1,2}$ and $\overrightarrow{p_{1,2}}$ are respectively the masses, energies and 3-momenta of the daughter particles.

For the decay $\pi^0 \to 2\gamma$ this simplifies with $m_\gamma = 0$ to

$$m_{\pi^0} = \sqrt{2(E_{\gamma_1} E_{\gamma_2} - \overrightarrow{p_1} \cdot \overrightarrow{p_2})}. \tag{6.3}$$

Events identified as $2\pi^0$p candidate events had either four or five associated 4-vectors; four of these are attributed to π^0 decay photons with the fifth a recoiling proton. When extracting polarisation observables, it is necessary to identify which

pairs of 4-vectors formed the separate π^0s.

When four particles are detected, three combinations of photon pairs need to be considered, when including a fifth particle (the proton cluster) the combinations increase to fifteen with each of the five vectors, in turn, excluded. The correct pairings for the daughter photons are determined by testing each combination where the invariant masses of the π^0 candidates are compared to the PDG mass of the π^0. The chosen combination is taken as the minimum ΔM from

$$\Delta M^2 = \Delta m_a^2 + \Delta m_b^2 = (m_{\pi^0} - m_a)^2 + (m_{\pi^0} - m_b)^2, \tag{6.4}$$

where m_{π^0} is the PDG value for π^0 invariant mass and $m_{a,b}$ are the π^0 candidate masses. The smallest value of ΔM gives a best guess as to the correct combination of photon pairs. Figure 6.3 shows the invariant mass of the photon combinations for $2\pi^0$ photoproduction, before and after the best candidates have been identified.

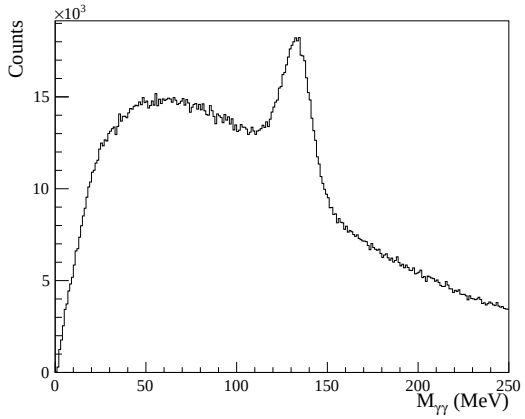

(a) $M_{\gamma\gamma}$ projection all combinations

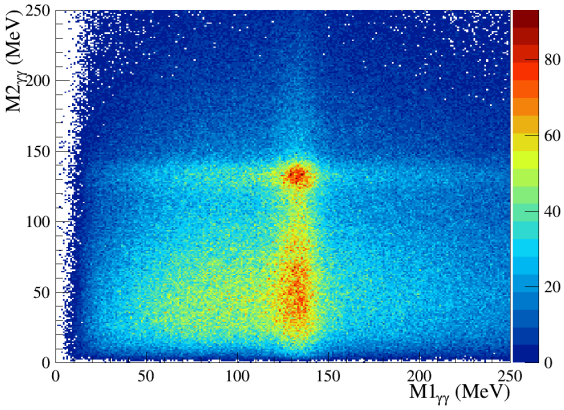

(b) $M1_{\gamma\gamma}$ against $M2_{\gamma\gamma}$ all combinations

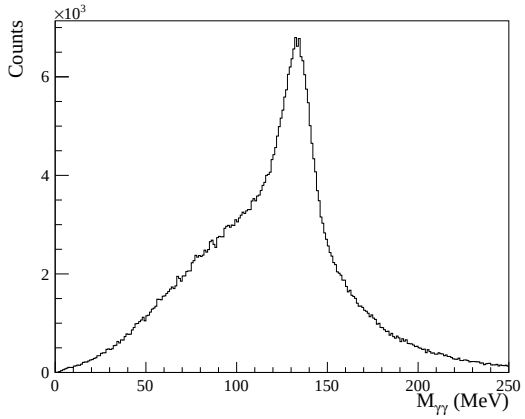

(c) $M_{\gamma\gamma}$ projection best combination

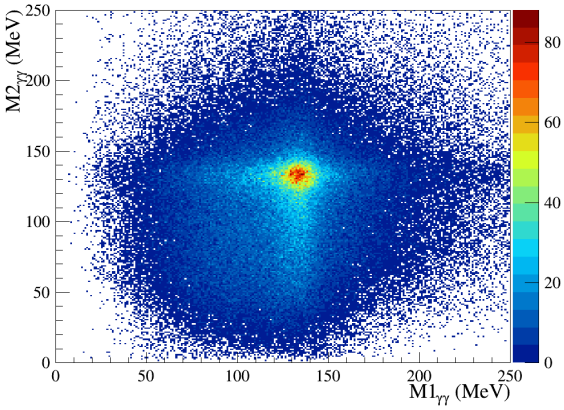

(d) $M1_{\gamma\gamma}$ against $M2_{\gamma\gamma}$ best combination

Figure 6.3: Invariant mass distribution of π^0 candidate from photon pairs. Left - Histograms filled with both combinations. Right - 2D plot showing both masses. Top - all combinations. Bottom - best selected combination with a clear peak at 135 MeV (PDG π^0 mass). The symmetry between the two pion mass distributions is broken by the ordering of the photon clusters, the clusters are ordered by energy in AcquRoot so that the first combination will always contain a higher energy photon.

The distribution of $M_{\gamma\gamma}$ for the selected combination of photons in single π^0 photoproduction is shown in figure 6.4.

The selected π^0 candidate 4-vectors are given the PDG invariant mass of the π^0 while their lab 3-Vectors are kept constant. For a small number of events the combination will have been incorrectly identified, this is determined to have a negligible effect on the final measurements. Alternatively the detected clusters may not have been the result of photons. The events where this occurs are excluded through an

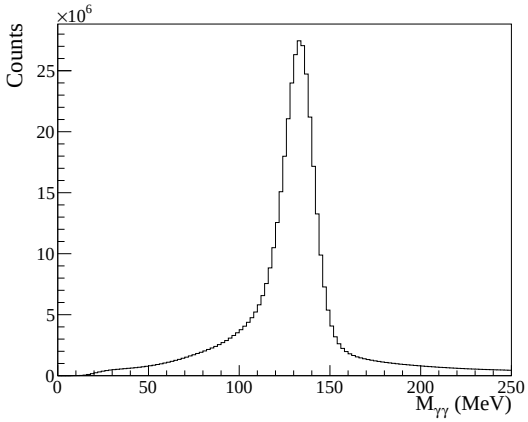

Figure 6.4: $M_{\gamma\gamma}$ from π^0 photoproduction.

investigation of the mass of the missing vectors.

Proton Reconstruction

After the identification of the π^0 vectors, the missing proton recoil vector is calculated for each tagged photon ($\boldsymbol{\gamma_B}$)

$$\mathbf{p_R} = \mathbf{p_T} + \boldsymbol{\gamma_B} - \left(\boldsymbol{\pi_1^0} + \boldsymbol{\pi_2^0}\right) \tag{6.5}$$

The mass distribution of the reconstructed missing 4-Vectors is shown in figure 6.5. There is a peak at the expected proton PDG mass with a large background which largely consists of tagged bremsstrahlung photons which are in random coincidence with the reaction, also with additional background from events with a misidentified reaction ID.

The tagged bremsstrahlung photon can not be uniquely identified for each event, two different techniques tested to account for the random coincidence events are explained in sections 6.3 and 6.4.1. The separation of the signal from background sources in the remaining events in this analysis is handled with the ${}_s\mathcal{P}lot$ technique (section 6.4.2). First an outline of a more conventional sideband subtraction approach is given so the advantages of using the ${}_s\mathcal{P}lot$ technique become apparent.

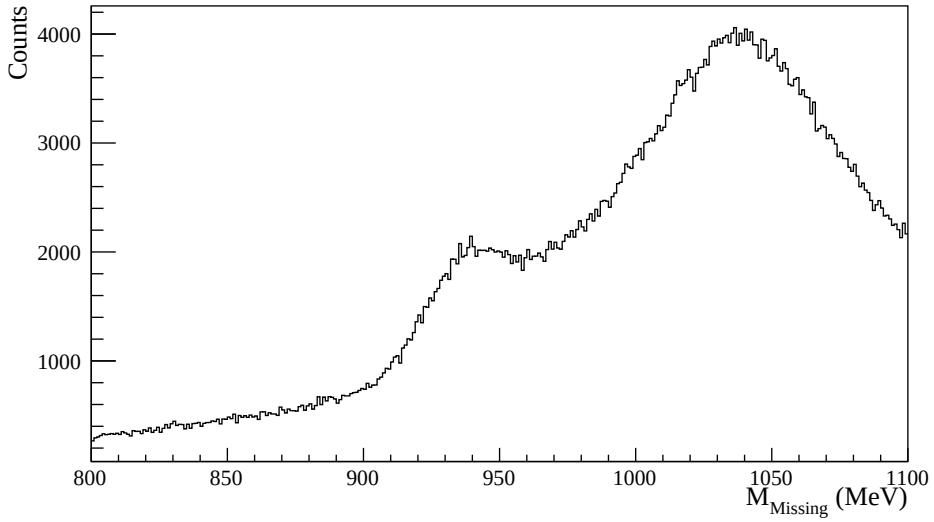

Figure 6.5: Missing mass distribution after π^0 candidates have been selected, calculated with all tagged photons. From kinematic bin [1326<W<1329 MeV, 86< θ_π <92°].

6.3 Sideband Background Subtraction

This section summarises the sideband subtraction method for removing background contributions to the signal. This method has been used in several previous similar analyses. However it is not without deficiencies. The sideband subtraction involved making multiple cuts on the data to limit the accepted kinematics close to that expected in the decay process. For simplicity this section will discuss the π^0p decay channel.

The first cut is made on the best selected $M_{\gamma\gamma}$, the loose cut is made at 3σ of a Gaussian fitted to the peak. Cut limits of $98 < M_{\gamma\gamma} < 172$ MeV are shown in figure 6.6

Next the reaction prompt photon energy is identified statistically by subtracting events reconstructed with random photons, outside of the coincident peak, from those in coincidence with the trigger. Figure 6.7 shows the cuts made on the timing peak along with the mass of the missing 4-vector relating to each cut region. The events in the background cut are weighted so the integral is equivalent to the integral of random events under the coincidence peak.

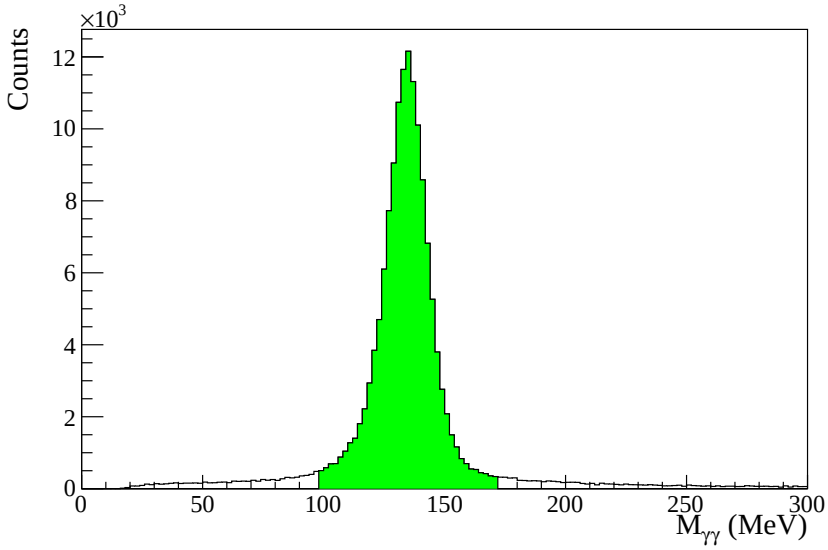

Figure 6.6: Cut made on invariant mass of events. From kinematic bin [1420<W<1422 MeV, 111< θ_π <117°].

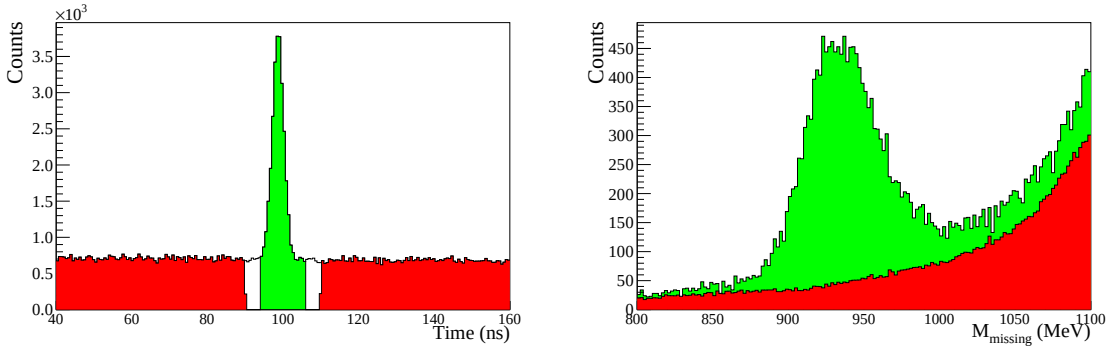

(a) Timing peak cuts

(b) Timing scaled missing mass contributions

Figure 6.7: Left - Time cuts used for prompt signal (green) and random background events (red). Right - Missing mass of events from prompt and random regions, random events scaled to contribute equally based on time. From kinematic bin [1420<W<1422 MeV, 111< θ_π <117°].

Next a cut is made on the mass of the missing vector at 2σ of a Gaussian fitted to the proton peak. The width of the peak increases with higher incident photon energy, where the cut is made in the range $2\sigma = 75 \rightarrow 175$ MeV. Events outwith this cut are assumed to represent a sample of the background events underneath the signal peak. Figure 6.8 shows the missing mass distribution after the tagger random subtraction is made, also demonstrating the missing mass ranges which are designated as signal and background.

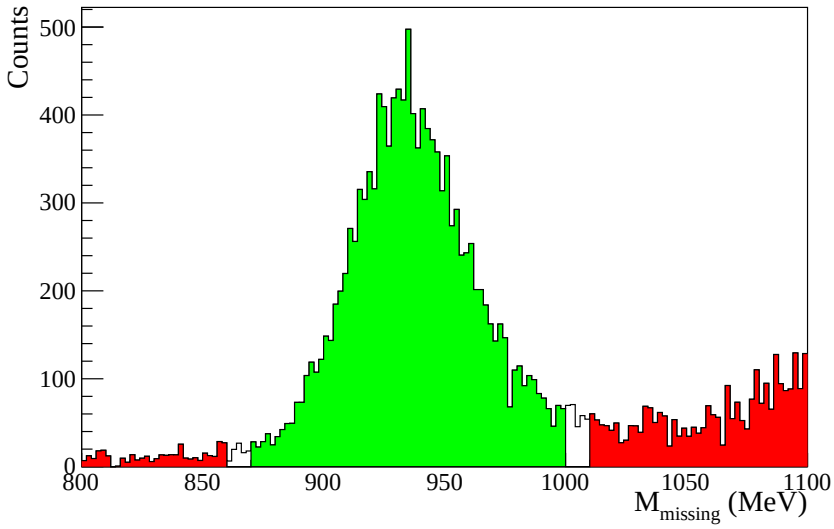

Figure 6.8: Cut made for signal (green) and background (red) missing mass of events. From kinematic bin [1420<W<1422 MeV, 111< θ_π <117°].

The remaining background dilution in the peak is quantified by using a simple model, the signal contribution is described by a Gaussian model, and the background is modelled as second order polynomial. An example of the fit is shown in figure 6.9.

The fraction of the total integral attributed to the background polynomial describes the remaining background in the peak region, in figure 6.9 this is estimated to be of the order 20%. Using a method similar to the tagger random subtraction, events taken from the sidebands are scaled to match the integral of the background and subtracted from the events in the peak region. The effects of this sideband subtraction on the invariant mass and azimuthal ϕ angle are shown respectively in figures 6.10 and 6.11.

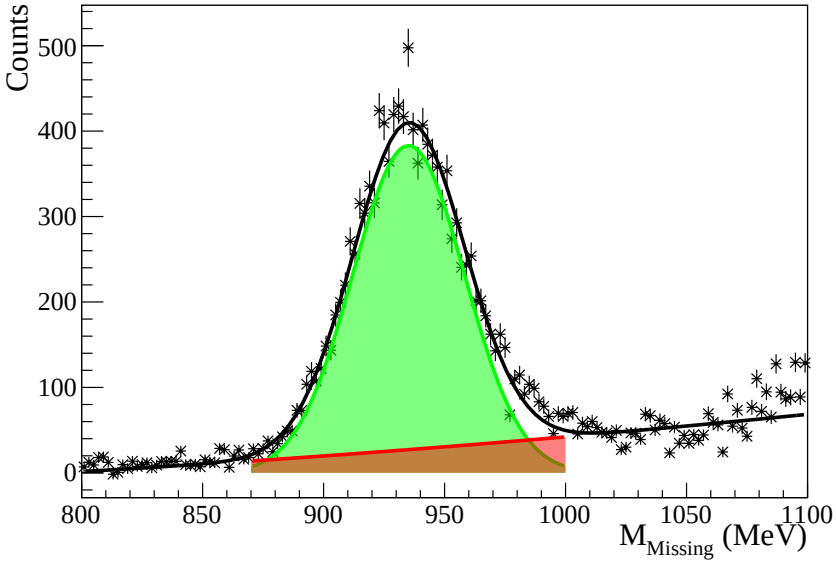

Figure 6.9: Model fit to the missing mass of the data (black stars). The fit is described as the sum (black) of a Gaussian (green) representing signal events and a second order polynomial (red) representing background events. From kinematic bin [1420<W<1422 MeV, 111< θ_π <117°].

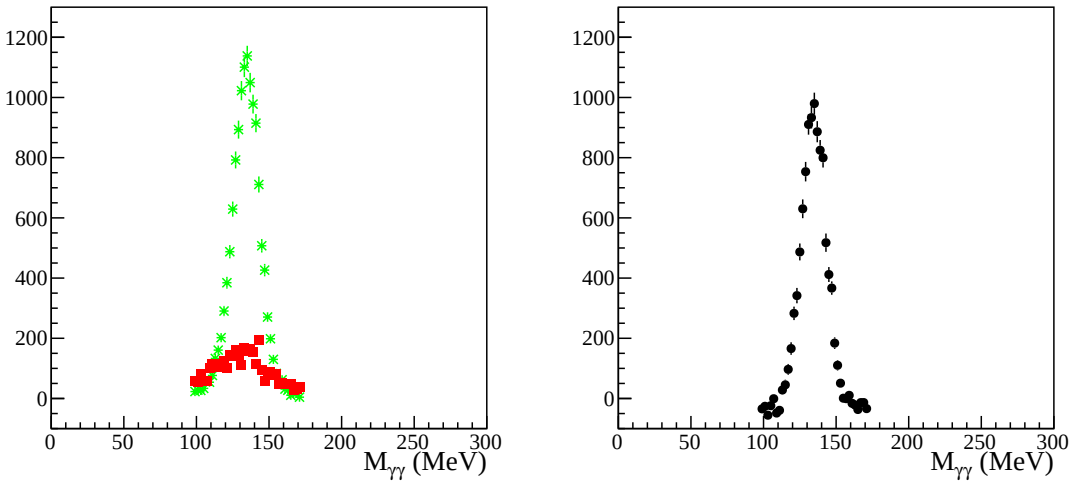

Figure 6.10: Invariant mass distributions showing the effects of a sideband subtraction. Left - Distributions associated with missing mass cuts, (green) proton peak cut, (red) sideband distribution scaled to background dilution. Right - Sideband subtracted events. From kinematic bin [1420<W<1422 MeV, 111< θ_π <117°].

The ϕ distribution of events from the proton mass peak show a strong $\cos 2\phi$ dependence whereas the distribution of events from the sidebands show no significant ϕ

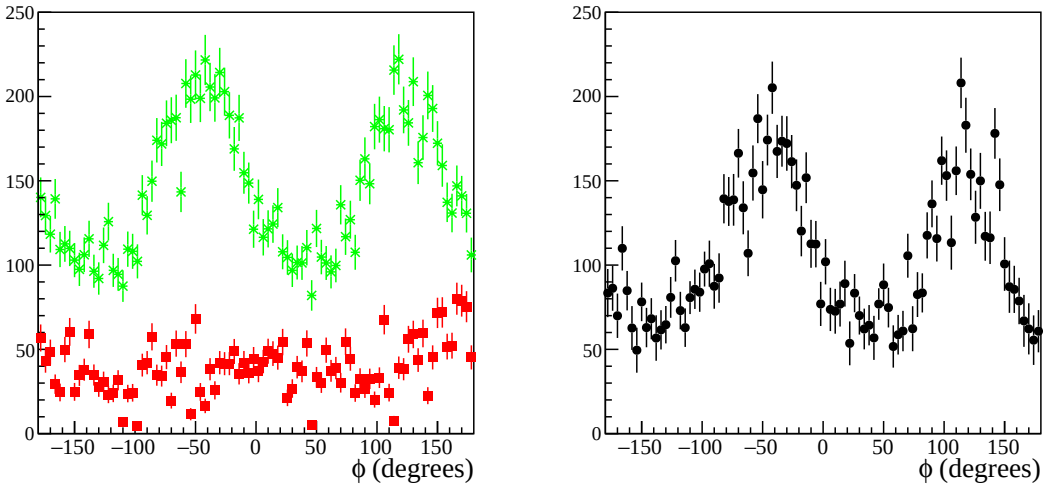

Figure 6.11: Phi distributions showing the effects of a sideband subtraction. Left - Distributions associated with missing mass cuts, (green) proton peak cut, (red) sideband distribution scaled to background dilution. Right - Sideband subtracted events. From kinematic bin [1420<W<1422 MeV, 111< θ_π <117°].

dependence. From the invariant mass plots it is shown that the background contribution has been slightly over estimated by the fit, with the event counts dropping below zero either side of the peak. A model which more accurately describes the signal and background components for the fit could be employed to improve the estimate.

The sideband subtraction method has been used to acquire accurate measurements, however a key drawback comes from the assumption that the events in the sideband have the same properties as the background events within the signal peak, this can be a significant source of systematic uncertainty. Away from the proton mass peak it is less likely that the nature of the sideband events will be equivalent to the background events, for this reason sidebands are limited to the statistics close to the peak.

The associated uncertainties in the sideband subtraction become more prevalent in the $2\pi^0$ channel where there are many contributing background sources, some of which will have a significant ϕ dependence. The total background contribution is as much as 90% in some kinematic bins.

The ${}_s\mathcal{P}lot$ method, discussed in detail in section 6.4, has the advantage of using

only events in the final data range to identify the background contribution rather than introducing new negative events to try and cancel the background out as with the sideband subtraction. A comparison of the methods is discussed in section 6.4.3.

6.4 ${}_s\mathcal{P}lot$ Weighting

The ${}_s\mathcal{P}lot$ technique[104] is used to untangle desired signal events from background contributions using event-by-event weighting. Weights calculated using this technique are described as sWeights. Further discussion of the technical aspect of the technique is given in appendix A.1.

In this analysis sequential ${}_s\mathcal{P}lot$ fits are applied; firstly to separate out tagger random events and then to separate background reaction processes from the signal reaction channel. The resulting signal weighted events are shown to have little to no remaining background contamination.

6.4.1 Timing Fit

The primary fit is made to the timing peak in order to untangle the tagged photon from those in random coincidence. The resulting weighted event distributions represent the physics from events in the target.

The nature of the photon timing peak is shown in figure 4.11, this shape can be described as a sharp Gaussian signal peak about twice the magnitude of a level background. The probability density functions (PDFs) used in the ${}_s\mathcal{P}lot$ fit to the data reflect this; a Gaussian to fit the signal events, and a first order polynomial for the random events. The results of a maximum likelihood fit of the sum of these PDFs to the timing distribution of the data is shown in figure 6.12.

sWeights are calculated from the fit, reflecting the probability an event is either signal or background depending on where in the tagger time distribution it occurs.

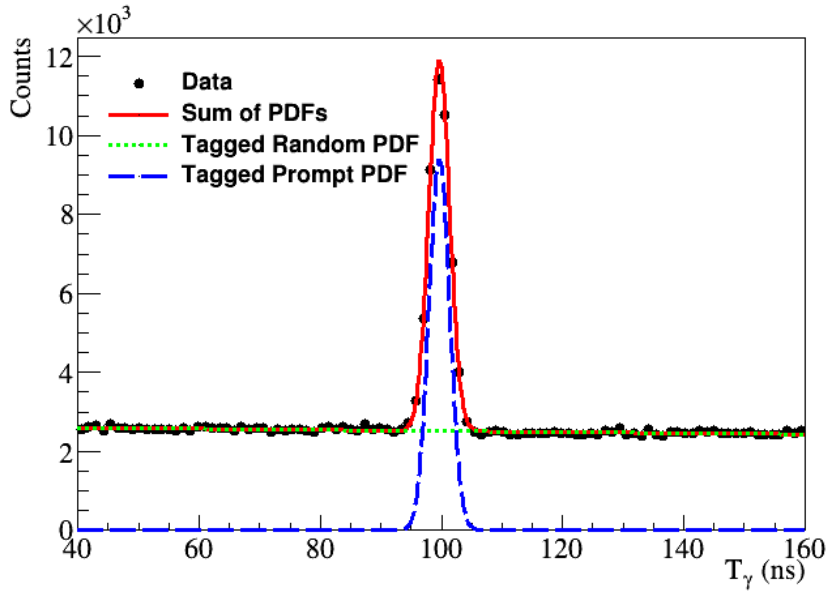

Figure 6.12: Results of a maximum likelihood fit to the tagged time distribution. The signal peak is fit with a Gaussian, and the random background with a line. From kinematic bin [1326<W<1329 MeV, 86< θ_π <92°].

Applying the signal and random background sWeights from this fit to the events produced the missing mass distributions shown in figure 6.13. The tagged random weighted distribution shown has no peak at the proton mass whereas the signal weighted distribution is dominated by it.

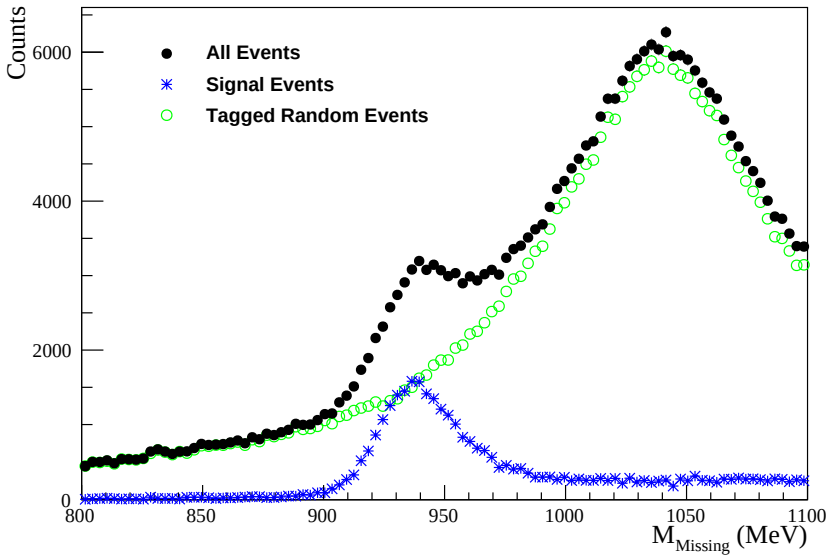

Figure 6.13: Missing Mass of all events weighted by; signal (blue), random (green), and un-weighted data (black). From kinematic bin [1326<W<1329 MeV, 86< θ_π <92°].

This tagger time fit is used to identify the photon which prompted the reaction in the target. The events weighted with the prompt signal sWeights still contain background contributions from misidentified reactions.

6.4.2 Missing Mass Fit

An ${}_s\mathcal{P}lot$ fit is next applied to the missing mass distribution of the prompt timing weighted-events. The distribution of $M_{Missing}$ is used because the different sources of background had distinctive contributions which can be evaluated separately to disentangle their contributions.

Each source of events contributes differently across the $\cos\theta$ and E_γ kinematic range, thus in order to get the most accurate model for the background each bin is treated independently. Sources of events considered as contributors to the data are $\gamma p \rightarrow \pi^0 p$, $2\pi^0 p$, γp scattering, $\pi^+ n$, $\pi^+\pi^0 n$, $\pi^+\pi^- p$ and target cell interactions.

The main source of background which contributed to both the π^0 and $2\pi^0$ photoproduction channels has been determined to be events originating from the target cell. The contribution from the target is quantified from a small number of dedicated runs, where the experiment was conducted under the same conditions as production runs but with the target cell evacuated. The empty target data is analysed identically to the production runs, producing timing sWeighted events now only originating from the target cell. The magnitude of the target cell contribution to the production data is given by the ratio of the tagged photon total fluxes incident on the target during empty target and production runs. For the data available from this experiment the ratio of empty target events to production events is 1:7.5.

For events originating from the LH_2 there is no experimental method of disentangling the contribution of the background channels from the signal channel; instead the Geant4[94] simulation of the A2 experimental setup is utilised. Ten million events were generated for the signal channel and each of the background channels across the full range of $\cos\theta$ and E_γ analysed. Generated events for each channel are run independently through the simulation and subsequent analysis as with experi-

mental data, although no tagger subtraction is required as E_γ is known as an input to the simulation. The resulting distribution of events is used as a representation of those expected to contribute to the data.

The $M_{Missing}$ distributions of the simulated signal and background channels are used as PDFs in a fit to the data. Figures 6.14 and 6.15 show the shapes of the PDFs considered respectively in the fitting of a single kinematic bin in π^0p and $2\pi^0$p photoproduction.

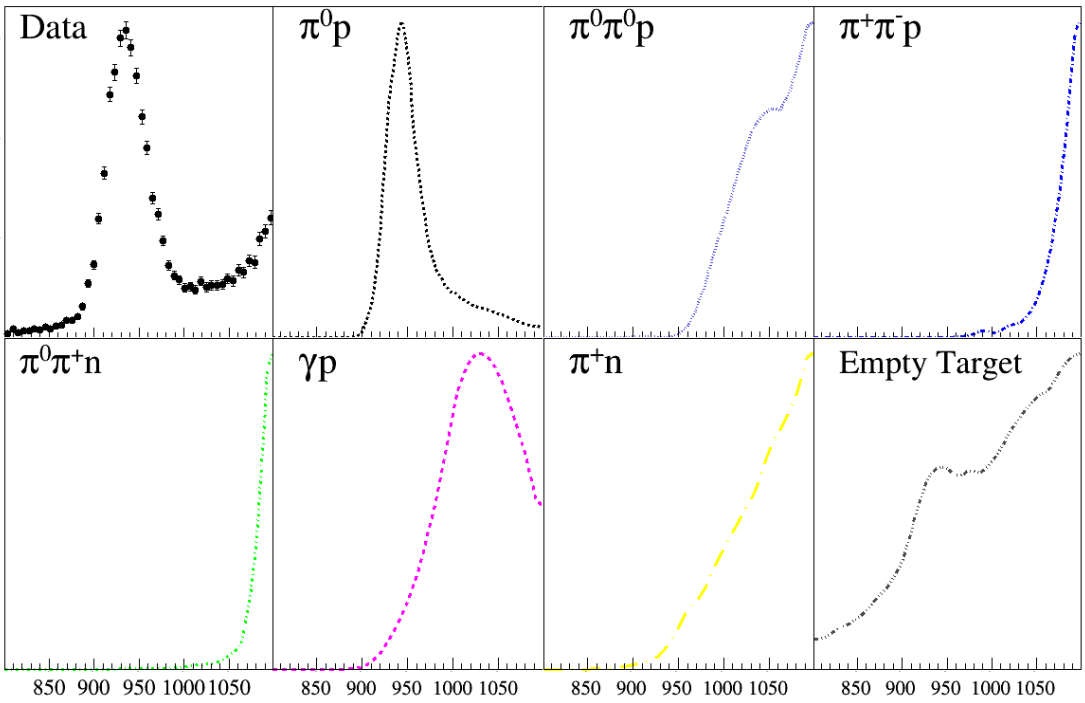

Figure 6.14: PDFs considered as contributors to the $M_{Missing}$ distribution in MeV of π^0p data. From kinematic bin [1420<W<1422 MeV, 111< θ_π <117°].

Some simulated reaction channels only have a small percentage of events accepted by previous analysis cuts, the PDFs constructed using these low statistics are not smooth. The small number of events making the cut implies there is unlikely to be much contribution of that reaction channel as a background to the signal shape, this can not however be the only indicator used. In this process the relative cross sections of the reactions are not taken into account. Some channels, for example Compton scattering, have a large percentage of events that get misidentified as π^0p signal events, however the cross section of this channel in the higher energy regime is

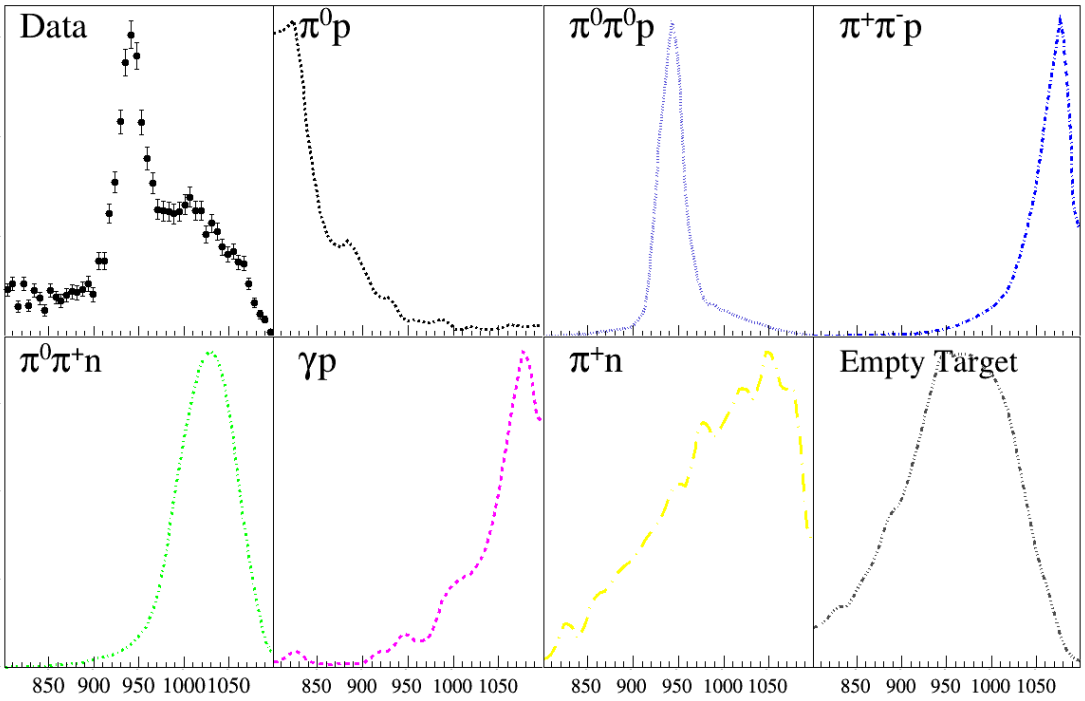

Figure 6.15: PDFs considered as contributors to the $M_{Missing}$ distribution in MeV of $2\pi^0$p data. From kinematic bin [1370<W<1374 MeV, 30< θ_π <60°].

many orders of magnitude lower than that of the signal so is not a strong contributor to the background.

In order to account for any differences between the simulation and experiment some flexibility in the shape of the simulated PDFs is allowed, these parameters are:

- Offset in Energy
- Scale - Stretching in energy
- Gaussian smearing - Each event contributes to the distribution as a Gaussian
- Total percentage contribution of PDF

Each channel's relative contribution to the data could be calculated, given by the ratio of signal-background differential cross sections multiplied by the relative percentage of simulated events that make it through previous cuts. This calculation relies of previous experimental results of varying precision so instead the magnitude is left as a free parameter to be fitted. Two examples of fits for the π^0p channel along with an enhanced plot of the background contributions are given in figures

6.16 and 6.17.

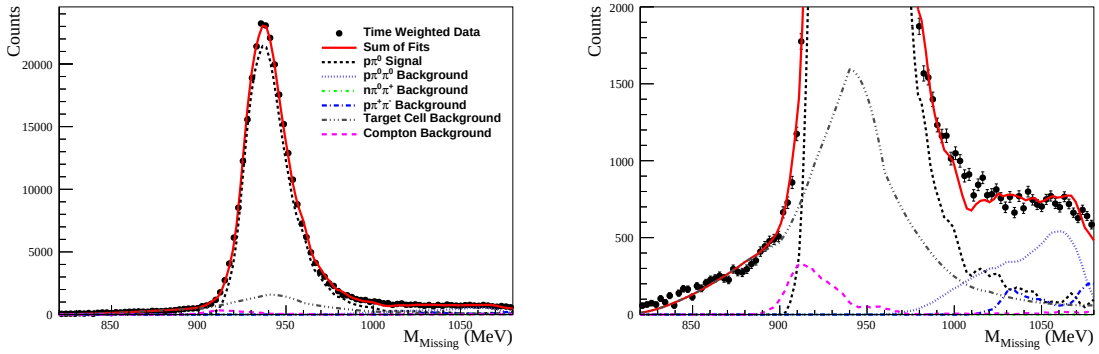

(a) Fit of $M_{Missing}$ (b) Fit background contributions

Figure 6.16: Fit of simulated PDFs to the $M_{Missing}$ distribution of data. From kinematic bin [1244<W<1247 MeV, 86< θ_π <92°].

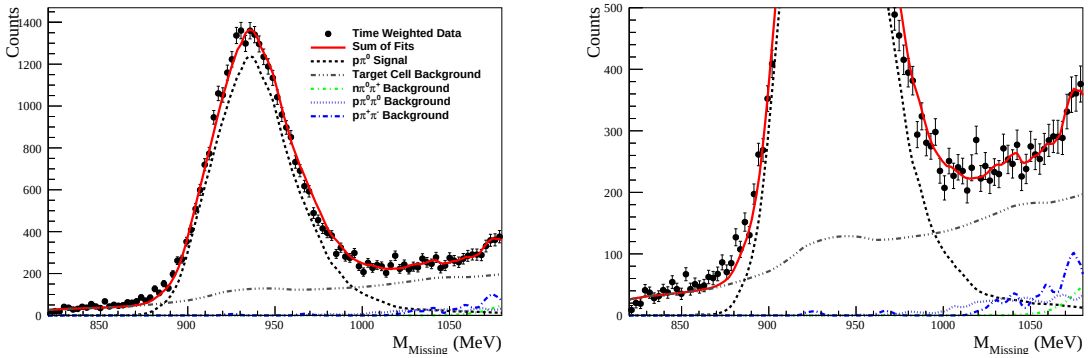

(a) Fit of $M_{Missing}$ (b) Fit background contributions

Figure 6.17: Fit of simulated PDFs to the $M_{Missing}$ distribution of data. From kinematic bin [1420<W<1422 MeV, 111< θ_π <117°].

The main source of background for all of the single π^0 kinematic bins is the target cell. As photon energy is increased, the 2π channel thresholds are passed and need to be considered, a mix of signals from these is measured contributing in the high $M_{Missing}$ region.

Examples of fits to two kinematic bins in the $2\pi^0$p channel are shown in figure 6.18

A significant portion of events masquerading as $2\pi^0$p also come from the target cell, however using events with four or five clusters also increases the acceptance of other

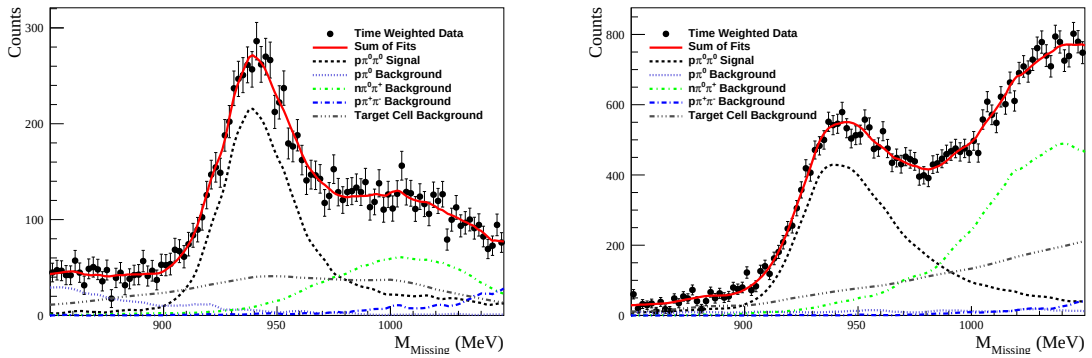

(a) 1370<W<1374 MeV, 30< θ_π <60° (b) 1445<W<1448 MeV, 120< θ_p <138°

Figure 6.18: Fit of simulated PDFs to the $M_{Missing}$ distribution of $2\pi^0$ data.

2π channels. In particular the $\pi^0\pi^+$n channel has four final state particles, two of which could have been correctly reconstructed into the π^0.

Due to the complex nature of the data and PDFs which are fitted, five initial χ^2 fits are carried out with randomised starting parameters. The fit with the lowest χ^2 is used in the calculation of the sWeights through the maximum likelihood fit. The background PDFs are summed together and all parameters other than the total contribution are set constant before the ${}_s\mathcal{P}lot$ fit is conducted. This ensures the relative contributions of the backgrounds are static and the maximum likelihood fit is simplified, with only two free parameters in the calculation of the sWeights for signal and background. Systematic effects of this technique are discussed in section 6.4.3.

The success of the ${}_s\mathcal{P}lot$ fits are reflected in sWeighted plots of $M_{\gamma\gamma}$. Figures 6.19, for single π^0, and 6.20, for $2\pi^0$, show that with no explicit cut on $M_{\gamma\gamma}$, the particles with the π^0 PDG mass have been disentangled from backgrounds. The same figures shown prior to applying the sWeights were shown respectively in figures 6.4 and 6.3.

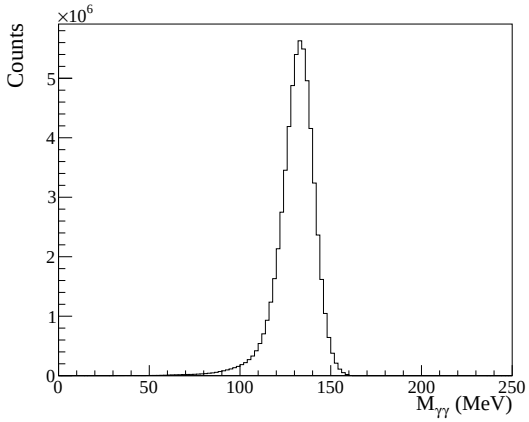

Figure 6.19: sWeighted $M_{\gamma\gamma}$ from π^0 photoproduction.

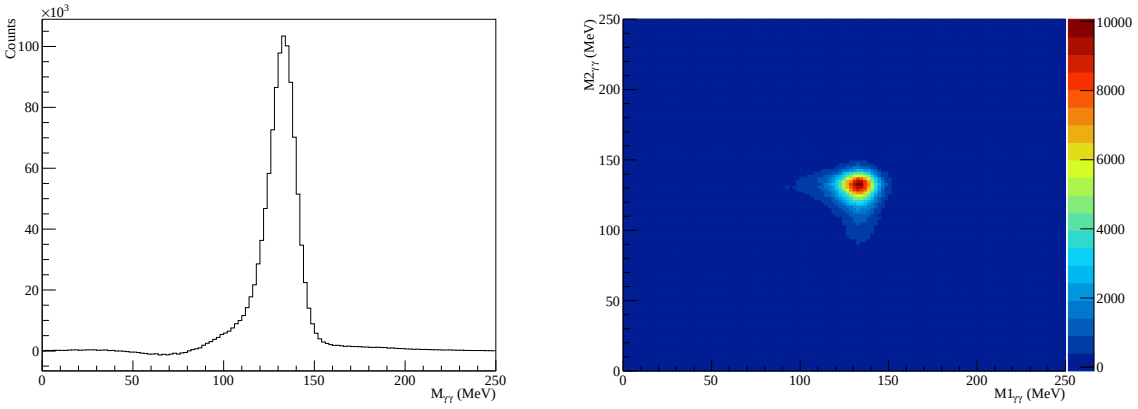

(a) Signal weighted invariant mass projection (b) Invariant mass of signal weighted $2\pi^0$ events

Figure 6.20: sWeighted $M_{\gamma\gamma}$ plots from $2\pi^0$ photoproduction. Left - 1D projection of invariant masses of both reconstructed particles. Right - 2D plot of the two particle masses.

The signal sWeights calculated for the events are used in plotting distributions of any associated variable. The main use in this analysis is producing histograms with sWeighted ϕ distributions from which the polarisation observables are calculated. Figure 6.21 shows an example bin of the ϕ distributions resulting from events weighted with both signal and background sWeights.

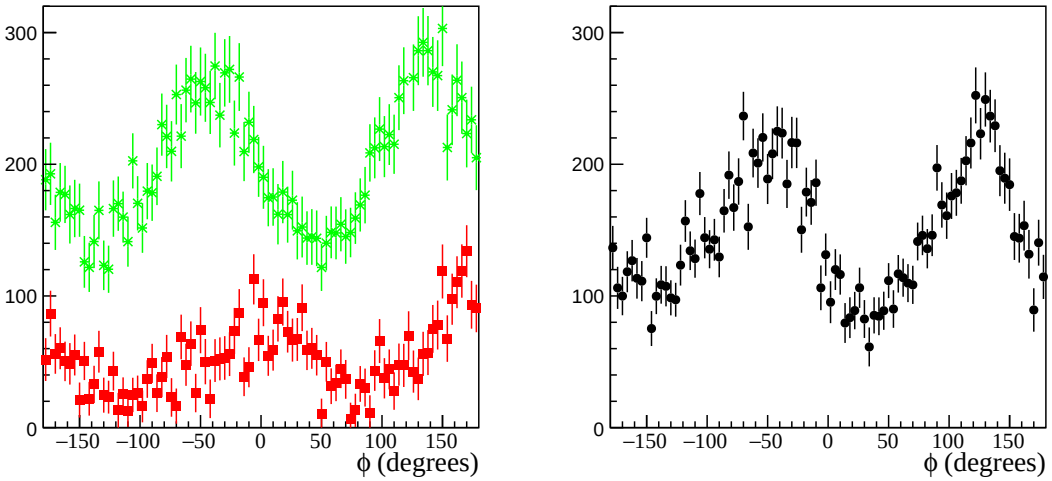

Figure 6.21: Distributions of ϕ, showing the effects of a applying sWeights. Left - (green) un-weighted events, (red) background sWeighted events. Right - Signal sWeighted events. From kinematic bin [1420<W<1422 MeV, 111< θ_π <117°].

6.4.3 Systematic Comparison

A comparison of the sideband and $_s\mathcal{P}lot$ methods of background subtraction in single π^0 photoproduction are shown in figure 6.22. The Σ asymmetry is calculated for the same E_γ and θ bin using an identical initial wide cut on the $M_{Missing}$ and T_γ.

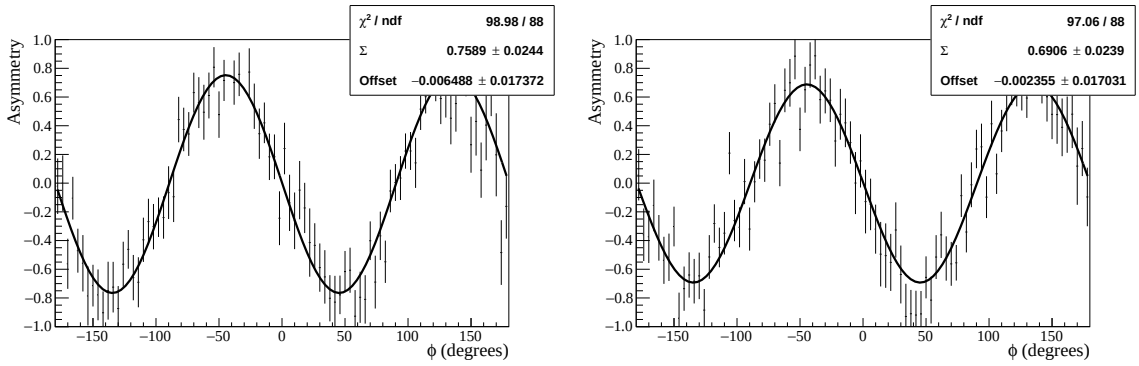

(a) Sideband asymmetry

(b) $_s\mathcal{P}lot$ asymmetry

Figure 6.22: Beam asymmetry Σ calculated from events background subtracted using the sideband subtraction (left) and the $_s\mathcal{P}lot$ method (right).

The sideband subtracted value for Σ is larger than the $_s\mathcal{P}lot$ value due in part to an over estimation of the background contribution, shown in the negative counts for the $M_{\gamma\gamma}$ in figure 6.10.

A comparison of figures 6.11 and 6.21 shows that there is also an asymmetry in the background contribution, under the signal peak, which is not present in the sidebands, this asymmetry is accounted for in the ${}_s\mathcal{P}lot$ fit but is impossible to accurately quantify by using sidebands. It is likely that these events came from π^0 photoproduction off bound nucleons in the target cell, the process of which is expected to have an asymmetry similar to that of those coming from the proton target.

Studies into the systematic uncertainty associated with the two methods have been conducted.

The systematic uncertainty in the sideband subtraction method is directly linked to the estimation of the background dilution. By altering the missing mass range to which the analytical fit is made, a distribution of dilution factors are calculated, the root mean squared (RMS) of this distribution is a good estimate of the error in the total dilution. Figure 6.23 shows the estimated systematic error in the dilution factor for every centre of mass energy and theta bin. Across all bins the average uncertainty from using the sideband subtraction method is in the order of 10%. This could be reduced by implementing a more sophisticated fit model.

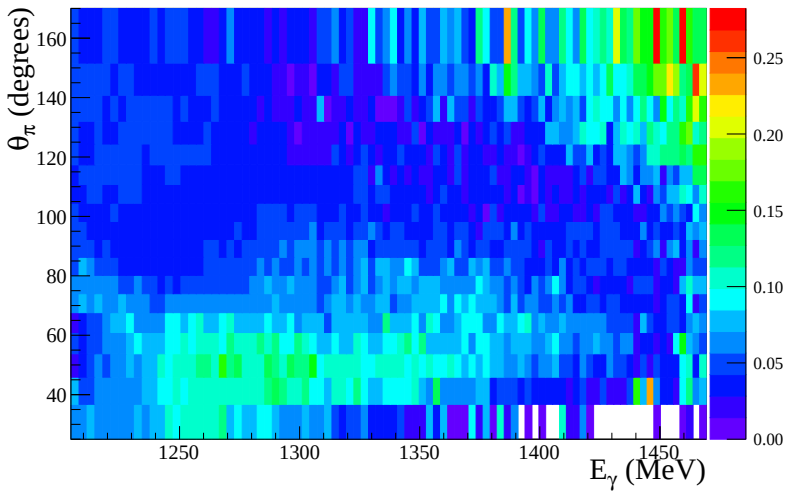

Figure 6.23: Estimation of the fractional systematic uncertainty in the sideband subtraction method across all kinematic bins.

In order to estimate the uncertainty associated with the ${}_s\mathcal{P}lot$ method, three tests

are performed. Firstly, values of Σ in π^0 photoproduction are calculated in five kinematic bins. Two values of Σ are calculated with the signal PDF estimated as a Gaussian, using random tagged photon subtraction of weights derived from prompt-random cuts and comparatively, using weights from a Gaussian fit to the full tagger coincidence distribution. This is repeated using bifurcated Gaussian PDFs as an estimate for the signal shape. From the four values calculated for each kinematic bin, an estimate for the maximum variance across the bins is calculated to be of the order of 2.5%. This systematic test investigated the effects of using different simple PDF shapes.

The second test uses the five χ^2 fits of the simulated PDFs with the initial values of all the parameters laid out in section 6.4.2 randomised. sWeights calculated from each fit are propagated to final values of Σ, the variation in the values is in the order of 1%.

The final test conducted is to determine the effects of summing together the background contributions in order to improve the stability of the fit. Because it is anticipated that the background contributions have different ϕ distributions, summing them together produces a correlation with missing mass. A systematic uncertainty of up to 3% is calculated by conducting a pull analysis between results calculated with and without summing the backgrounds across a number of kinematic bins.

The total systematic uncertainty from the use of the ${}_s\mathcal{P}lot$ method is estimated to be 3% in the single π^0 reaction channel where the discussed investigations explore different aspects of the same uncertainty.

Similar tests are conducted for the $2\pi^0$ channel where the total systematic uncertainty is estimated at 6%. The value is larger in the $2\pi^0$ reaction as the background contributions under the signal peak are more neumerous and average significantly larger than for the single π^0 reaction.

The ${}_s\mathcal{P}lot$ technique provides greater control and therefore confidence in the estimation of background contributions. Error in the estimation of dilution propagates to a lesser degree to the final measurements of Σ and an over estimation of background

can not result in an enlarged Σ so long as the fit has been successful.

6.5 Observable Extraction

This section describes the final process in analysis explaining how polarisation observables are extracted from the kinematics of the selected events. Physical and mathematical interpretations of the observables Σ, I^s and I^c have previously been provided in section 2.4.

6.5.1 Σ Photon Asymmetry

The Σ polarisation observable is a measurement of the sensitivity of the protons excitation and subsequent decay to the linear polarisation of the γ beam. Here the function used in extracting values of the Σ asymmetry is built and finally given in equation 6.12.

Polarisation

A polarisation plane is described by the momentum vector $\overrightarrow{k}$ (beam direction) and electric field vector $\overrightarrow{\varepsilon}$ of the polarised γ. The polarisation of each tagged photon P^T relates to the azimuthal angle away from this polarisation plane by

$$P^T(\phi) = 1 + P^T \cos(2\phi), \tag{6.6}$$

where P^T is the degree of polarisation (5.3) and ϕ is the angle taken anticlockwise around the beam direction, from the polarisation plane. The quantum mechanical nature of the γ means the polarisation distribution may be interpreted as the PDF for a γ interacting with its electric field vector at a particular ϕ angle. The relationship between the linear polarisation of the beam and the azimuthal dependency of

the differential cross section is now given by

$$\frac{d\sigma}{\mathrm{d}\Omega}(\phi) = \left(\frac{\mathrm{d}\sigma}{\mathrm{d}\Omega}\right)_0 (1 + P^T \Sigma \cos(2\phi)), \tag{6.7}$$

where $\left(\frac{\mathrm{d}\sigma}{\mathrm{d}\Omega}\right)_0$ is the un-polarised differential cross section and the polarisation observable Σ is introduced as the sensitivity to the polarisation. Measuring the cross section directly is difficult as the yield measurements are sensitive to detector acceptance such that any measurement introduces additional systematic uncertainties.

Asymmetry

The differential cross section can be excluded from the calculation entirely by taking an asymmetry between yield measurements at two orthogonal polarisation planes, cancelling out the effects of the detector. Figure 6.24 shows the experimental description of the polarisation planes. Measurements were taken with the polarisation planes at angles relative to the lab horizontal, designated *parallel* ($-45°$) and *perpendicular* ($+45°$) in order to avoid either having maximum polarisation along the join between the two halves of the crystal ball.

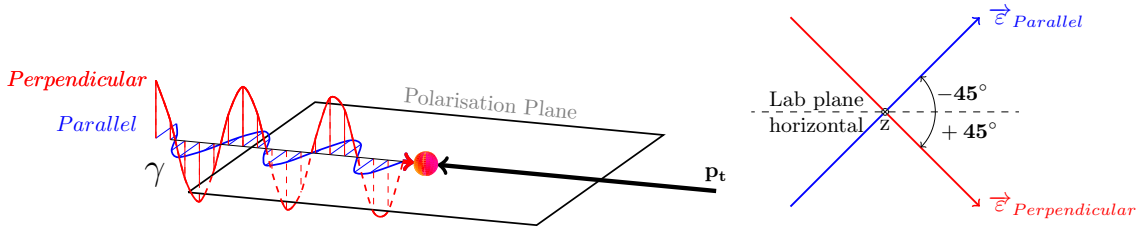

(a) Polarisation frame (b) Polarisation vectors

Figure 6.24: Frames describing the polarisation planes and how they are orientated to the lab frame.

The total yield distribution from each polarisation plane is given as

$$\begin{aligned} N_{\parallel}(\phi) &= A(\phi)F_{\parallel}(1 + P_{\parallel}^{T}\Sigma\cos(2(\phi - 45^{\circ}))), \\ N_{\perp}(\phi) &= A(\phi)F_{\perp}(1 + P_{\perp}^{T}\Sigma\cos(2(\phi + 45^{\circ}))), \end{aligned} \tag{6.8}$$

where $A(\phi)$ describes the detector efficiencies, F is the yield of events and, $\parallel$ and $\perp$ relate to the parallel and perpendicular polarisation planes.

Using the identity $\cos(2\phi - 90^{\circ}) \equiv -\cos(2\phi)$; an asymmetry is formed from the events in each data set,

$$\frac{N_{\parallel}(\phi) - N_{\perp}(\phi)}{N_{\parallel}(\phi) + N_{\perp}(\phi)} = \frac{A(\phi)(F_{\parallel} - F_{\perp} + (F_{\parallel}P_{\parallel} + F_{\perp}P_{\perp})\Sigma\cos(2(\phi + 45^{\circ})))}{A(\phi)(F_{\parallel} + F_{\perp} + (F_{\parallel}P_{\parallel} - F_{\perp}P_{\perp})\Sigma\cos(2(\phi + 45^{\circ})))}. \tag{6.9}$$

When the $\parallel$ and $\perp$ data sets have equal total flux ($F_{\parallel} = F_{\perp}$) and degree of polarisation ($P_{\parallel} = P_{\perp}$) the function simplifies to

$$\frac{N_{\parallel}(\phi) - N_{\perp}(\phi)}{N_{\parallel}(\phi) + N_{\perp}(\phi)} = P^{T}\Sigma\cos(2\phi) \tag{6.10}$$

Naturally the fluxes are not identical, effects of *small* discrepancies in the yields can be accounted for by scaling the data sets to each other

$$\begin{aligned} Y_{\parallel}(\phi) &= F_{\perp}N_{\parallel}(\phi) \\ Y_{\perp}(\phi) &= F_{\parallel}N_{\perp}(\phi). \end{aligned} \tag{6.11}$$

Unequal degrees of polarisation can also be accounted for by dividing the polarisation out of the fit function, scaling the asymmetry denominator fluxes by the polarisation relating to the other data set. The final function used to fit the asymmetry is given

by,

$$\frac{Y_{\perp}(\phi) - Y_{\parallel}(\phi)}{P_{\parallel}Y_{\perp}(\phi) + P_{\perp}Y_{\parallel}(\phi)} = A + \Sigma\cos(2\phi), \tag{6.12}$$

where A provides for the possibility of a small systematic uncertainty in the normalisation of the yields.

6.5.2 Σ - π^0 Asymmetry

Σ varies as a function of θ_{cm} angles and incident γ energies, measurements are made using equation 6.12 with examples of individual fits shown in figure 6.25. The full range of results are presented in section 7.1.

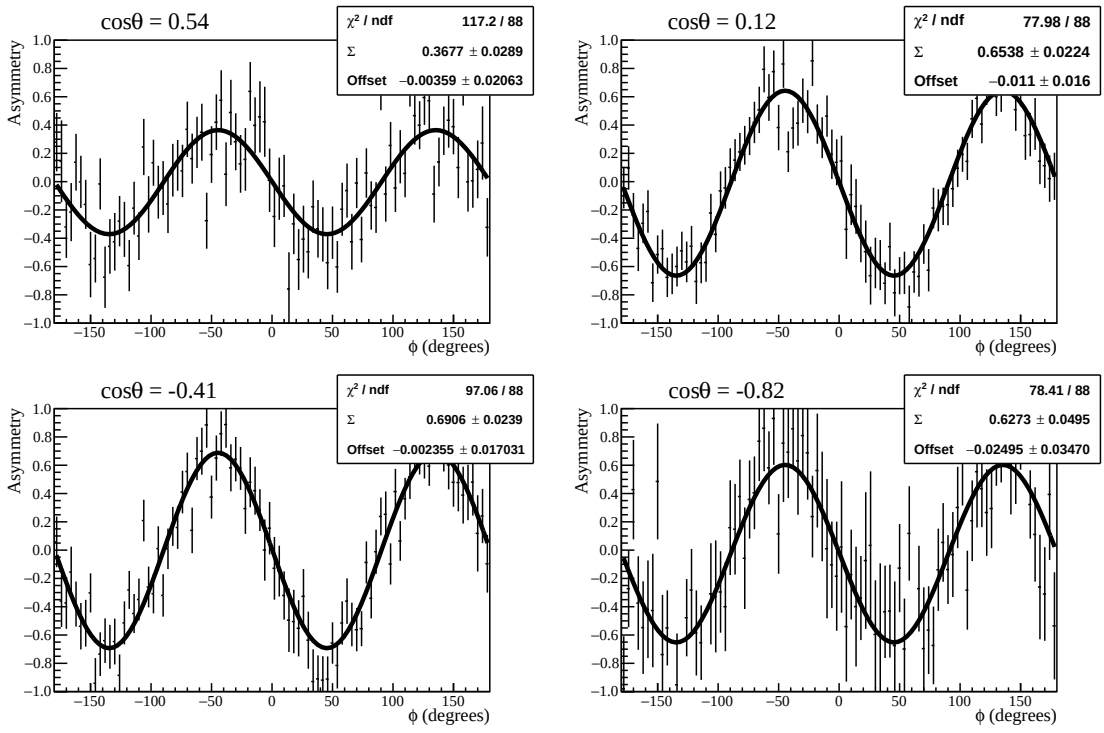

Figure 6.25: Examples of the ϕ asymmetry and fit from the single π^0 decay channel for four $\cos\theta$ bins at 1420<W<1422 MeV.

6.5.3 Σ_p and Σ_π - $2\pi^0$ Asymmetry

The conventions used in presenting values for $2\pi^0$ Σ have varied between publications. Early results from GRAAL[60] describe the observables in terms of the vectors $\overrightarrow{P}_{\pi_1^0+\pi_2^0}$ and $\overrightarrow{P}_{\pi^0}$. The more recent publication from CBELSA[61] uses the definitions adopted in this work (see section 2.4.2).

Values for Σ_p and Σ_π have been measured across a range of incident γ energies and θ_{cm} of the corresponding vector. Figure 6.26 shows examples of the fits to ϕ with full results presented in section 7.2.

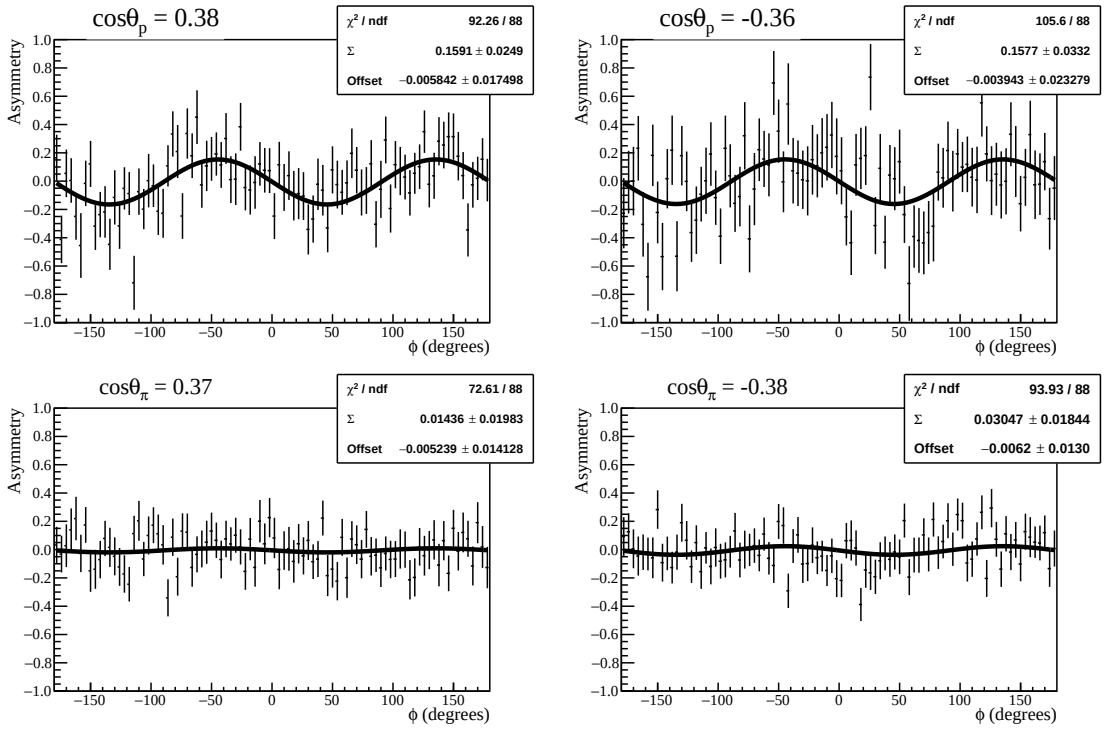

Figure 6.26: Examples of the ϕ asymmetry and fit from the double π^0 decay channel for two $\cos\theta$ bins at 1447<W<1450 MeV in both p and π recoil frames.

6.5.4 I^c and I^s Asymmetry

The extraction of I^c and I^s requires a more complicated fit function. Taking the asymmetry (equation 6.12) of the $2\pi^0$ differential cross section (equation 2.15) we

now have the function,

$$\frac{Y_\perp(\phi) - Y_\parallel(\phi)}{P_\parallel Y_\perp(\phi) + P_\perp Y_\parallel(\phi)} = A + (I^c \cos 2\phi + I^s \sin 2\phi) \tag{6.13}$$

which can be fitted to the data. I^c and I^s can be measured as a function of the three variables Φ^*, $\cos\theta_{cm}$ and E_γ, examples of the fit for different bins are shown in figure 6.27.

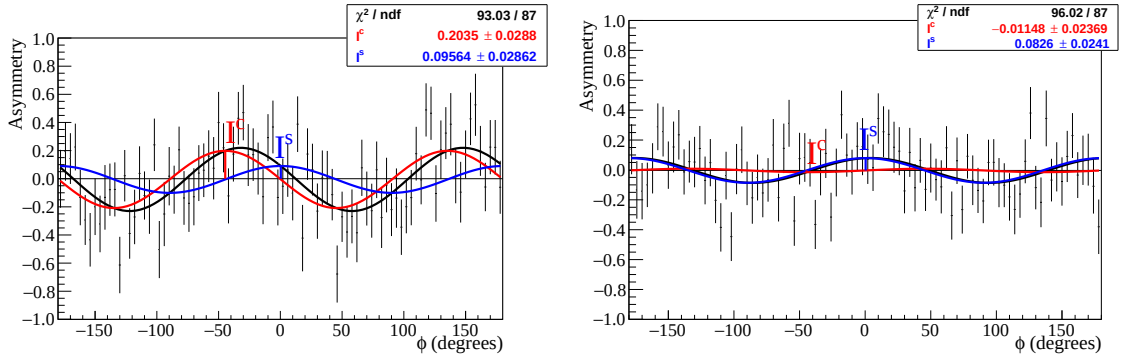

(a) π recoil ϕ example (b) proton recoil ϕ example

Figure 6.27: ϕ fits to the asymmetry (black) extracting values of I^c (red) and I^s (blue). Left - proton recoil frame from kinematic bin [1419<W<1452 MeV, 0.5< $\cos\theta_p$ <1.0, 108°<Φ^*<126°]. Right - π^0 recoil frame from kinematic bin [1419<W<1452 MeV, -0.5< $\cos\theta_\pi$ <0.0, 36°<Φ^*<54°]. The black line is the fit function as a sum of the sin and cosine components.

Figure 6.28 shows the full 2D ϕ-Φ^* asymmetry of the data beside the distribution of the function resulting from fitting equations 6.13, 2.16 and 2.17.

Equations 2.18 and 2.19 describe the transformation of I^c and I^s respectively as even and odd functions of Φ^*, this symmetry allows the results to be plotted beside a mirror operated copy of itself to check the measurements are self consist. An example of the condition is shown in figure 6.29.

Values for I^c_p, I^s_p, I^c_π and I^s_π have been measured across a range of incident γ energies θ_{cm} and Φ^* in the desired frame. Results are presented in section 7.3.

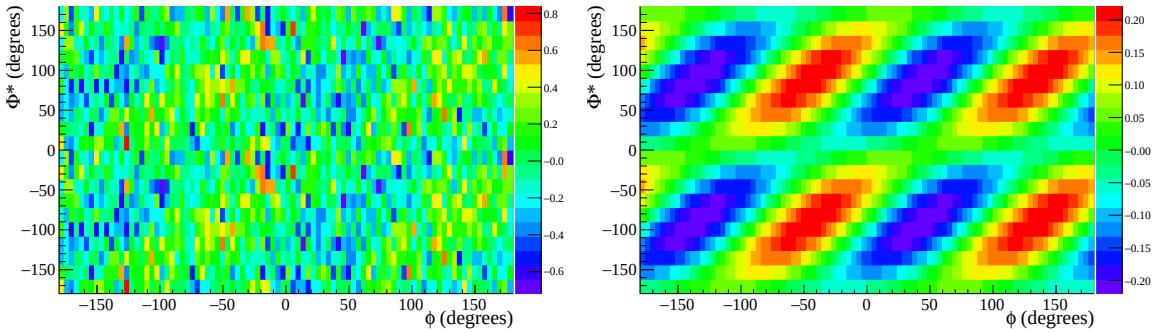

(a) Data (b) Function resulting from fit

Figure 6.28: 2D asymmetry of ϕ-Φ^*. Left - Data. Right - Functional form resulting from fitting the data. Showing the kinematic bin 1419<W<1452 MeV and 0.5< $\cos\theta$ <1.0.

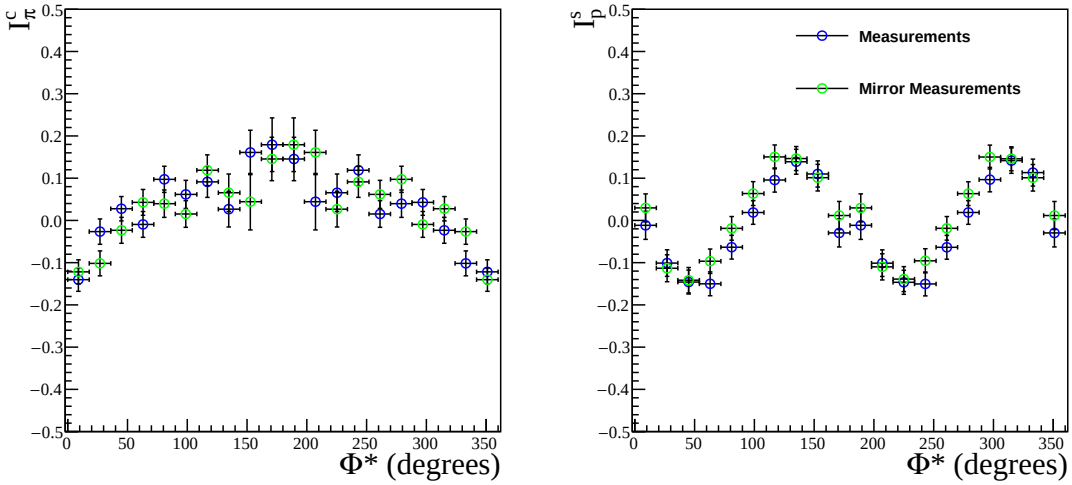

Figure 6.29: Demonstration of the symmetries inherent in measurements of I^c and I^s. Measurements of the observables are plotted alongside mirror operated measurements.

Chapter 7

Results

This chapter shows the results of the analysis conducted for this thesis. Measurements of the polarisation observable Σ are presented with high statistics for single π^0 photoproduction. The observable Σ is also presented for the $2\pi^0$ photoproduction channel in section 7.2 along with observables I^c and I^s in section 7.3 from both proton and π^0 recoil frames. Comparing measurements with PWA predictions gives an insight into the accuracy of the most recent fits where any discrepancy suggests the values of resonance-decay couplings could be improved.

Fits to the angular distribution of the single π^0 profile function $\check{\Sigma}$ have been carried out to determine with maximum orbital angular momentum (ℓ_{max}) required to describe the measurements. The coefficients from these fits directly connect the with partial wave contributions of resonances with different angular momenta across the energy range. A brief discussion of the potential interpretations stemming from the results of the fit is presented in section 7.1.1.

Section 7.3.1 explores the coefficients of third order cosine and sine series fits to I^c and I^s observables respectively. Tracing the fit coefficients as a function of energy provides information that can help determine the varying contribution of different order partial waves.

Finally, the estimated systematic errors on the measurements are considered in section 7.4.

7.1 Σ - Single π^0

The Σ polarisation observable has been measured to high precision as a function of both W_{cm} and $\cos\theta_{cm}$. A previous analysis using this data was presented by Howdle in his PhD thesis (2012)[78]. In the present analysis the coverage and quality of the measurements have been improved by conducting ${}_s\mathcal{P}lot$ event weighting and by requiring the detection of only the two photons from the π^0 decay. These results have been published and can be found in reference [108].

Figures 7.1 and 7.2 show the measured values of Σ, binned by tagger channel energy and 18 equal polar bins $-0.985 < \cos\theta < 0.906$ ($25 < \theta < 170$) counting a total of 1403 measurements. Alongside the data presented here are the previously published measurements and partial wave predictions from MAID (*MAID2007*[34]), SAID (*PR15*[66]), and Bonn-Gatchina (*BG2014-2*[56]).

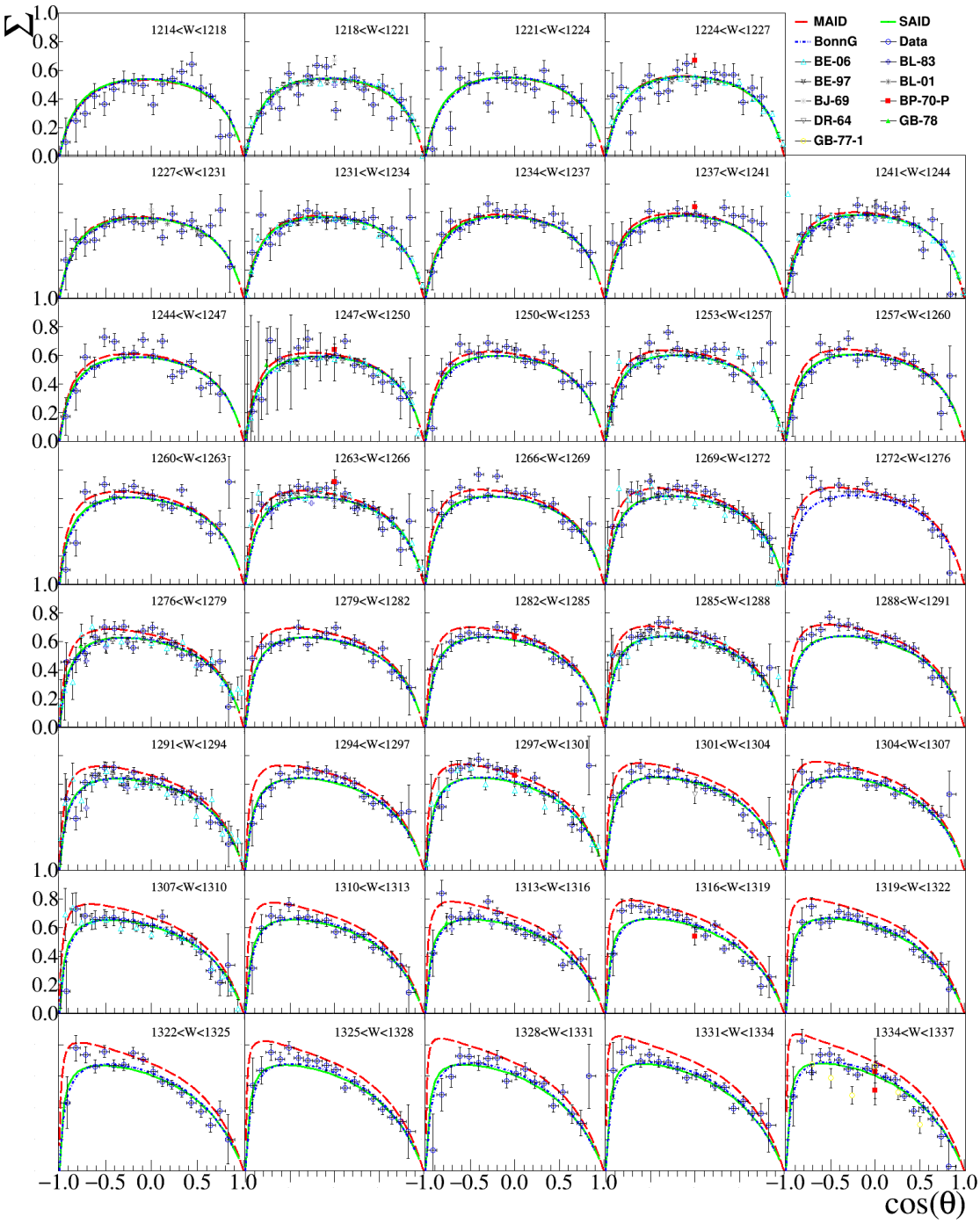

Figure 7.1: Photon asymmetry Σ as a function of $\cos\theta_{cm}$ across center-of-mass energy range 1214<W<1337 MeV. The W_{cm} range for each plot is shown in the top right. The legend shows the data measured for this work as open circles (blue), predictions from PWAs (MAID [109], SAID [110], Bonn-Gatchina [68]) as coloured lines and data from previous experiments (Previous Data: BE-06[51]BL-83[111]BE-97[46]BL-01[112]BJ-69[113]BP-70-P[114]DR-64[43]GB-78[115]GB-77-1[116]) as points, taken from the SAID database [67].

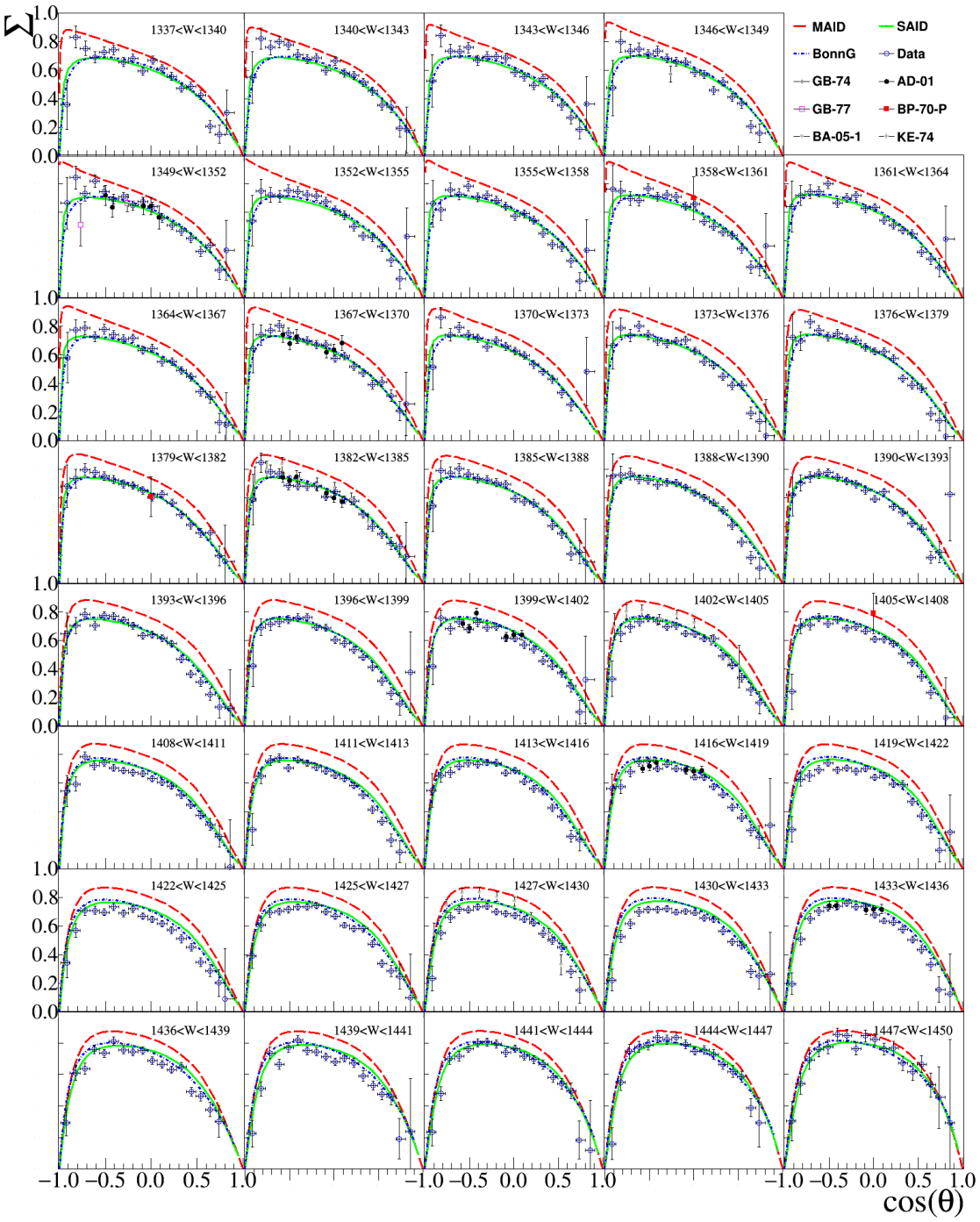

Figure 7.2: Photon asymmetry Σ as a function of $\cos\theta_{cm}$ across center-of-mass energy range 1337<W<1450 MeV. The W_{cm} range for each plot is shown in the top right. The legend shows the data measured for this work as open circles (blue), predictions from PWAs (MAID [109], SAID [110], Bonn-Gatchina [68]) as coloured lines and data from previous experiments (Previous Data: GB-74[117]AD-01[48]GB-77[116]BP-70-P[114]BA-05-1[47]KE-74[118]) as points, taken from the SAID database [67].

In general the measurements presented are in very good agreement with the latest predictions of SAID and Bonn-Gatchina; this is expected as the partial waves have previously been well constrained by measurements at the energies either side of this analysis. The predictions of the MAID group have not been updated in recent years and so did not have access to the more recent polarisation observable measurements.

These results have helped to consolidate the predicted values across the full range of kinematics measured with a slight deviation around W_{cm}=1430 MeV.

7.1.1 Orbital angular momentum fits

An ℓ_{max}-fit moment analysis was carried out on the Σ measurements, this provides an estimate for the maximum angular momentum (ℓ) required to describe the measurements. The procedure is outlined in reference [119] and is similar to work carried out in reference [120].

In order to relate the polarisation observable Σ to reaction amplitudes, the profile function $\check{\Sigma}$ as a function of θ is needed, this is the product of dimensionless Σ and the unpolarised differential cross section σ_0,

$$\check{\Sigma}\left(W,\theta\right) = \Sigma\left(W,\theta\right) * \sigma_0\left(W,\theta\right). \tag{7.1}$$

The $\check{\Sigma}$ values are calculated using the Σ measurements from this analysis along with differential cross section measurements taken from the recent analysis by Adlarson *et al.*[66]. The values can be described as an associated Legendre polynomial series (From equations 2.5 - 2.8) given by,

$$\check{\Sigma}\left(W,\theta\right) = \frac{q}{k}\sum_{k=2}^{2\ell_{max}} a_k^{\Sigma}\left(W\right) P_k^2\left(\cos\theta\right), \tag{7.2}$$

where q and k are respectively the 3-momentum moduli of the reaction γ and produced π^0, meaning $\frac{q}{k}$ is a Lorentz invariant 2-body phase space factor, a_k^{Σ} are the

coefficients of associated Legendre polynomials $P_k^2(\cos\theta)$, the forms of which are given in equations 7.3-7.7. The coefficients and truncation of this series provide information as to the dominant Legendre contributions, along with other profile functions this can be used to confine the contributions of the electric and magnetic multipole coefficients describing resonances.

The associated Legendre polynomial convention used here is give by,

$$P_2^2(\cos\theta) = 3\left(1-(\cos\theta)^2\right) \tag{7.3}$$

$$P_3^2(\cos\theta) = 15\left(1-(\cos\theta)^2\right)\cos\theta \tag{7.4}$$

$$P_4^2(\cos\theta) = \frac{15}{2}\left(1-(\cos\theta)^2\right)\left(-1+7(\cos\theta)^2\right) \tag{7.5}$$

$$P_5^2(\cos\theta) = \frac{105}{2}\left(1-(\cos\theta)^2\right)\left(-\cos\theta+3(\cos\theta)^3\right) \tag{7.6}$$

$$P_6^2(\cos\theta) = \frac{105}{8}\left(1-(\cos\theta)^2\right)\left(1-18(\cos\theta)^2+33(\cos\theta)^4\right) \tag{7.7}$$

With ℓ_{max} functions up to the 3rd order,

$\ell_{max} = 1$:

$$\check{\Sigma}(W,\theta) = \frac{q}{k}a_2^{\Sigma}(W)\,P_2^2(\cos\theta) \tag{7.8}$$

$\ell_{max} = 2$:

$$\check{\Sigma}(W,\theta) = \frac{q}{k}\left(a_2^{\Sigma}(W)\,P_2^2(\cos\theta)+a_3^{\Sigma}(W)\,P_3^2(\cos\theta)+a_4^{\Sigma}(W)\,P_4^2(\cos\theta)\right), \tag{7.9}$$

$\ell_{max} = 3$:

$$\begin{aligned}\check{\Sigma}(W,\theta) = \frac{q}{k}\Big(&a_2^{\Sigma}(W)\,P_2^2(\cos\theta)+a_3^{\Sigma}(W)\,P_3^2(\cos\theta)+a_4^{\Sigma}(W)\,P_4^2(\cos\theta)\\ &+a_5^{\Sigma}(W)\,P_5^2(\cos\theta)+a_6^{\Sigma}(W)\,P_6^2(\cos\theta)\Big),\end{aligned} \tag{7.10}$$

These functions are fitted using a χ^2 minimisation to values of $\check{\Sigma}(\theta)$, with the coefficients a_k^{Σ} as free parameters for each W_{cm} bin. Four energy bins showing the fit results calculated in Bonn[121] are shown as examples in figure 7.3.

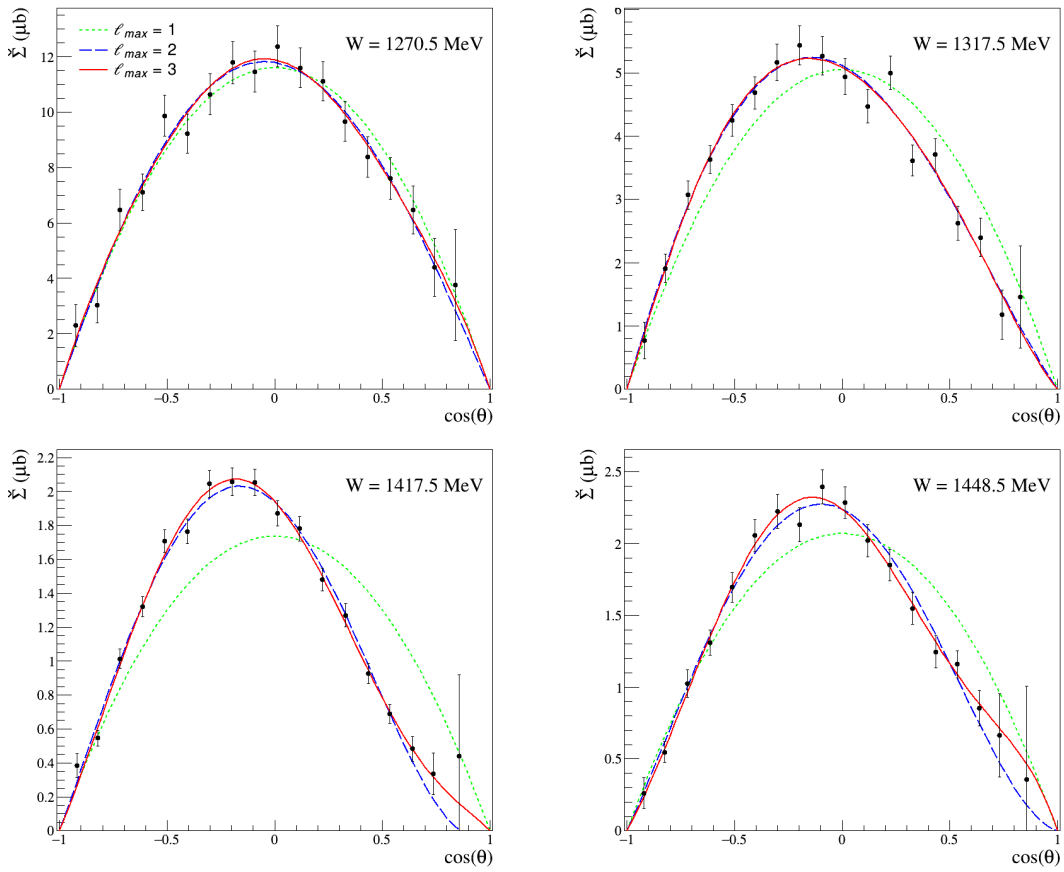

Figure 7.3: Example plots showing the truncated Legendre polynomial fit for ℓ_{max}=(1,2,3). At $W = 1270.5$ MeV $\ell_{max} = 1$ is sufficient to describe the data whereas at $W = 1417.5$ truncation at $\ell_{max} = 1$ no longer provides a valid fit.

The quality of the ℓ_{max} fit, described by χ^2/ndf, is shown as a function of W in figure 7.4. On average the fit to $\check{\Sigma}$ will have a lower χ^2/ndf for higher order ℓ_{max}. Where a significant difference in the χ^2/ndf between the different fits is observed, the lower ℓ_{max} is clearly no longer sufficient to describe the $\check{\Sigma}$ measurements. The χ^2/ndf of the fit is dependent on the statistics, which is not shown in the figure. Low statistics can be fitted more easily with any function, such that a convergence in the χ^2/ndf does not necessarily mean that higher order angular momenta are not physically present, just the measurements aren't accurate enough to be conclusive.

Each coefficient of the fit is described by a sum of contributions from resonances

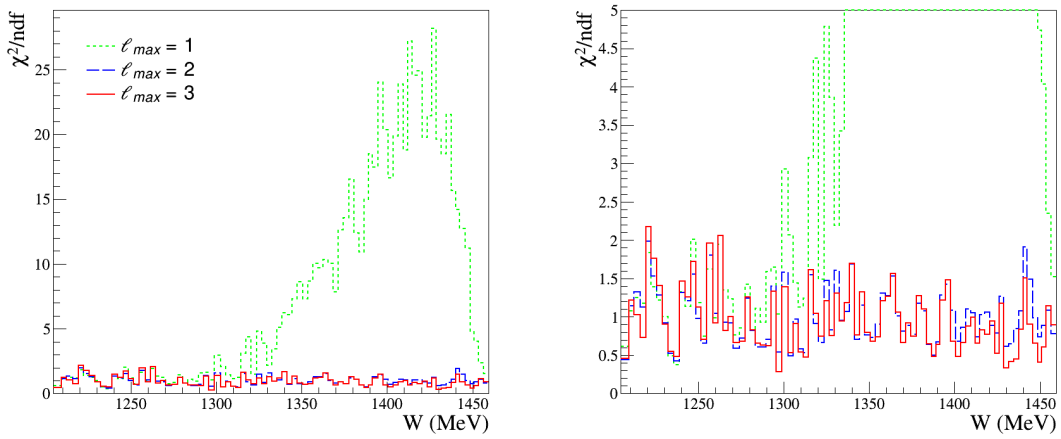

Figure 7.4: χ^2 of the Legendre polynomial fits to $\cos\theta$ across a range of W for truncation $\ell_{max} = (1, 2, 3)$. Left - Full range of values shown. Right - Enhanced around $\ell_{max} = (2, 3)$. At around $W = 1300$ MeV $\ell_{max} = 1$ becomes insufficient to describe the $\check{\Sigma}$ measurements. At the top end there is a small divergence between $\ell_{max} = 2$) and $\ell_{max} = 3$ suggesting higher resonances are becoming more prevalent.

and interference terms. When taking angular momenta terms up to L=3, the function has contributions from S-, P-, D- and F-Waves, where each coefficient can be described as,

$$a_2^\Sigma = \langle S, D\rangle + \langle P, P\rangle + \langle P, F\rangle + \langle D, D\rangle + \langle F, F\rangle\,, \tag{7.11}$$

$$a_3^\Sigma = \langle S, F\rangle + \langle P, D\rangle + \langle D, F\rangle\,, \tag{7.12}$$

$$a_4^\Sigma = \langle P, F\rangle + \langle D, D\rangle + \langle F, F\rangle\,, \tag{7.13}$$

$$a_5^\Sigma = \langle D, F\rangle\,, \tag{7.14}$$

$$a_6^\Sigma = \langle F, F\rangle\,. \tag{7.15}$$

This shorthand notation $\langle -, -\rangle$ denotes all interference terms among multipoles of definite ℓ-quantum-numbers. For instance, $\langle S, D\rangle$ denotes a sum,

$$\langle S, D\rangle = \sum_{\mathcal{M},\mathcal{M}'=\{E,M\}} \sum_{p,p'=\{\pm\}} c_{p,p'}^{\mathcal{M},\mathcal{M}'} \mathcal{M}_{0p}^* \mathcal{M}_{2p'}', \tag{7.16}$$

where $\mathcal{M}$ are the electric and magnetic coupling constants described in equation 2.5 and c are coefficients.

Individual coefficients from the fit can be used to provide a clearer indication of the energies at which different Legendre polynomials contribute more strongly and how the measurements compare to predicted values. Coefficients of the $\ell_{max} = 3$ fit to the measurements are shown alongside predicted values from truncated Bonn-Gatchina PWA fits in figure 7.5.

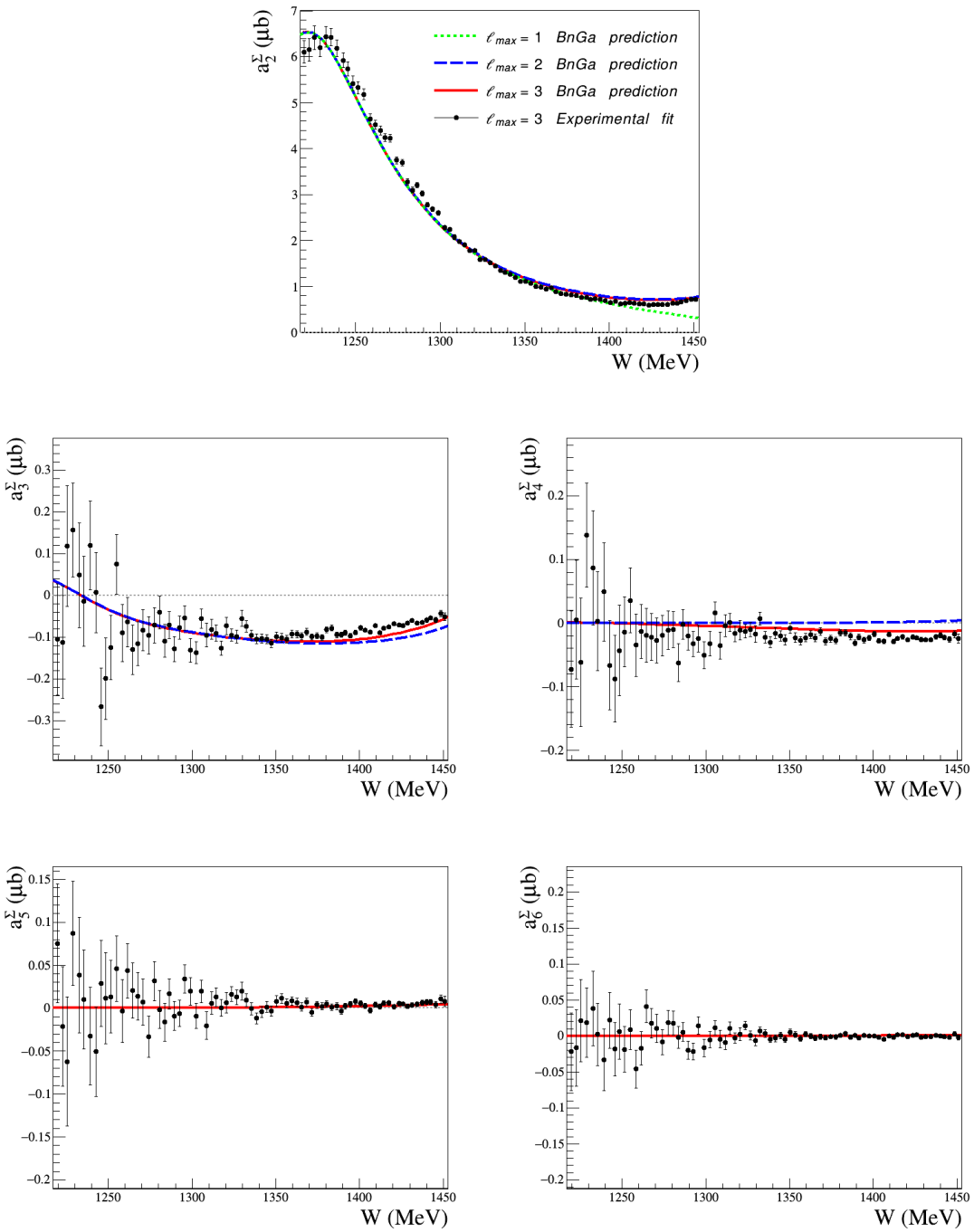

Figure 7.5: Values of the five Legendre coefficients as a function of W used to fit $\check{\Sigma}$ when $\ell_{max} = 3$. Lines are predictions from Bonn-Gatchina *BG2014-2*[56] fit multipoles truncated at different order ℓ as in the legend.

From the plot of χ^2/ndf a divergence between ℓ_{max} fits are only observed above $W = 1300$. By looking at the individual coefficients a_3^Σ and a_4^Σ, non-zero values from as low as $W = 1250$ have been measured, this can be accounted for by the

relatively large statistical uncertainty in the measurements across this energy range. The additional coefficients, a_4^Σ and a_5^Σ, present when increasing $\ell_{max} = 2$ to $\ell_{max} = 3$, appear to be consistent with zero across most of the W range. An expansion around zero, shown in figure 7.6, displays non-zero values for a_4^Σ in line with the Bonn-Gatchina predictions whereas a_5^Σ shows no significant trend.

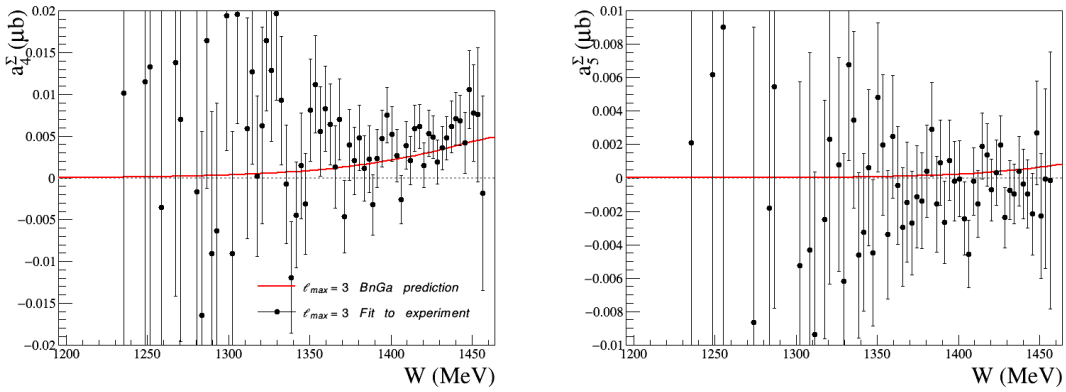

Figure 7.6: Values for the Legendre coefficients present when extended from $\ell_{max} = 2$ to $\ell_{max} = 3$. a_4^Σ appears to increase with the Bonn-Gatchina predictions however only having a small effect on the form of $\check{\Sigma}$. a_5^Σ however shows no statistically significant deviation from zero.

Interpretation

The recent Bonn-Gatchina predictions are in good agreement with the measured Legendre coefficients, this is encouraging as a support of the quality of the measurements and the predictive power of the Bonn-Gatchina multipole calculations.

Using equations 7.11-7.15 we can speculate about the contributions of different resonances across the energy range. The coefficients a_5^Σ and a_6^Σ are consistent with zero across the energy range, suggesting that there is very little F-wave contribution in line with there being no known 4-star F-resonance in reach of the energy range. The small contributions however turn out to be not entirely unimportant as increasing the partial wave expansion of the Bonn-Gatchina predictions to include the F-Waves shows a significant improvement in the description of the measurements of a_3^Σ and a_4^Σ.

The multipole compositions of a_3^Σ and a_4^Σ contain interference terms between F-waves

and partial waves of lower order angular momentum, these account for the improvement of the PWA prediction between $\ell_{max} = 2$ and $\ell_{max} = 3$. The a_3^Σ coefficient prediction is improved when accounting for the small contribution from the F-wave through its interference with S- and D-waves respectively from the $N(1520)\frac{3}{2}^-$ and $N(1535)\frac{1}{2}^-$ resonances within the reach of the data, evidence of the D-F interference can also be seen in the expanded axis of the a_3^Σ coefficient. The same interpretation can be made for the improvement in the a_4^Σ coefficient prediction where the small F-wave has a non-insignificant interference with the P-wave from the $N(1440)\frac{1}{2}^+$ resonance.

The measurements of Σ in this analysis show dominant contributions up to $\ell_{max} = 2$ and are in good agreement with the Bonn-Gatchina model predictions dominated by the lowest order partial waves. An improvement in the prediction is seen when expanding to $\ell_{max} = 3$ meaning there are small contributions through interference with F-wave resonances. The precision of the measurements is good enough to help further constrain higher order partial waves and interference terms beyond the energy reach of this experiment for future PWA models.

7.2 Σ_p and Σ_π - Double π^0

Measurements of Σ_p and Σ_π in double π^0 photoproduction can be generated using two methods, as discussed in section 2.4.3. Firstly, by directly fitting the ϕ distribution of a $\cos\theta_{cm}$-W bin or secondly by taking the first term of the cosine series fit to I^c as a function of Φ^* for that bin. Both methods have advantages which are outlined below.

The measurements of I^c and the cosine series fit are shown in section 7.3.

Fitting the ϕ distribution directly allows a finer W and $\cos\theta_{cm}$ binning in the values of Σ to be measured due to the higher statistics. By using the fit to I^c on the other hand, systematic detector acceptance effects which may vary over different values of Φ^* are accounted for. Effects of detector acceptance are expected to be small due to the four γ final state allowing a wide range of final state particle kinematics.

Values for Σ are presented here using the more finely binned integration over Φ^* with both proton and π^0 recoil frames shown respectively in figures 7.7 and 7.8.

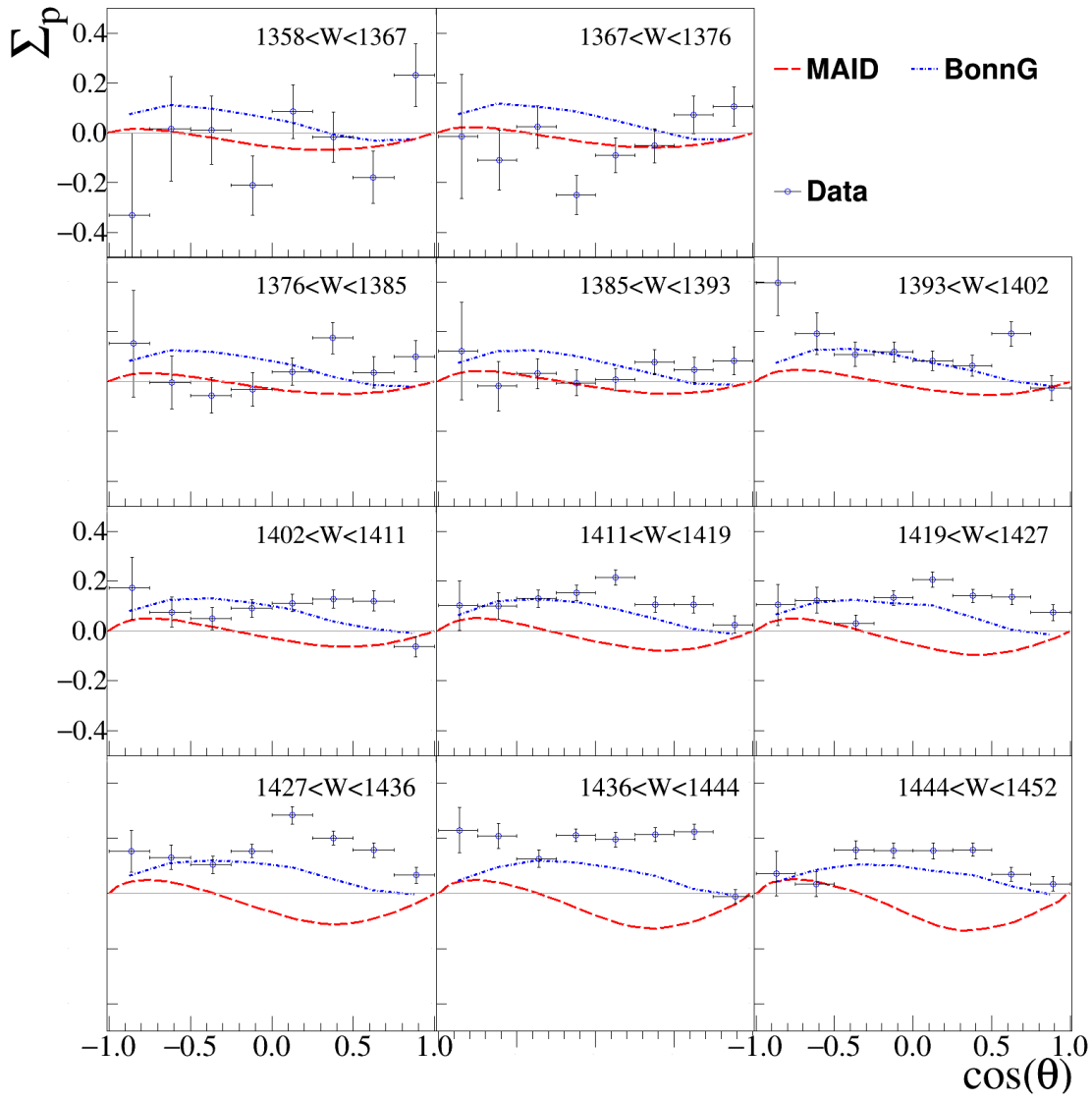

Figure 7.7: Double π^0 photon asymmetry Σ_p as a function of $\cos\theta_{cm}$ across center of mass energy range 1358<W<1452 MeV in the proton recoil frame. The W_{cm} range for each plot is shown in the top right. The legend shows the data measured for this work as open circles(blue) and predictions from PWAs (MAID[31], Bonn-Gatchina[42]) are plotted as coloured lines. No previous measurements have been made in this energy range.

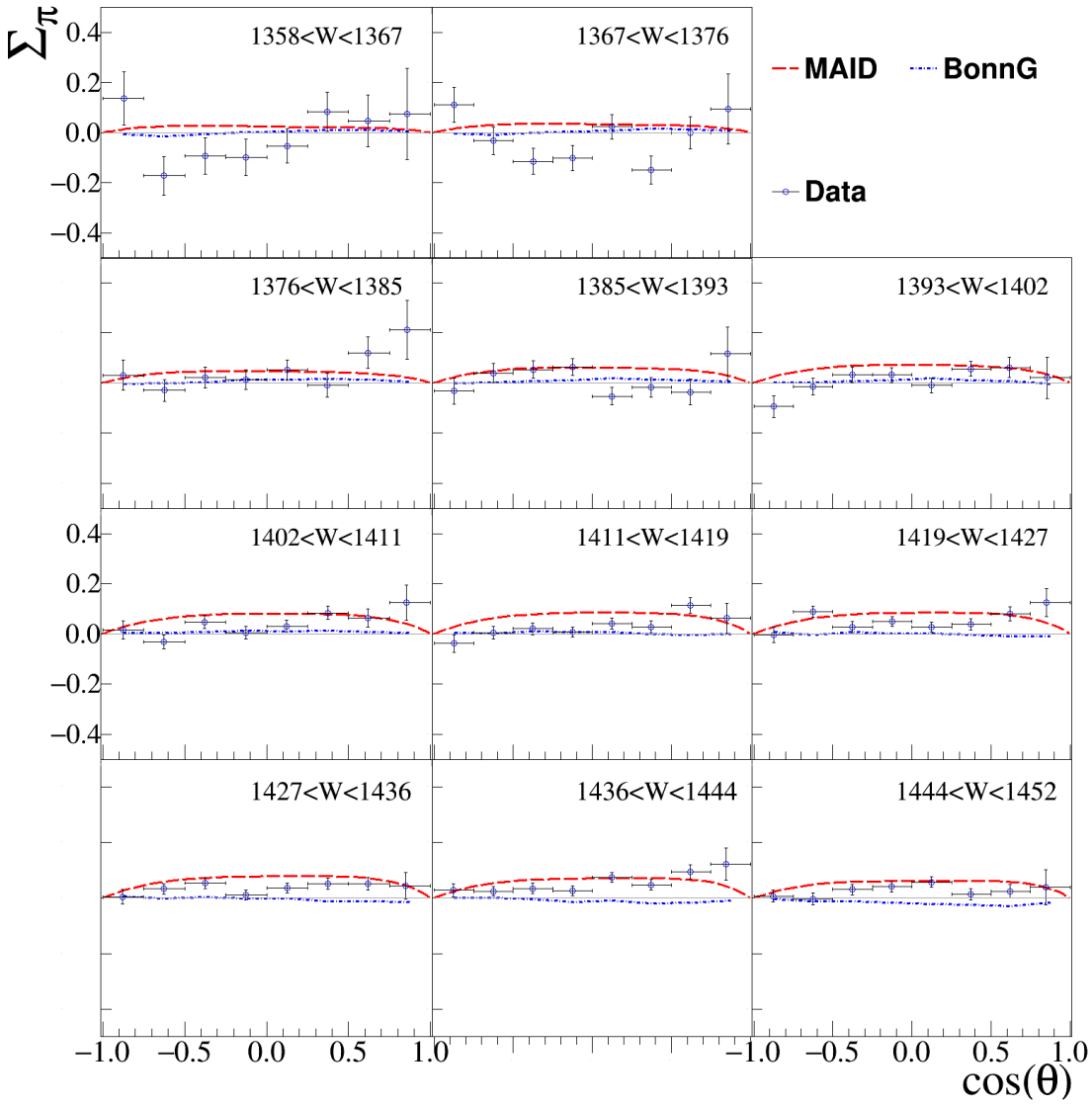

Figure 7.8: Double π^0 photon asymmetry Σ_π as a function of $\cos\theta_{cm}$ across center of mass energy range 1358<W<1452 MeV in the π^0 frame. The W_{cm} range for each plot is shown in the top right. The legend shows the data measured for this work as open circles(blue) and predictions from PWAs (MAID[31], Bonn-Gatchina[42]) are plotted as coloured lines. No previous measurements have been made in this energy range.

A comparison between values of Σ and associated errors, calculated using the two different methods, are presented in figures 7.9 and 7.10 for proton and π^0 recoil frames respectively.

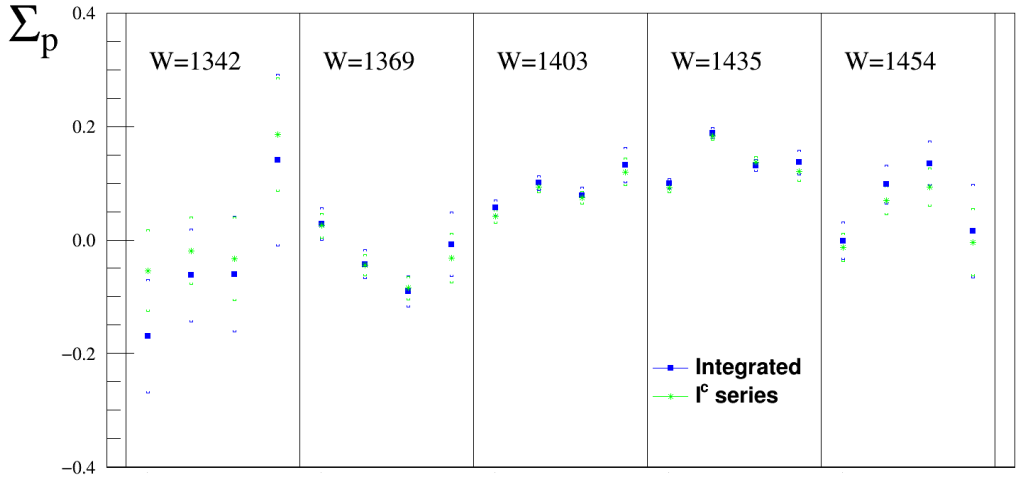

Figure 7.9: Values for Σ calculated from a fit to I^c values (green) and directly fitting the integrated $\cos 2\phi$ of the azimuthal angle (blue). Taken in the proton recoil frame.

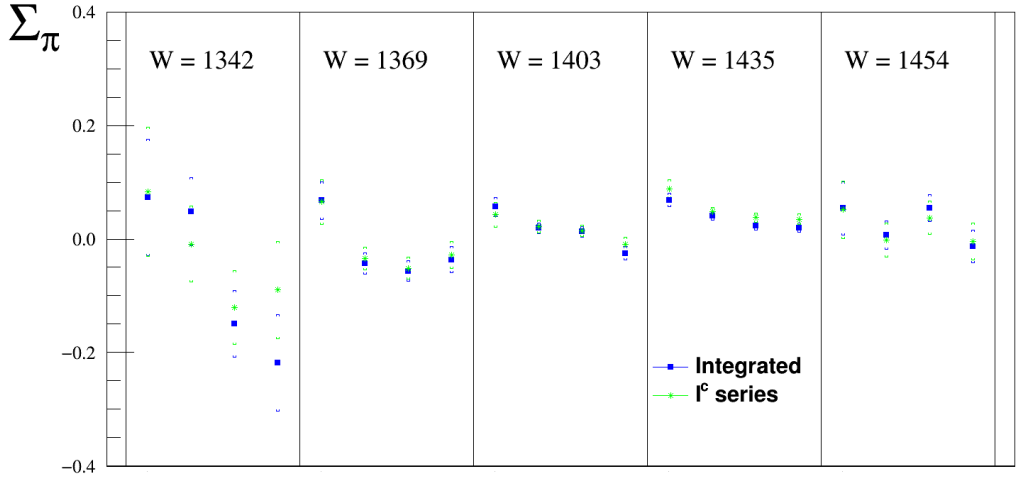

Figure 7.10: Values for Σ calculated from a fit to I^c values (green) and directly fitting the integrated $\cos 2\phi$ of the azimuthal angle (blue). Taken in the π^0 recoil frame.

The agreement between of the two measurements of Σ is encouraging, there are no large systematic differences between the two methods suggesting that any systematic effects from detector acceptances are very small.

7.3 I^s and I^c - Double π^0

Measurements of I^s and I^c have been made across a range of W, $\cos\theta$ and Φ^* in both proton and π^0 recoil frames. As described in section 2.4.3, symmetry conditions in the Φ^* angle mean that by using the mirror operator on the measurements, an equally valid set of measurements can be produced. The mean values of the original and mirror measurements of I^c and I^s have been fitted respectively with third order cosine and sine series across the Φ^* range.

Figures 7.11,7.12,7.13 and 7.14 show measurements of the observables, the fit function and PWA predictions from Bonn-Gatchina (*BG2014-2*[56]).

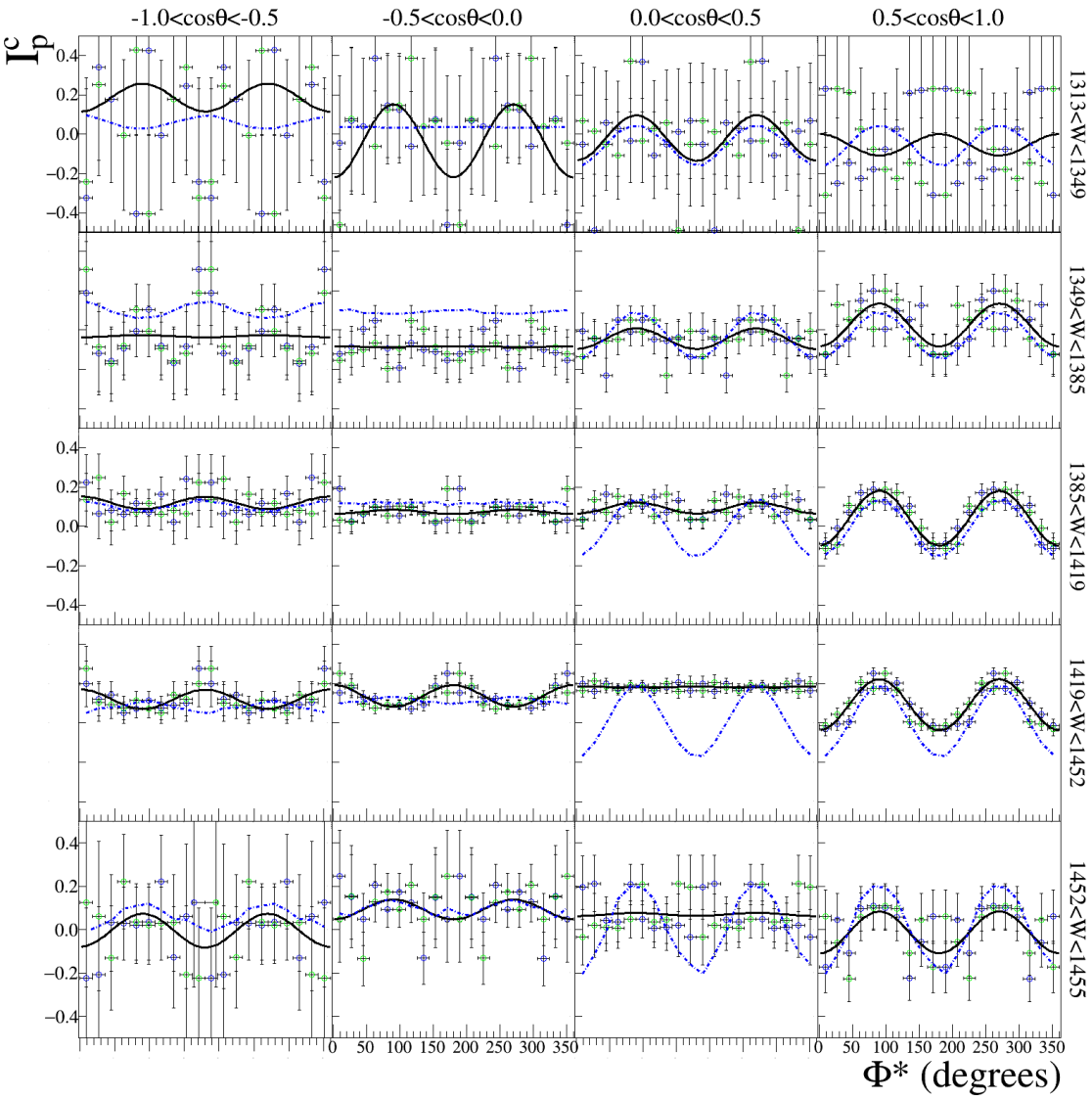

Figure 7.11: Polarisation observable I^c as a function of Φ^* in four equal $\cos\theta$ bins across center of mass energy range $1313 < W < 1455$ MeV in the proton recoil frame. The W_{cm} range for each plot is shown on the right of the row and the $\cos\theta$ range is shown at the top of the columns. Measurements are shown as open circles (blue), mirror opperated measurements are shown as open circles (green). Lines are a third order cosine series fitted to the mean of the two data sets (black) and Bonn-Gatchina predictions (dashed blue).

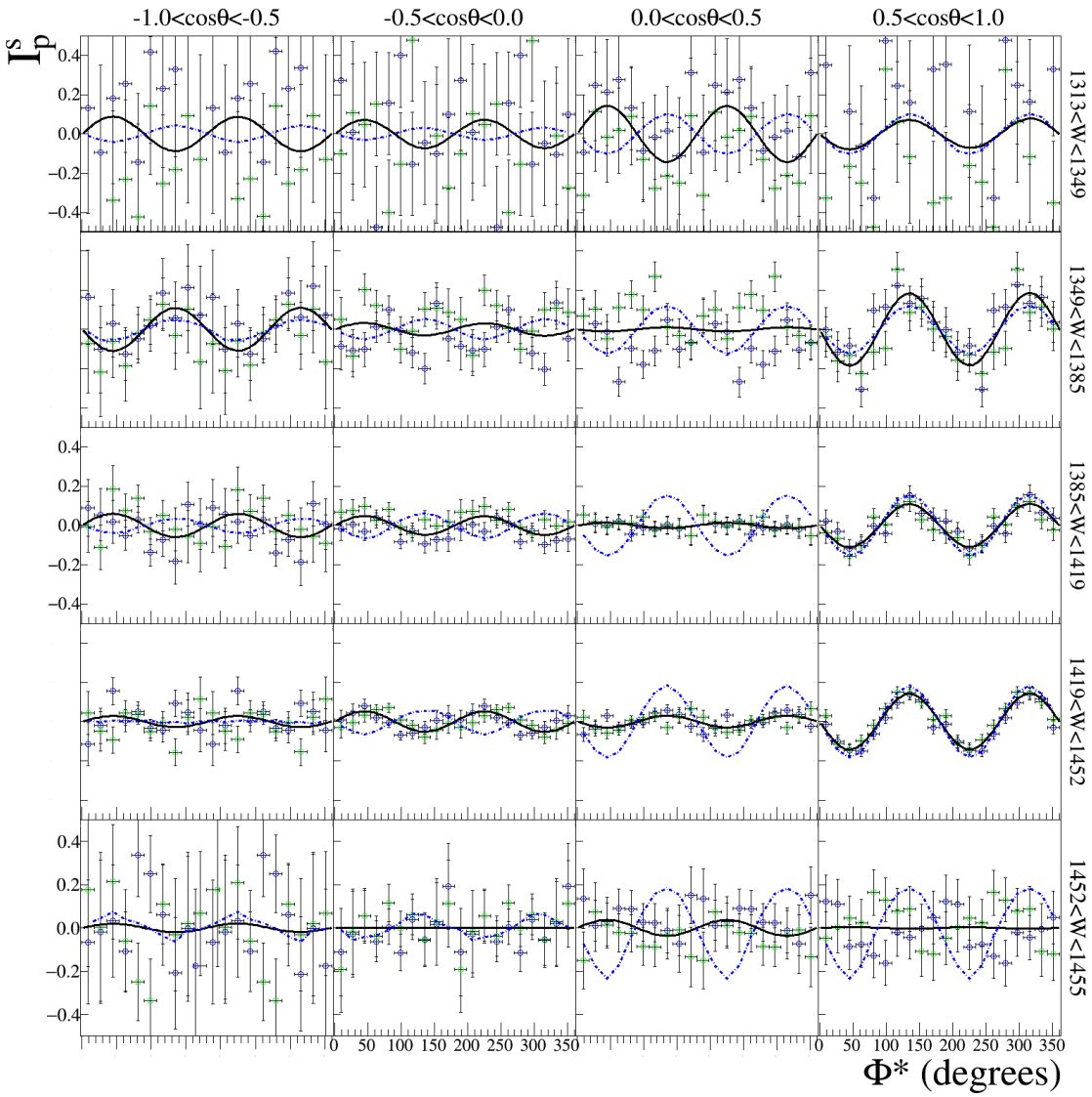

Figure 7.12: Polarisation observable I^s as a function of Φ^* in four equal $\cos\theta$ bins across center of mass energy range $1313 < W < 1455$ MeV in the proton recoil frame. The W_{cm} range for each plot is shown on the right of the row and the $\cos\theta$ range is shown at the top of the columns. Measurements are shown as open circles (blue), mirror opperated measurements are shown as open circles (green). Lines are a third order sine series fitted to the mean of the two data sets (black) and Bonn-Gatchina predictions (dashed blue).

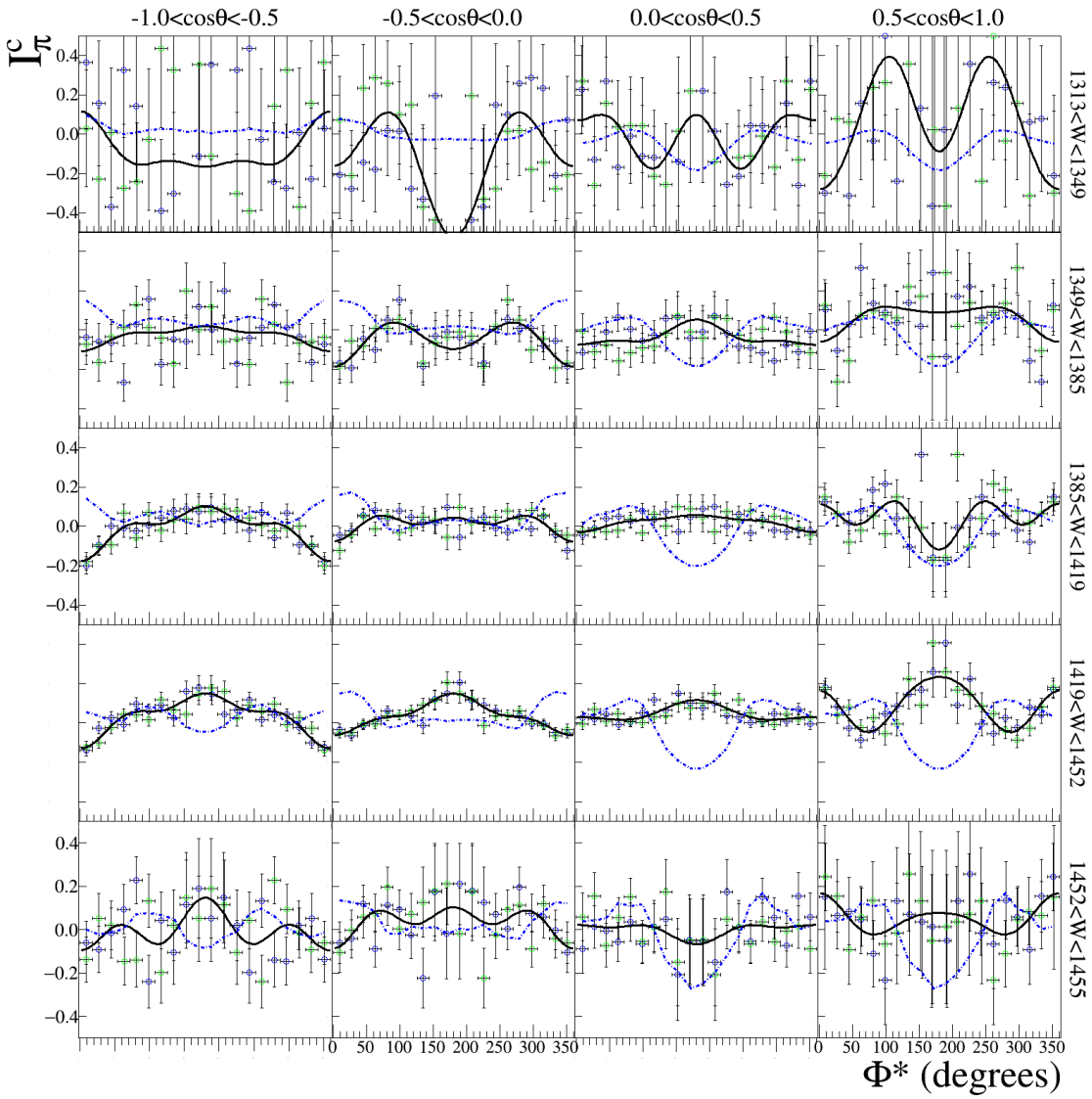

Figure 7.13: Polarisation observable I^c as a function of Φ^* in four equal $\cos\theta$ bins across center of mass energy range $1313 < W < 1455$ MeV in the π^0 recoil frame. The W_{cm} range for each plot is shown on the right of the row and the $\cos\theta$ range is shown at the top of the columns. Measurements are shown as open circles (blue), mirror opperated measurements are shown as open circles (green). Lines are a third order cosine series fitted to the mean of the two data sets (black) and Bonn-Gatchina predictions (dashed blue).

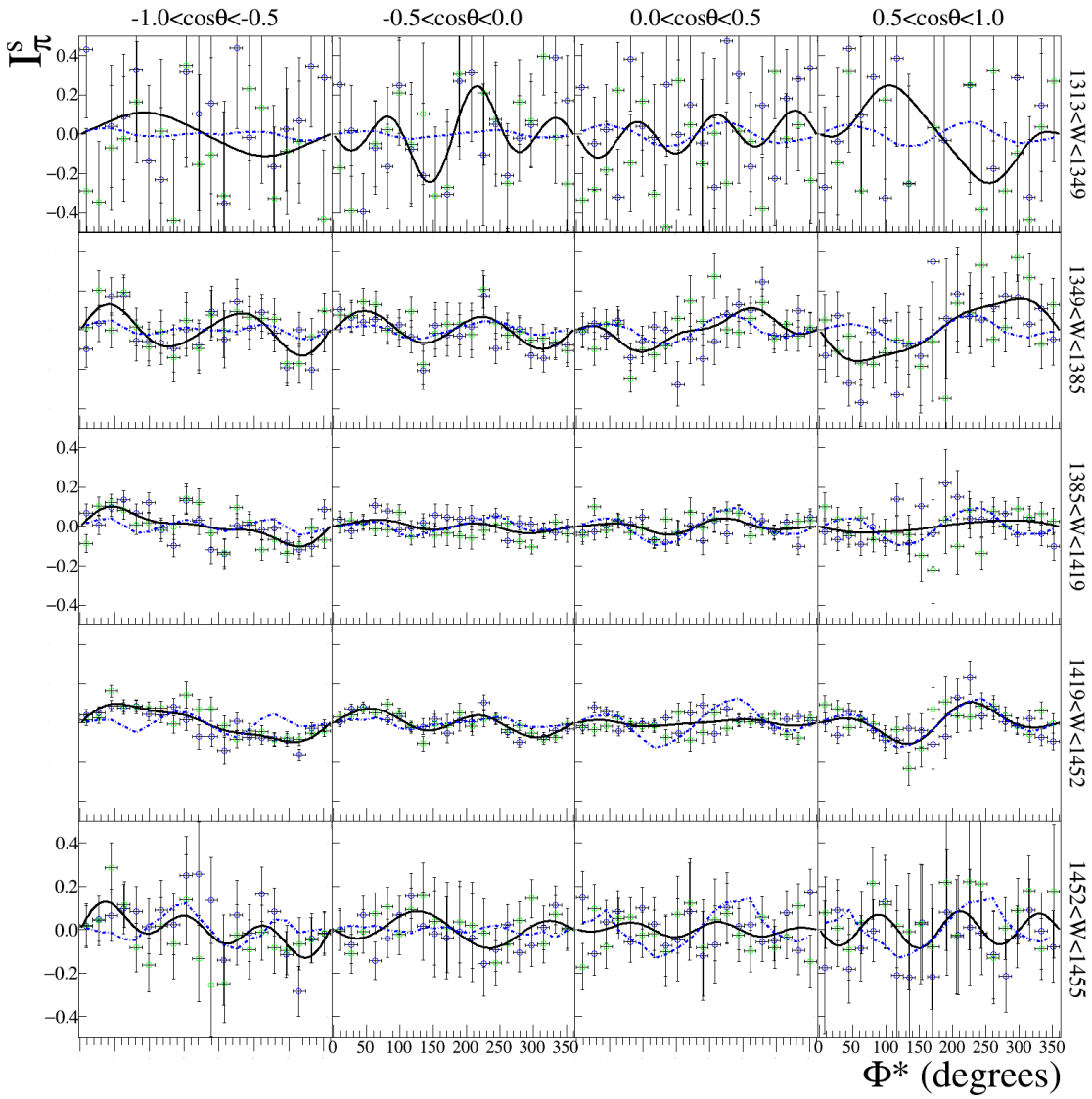

Figure 7.14: Polarisation observable I^s as a function of Φ^* in four equal $\cos\theta$ bins across center of mass energy range $1313 < W < 1455$ MeV in the π^0 recoil frame. The W_{cm} range for each plot is shown on the right of the row and the $\cos\theta$ range is shown at the top of the columns. Measurements are shown as open circles (blue), mirror opperated measurements are shown as open circles (green). Lines are a third order sine series fitted to the mean of the two data sets (black) and Bonn-Gatchina predictions (dashed blue).

7.3.1 Fit Coefficients

The coefficients of the third order cosine and sine series used to fit the values of I^c and I^s in both recoil frames are shown in figures 7.15, 7.16, 7.17 and 7.18, where the coefficients follow the labelling given by equations 2.16 and 2.17.

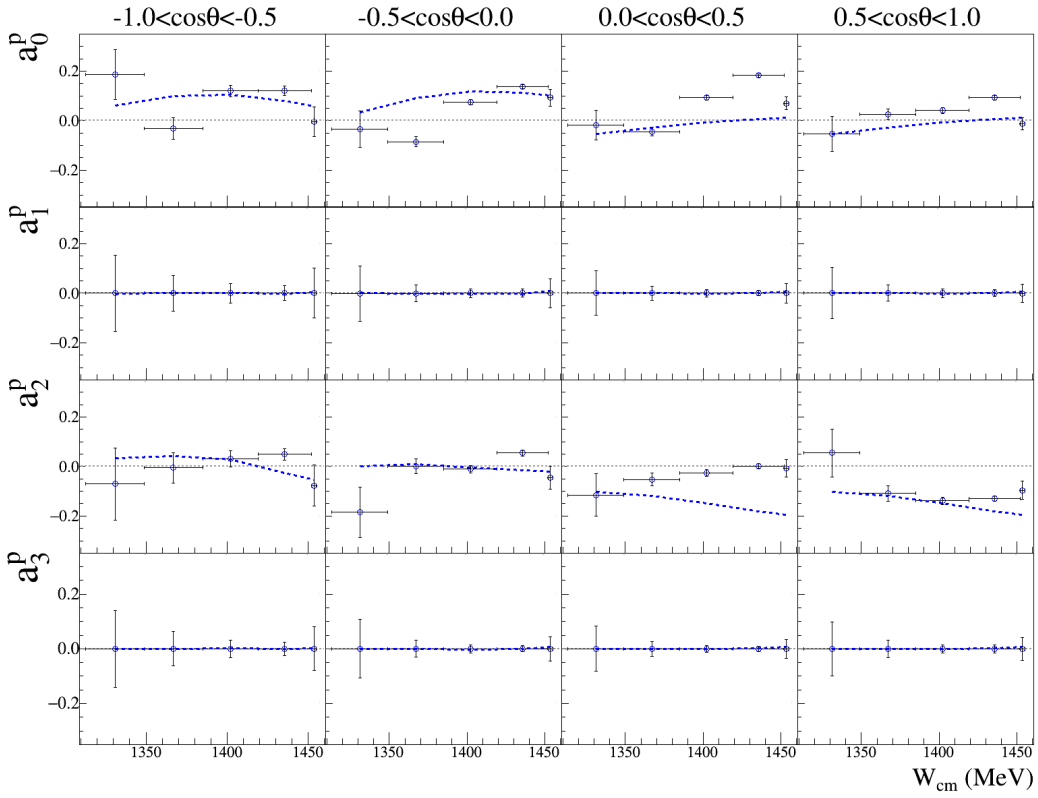

Figure 7.15: Coefficients of the 3rd order cosine series fit to the Φ^* dependence of I^c in the proton recoil frame. The indistinguishable nature of the π^0s restrict the odd coefficients a_1^p and a_3^p to 0. Dashed blue line - Bonn-Gatchina predictions.

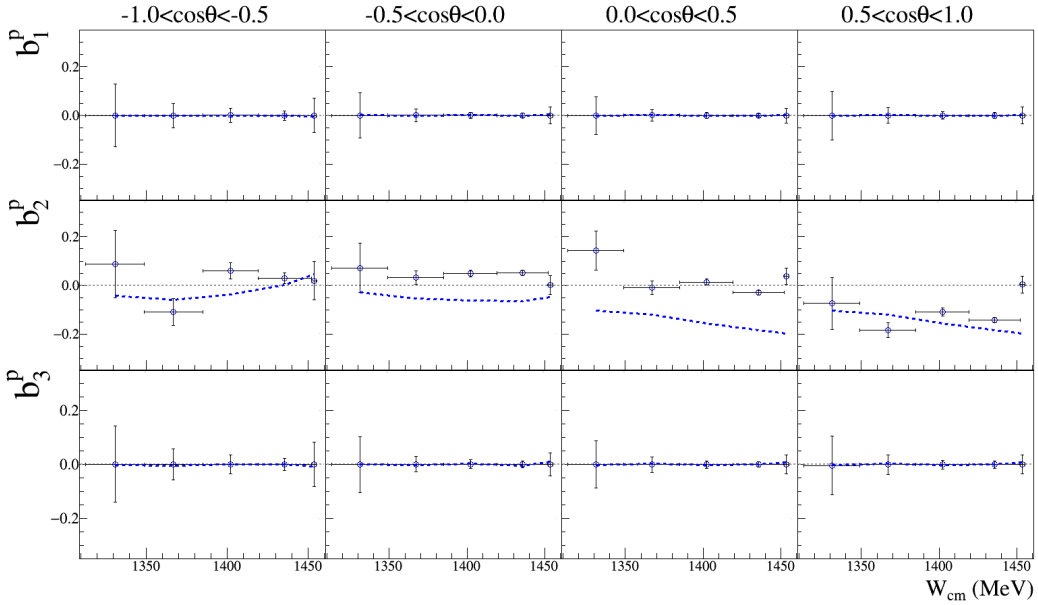

Figure 7.16: Coefficients of the 3rd order sine series fit to the Φ^* dependence of I^s in the proton recoil frame. The indistinguishable nature of the π^0s restrict the odd coefficients b_1^p and b_3^p to 0. Dashed blue line - Bonn-Gatchina predictions.

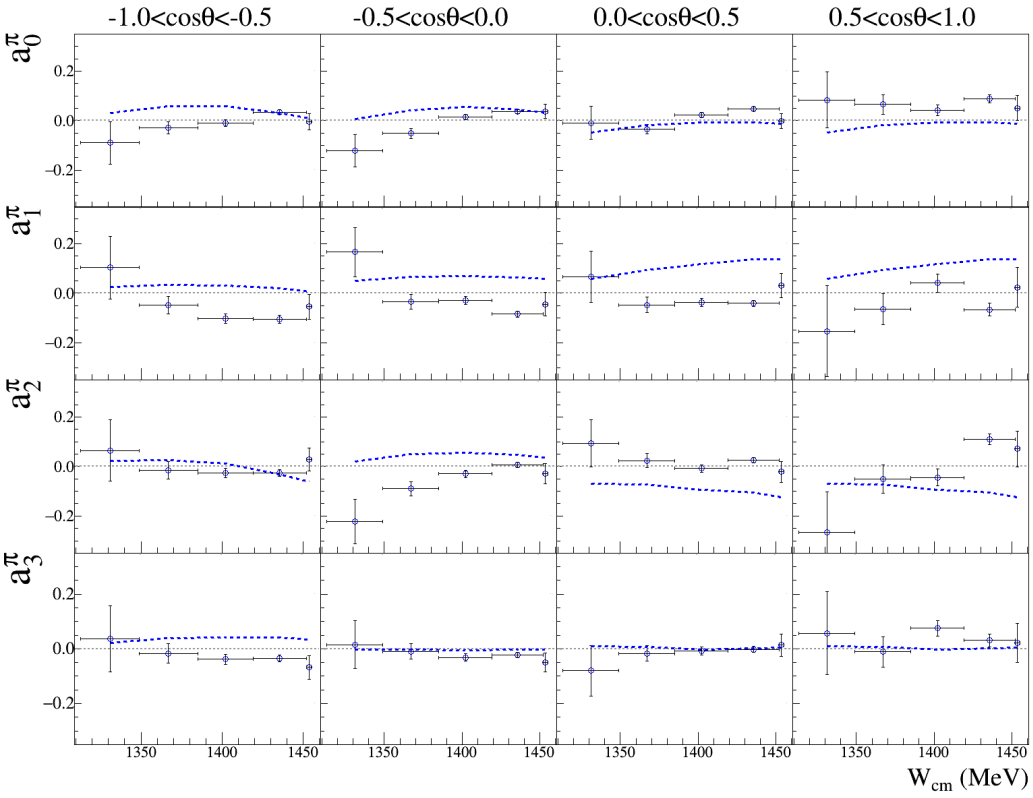

Figure 7.17: Coefficients of the 3rd order sine series fit to the Φ^* dependence of I^c in the π^0 recoil frame. Dashed blue line - Bonn-Gatchina predictions.

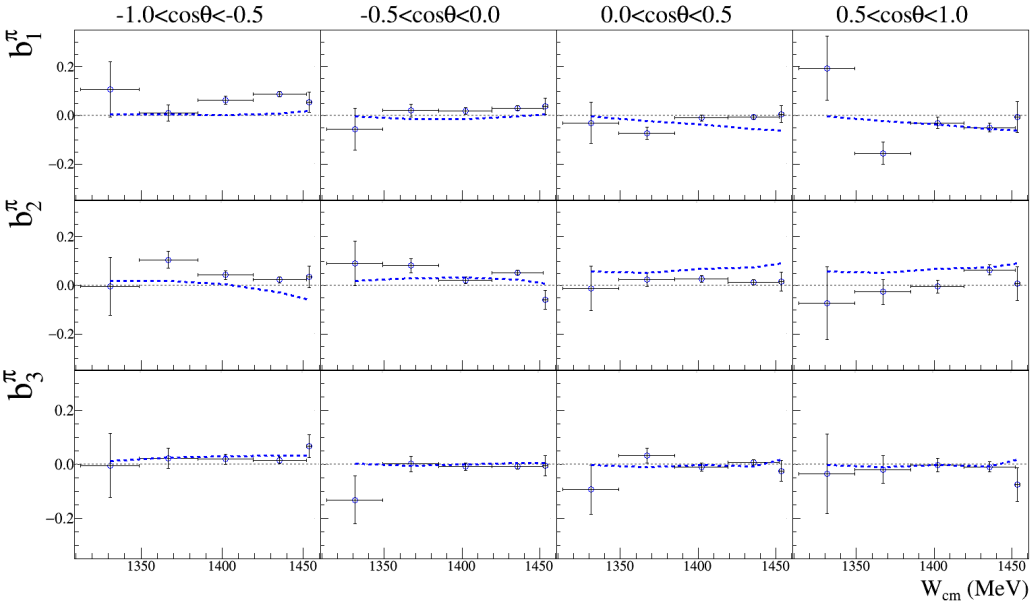

Figure 7.18: Coefficients of the 3rd order sine series fit to the Φ^* dependence of I^s in the π^0 recoil frame. Dashed blue line - Bonn-Gatchina predictions.

Interpretation

It is unclear what effect these results will have when constraining future PWA fits. From comparisons between the measurements and the Bonn-Gatchina PWA predictions there is obviously scope for improvement to current models.

The Roper resonance, N(1440), is covered by the energy range of these measurements and its properties are currently poorly constrained. The PDG database quotes a large uncertainty in the branching ratios in the decay of the Roper; the N(1440)$\rightarrow$ $\Delta(1232)\pi$ branching ratio is estimated as 15-30%, with the N(1440)$\rightarrow$ σp branching ratio as 13-20%. The measurement of Σ_p has a larger value than Σ_π on the Roper peak, suggesting that the intermediate σ decay may be the dominant process over the $\Delta(1232)$ process.

Only once the measurements have been included in a full PWA fit can the full implications of these results be interpreted.

7.4 Systematic Uncertainties

Two main sources of systematic uncertainties in the results have been investigated, the degree of photon linear polarisation (see section 5.3.4) and the estimation of background contributions to the data using an ${}_s\mathcal{P}lot$ fit to the missing mass (see section 6.4.3).

The uncertainty in the calculation of the degree of polarisation through a fit to PWA predictions was estimated to be 2%. Systematic uncertainties, also inherent in the PWA predictions used in the fit, are estimated to be 2%[103] and arise from propagation of the errors in the experimental measurements which have been used to calculate the prediction. Together these two uncertainties contribute a 3% systematic uncertainty to all final measurements of polarisation observables.

The ${}_s\mathcal{P}lot$ method of measuring background contributions is estimated to propagate an average systematic uncertainty of 3% to final measurements in the π^0 channel

and 6% in the $2\pi^0$ channel. The origin of the uncertainties in this technique are discussed in section 6.4.3.

The systematic errors investigated are included with the measurements when used in the calculations of theorists.

Chapter 8

Conclusions

High statistics measurements of linear polarisation observables in π^0 and $2\pi^0$ photoproduction off the proton have been calculated. The experimental data which has been analysed was collected in the A2 hall at MAMI.

The measured values of Σ in single π^0 photoproduction are a significant improvement over previously published measurements, covering the energy range $320<E_\gamma<650$ MeV ($1214<W<1450$ MeV), improving the resolution in both centre of mass energy and $\cos\theta$. The extent of these measurements is shown in figure 8.1. The results are in good agreement with all previous measurements of Σ and support the predictions of the most recent PWA of Bonn-Gatchina and SAID. The accuracy of the results is sufficient to further constrain future PWA fits.

The profile function $\check{\Sigma}$ has been fitted with a Legendre series, which was truncated at angular momentum $\ell_{max} = 1 \rightarrow \ell_{max} = 3$. The truncation at $\ell_{max} = 2$ provided a reasonable description of the data with a small but significant improvement in the χ^2 of the $\ell_{max} = 3$ fit. This is also seen when comparing the coefficients of the fit to truncated Bonn-Gatchina predictions, suggesting there is some contribution to the values of $\check{\Sigma}$ from S and D-wave interference with F-wave resonances.

The results for the single π^0 analysis have been published and can be found in reference [108].

Measurements of the $2\pi^0$ observables Σ, I^c and I^s were made in both recoiling pro-

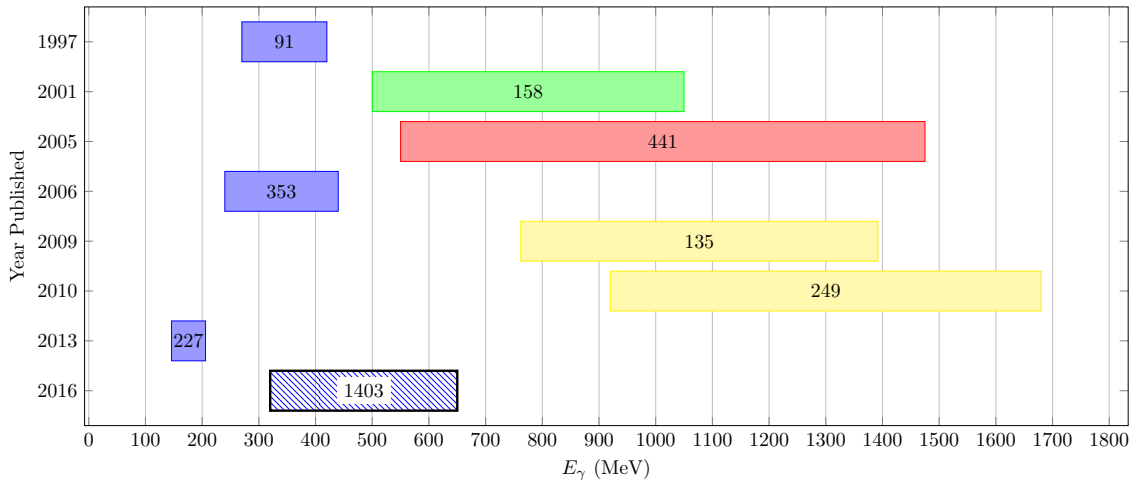

Figure 8.1: The coverage of single π^0 Σ measurements from this work are displayed as the blue hashed box compared to results from previous experiments. The number in each box is the total measurements from the experiment.

ton and recoiling π^0 frames, in an energy range with no previous measurements (1313<W<1349 MeV), the range of these measurements compared to previous experiments is shown in figure 8.2. These measurements provide information on the coupling of resonances to intermediate Δ and meson decay pathways, and are expected to significantly improve the predictive power of future $2\pi^0$ PWA fits by constraining the coupling of the $2\pi^0$ decay channels to resonances in this energy range.

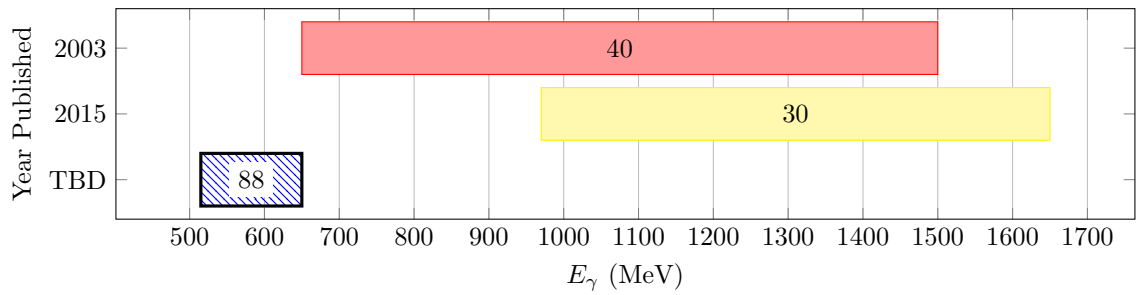

Figure 8.2: The coverage of double π^0 Σ measurements from this work are displayed as the blue hashed box compared to results from previous experiments. The number in each box is the total measurements from the experiment.

In particular, the properties of the Roper resonance, N(1440), are currently poorly constrained in the the PDG database[21]. The branching ratio for the decay N(1440)$\rightarrow$ $\Delta(1232)\pi$ is estimated as 15-30%, with the N(1440)$\rightarrow$ σp branching ratio as 13-20%, it is anticipated that the results produced for this thesis will help narrow the range of

these estimates. These measurements have been given to the Bonn-Gatchina group for inclusion in their partial wave analysis and are in the process of being written up for publication.

The measurement of the beam polarisation using the coherent Bremsstrahlung enhancement fitting method was subject to a large systematic uncertainty due to some of the technical constraints of the experiment. This was overcome by the development of a new approach where the polarisation was scaled by the ratio of measured to predicted values of Σ on the $\Delta(1232)$ peak, at which the predicted values are well founded and in good agreement. This method proved successful in providing a reliable degree of polarisation across the full coherent range, with a systematic error estimated at 2%.

The ${}_s\mathcal{P}lot$ statistical technique for disentangling event sources was successfully tested in the removal of background events from the single π^0 signal. This test provided confidence in its implementation for the $2\pi^0$ analysis where the background contributions are more complex. The use of ${}_s\mathcal{P}lot$ technique in this analysis has helped pave the way for further use and future development in the field.

A recent recoil experiment, carried out in August 2016, was run under similar conditions to the October 2008 beamtime. The new data was taken using a deuterium target with the coherent peak covering the same energy range and a new recoil polarimeter. The ${}_s\mathcal{P}lot$ techniques developed for the analysis in this thesis will be invaluable in comparing measurements of photoproduction off the quasi-free proton with those from the free proton in order to quantify the effects of Fermi motion in the deuteron. Correcting for these effects will allow measurements of, so far, unmeasured recoil polarisation observables off the neutron.

In summary, high statistics measurements of Σ have been made in single π^0 photoproduction and have been submitted in a paper for publishing. Additional high statistics measurements of linear polarisation observables in double π^0 photoproduction have been presented and are in preparation to be published. Techniques using ${}_s\mathcal{P}lot$ have been developed and are to be applied to recent data to yield similar measurements on the neutron in the near future.

Appendix A

Appendix

A.1 ${}_s\mathcal{P}lot$

The goal of using ${}_s\mathcal{P}lot$ is in disentanglement of desired signal distributions from background sources[104, 122]. This is achieved weighting events by values associated with the desired species, these weights are calculated through fitting PDFs to the distributions of discriminating variables in the data set.

A.1.1 Likelihood Fit

The log-Likelihood expression used to fit the data is given by:

$$\mathcal{L} = \sum_{e=1}^{N} ln \left\{ \sum_{i=1}^{N_s} N_i f_i \left(y_e \right) \right\} - \sum_{i=1}^{N_s} N_i, \tag{A.1}$$

where the terms, and examples, are outlined in table A.1.

Maximising the likelihood $\mathcal{L}$ provides the best estimate of the free parameters in the fit. Parameters left free are species yields N_i.

The likelihood fit is now used by ${}_s\mathcal{P}lot$ to produce an sWeight, associated with each species, for every event. When weighted with the sWeights, the control variable distributions of the signal are effectively disentangled from the control variable

Item	Definition	Examples
e	Event number	
N	Total number of events	
i	Species index	
N_s	Total number of species to fit	3={Signal, Background, Random}
N_i	Yield of events in species i	
f_i	PDF associated with species i	Gaussian, Polynomial, Histogram, Simulated distribution
y	Set of discriminating variables	Missing mass, Timing coincidence
$f_i\left(y_e\right)$	PDF magnitude at values y of event e	
x	Control variables uncorrelated with y	ϕ, θ

Table A.1: Maximum likelihood variables used in ${}_s\mathcal{P}lot$ the fit.

distributions of the other signal species.

A.1.2 sWeight Calculation

The sWeights are calculated from a likelihood fit to a variable which discriminates between different species contributions. The covariance matrix ($\mathbf{V}$) resulting from a fit of the species yields

$$\mathbf{V}_{ij}^{-1} = \frac{\partial^2(-\mathcal{L})}{\partial N_n \partial N_j} = \sum_{e=1}^{N} \frac{f_i(y_e) f_j(y_e)}{\left(\sum_{n=1}^{N_s} N_n f_n(y_e)\right)^2}. \tag{A.2}$$

The covariance matrix is used in the production of the sWeights, ${}_s\mathcal{P}_n\left(y_e\right)$ for each event e and species n, given by:

$${}_s\mathcal{P}_n\left(y_e\right) = \frac{\sum_{j=1}^{N_s} \mathbf{V}_{nj} f_j\left(y_e\right)}{\sum_{k=1}^{N_s} N_k f_k\left(y_e\right)}. \tag{A.3}$$

The proof of this, not reproduced here, is given in reference [104].

A.1.3 sWeight Properties

The sWeights have a number of properties worth noting.

sWeights are not probabilistic weights and so are not restricted between 0 and 1. However the sum of the weights of different species assigned to an event is equal to 1.

$$\sum_{n=1}^{N_s} {}_s\mathcal{P}_n\left(y_e\right) = 1 \tag{A.4}$$

The sum of events weighted by sWeights associated with a species equals the calculated yield of the species.

$$\sum_{e=1}^{N} {}_s\mathcal{P}_s\left(y_e\right) = N_s \tag{A.5}$$

The mean weight of an event associated with a species is equivalent to the average probabilistic weight.

$$\left\langle {}_s\mathcal{P}_s\left(y_e\right)\right\rangle = \frac{N_s}{N} \tag{A.6}$$

The sum of weights from two species is the same as the weight of a combined species.

Bibliography

[1] E. Rutherford. "Collision of α particles with light atoms". In: *Philosophical Magazine* 90.sup1 (1919), pp. 31–37. DOI: 10.1080/14786431003659230.

[2] J. Chadwick. "Possible Existence of a Neutron". In: *Nature* 129 (1932), p. 312. DOI: 10.1038/129312a0.

[3] E. Wigner. "On the Consequences of the Symmetry of the Nuclear Hamiltonian on the Spectroscopy of Nuclei". In: *Phys. Rev.* 51 (2 Jan. 1937), pp. 106–119. DOI: 10.1103/PhysRev.51.106.

[4] M. Gell-Mann. "Isotopic Spin and New Unstable Particles". In: *Phys. Rev.* 92 (3 Nov. 1953), pp. 833–834. DOI: 10.1103/PhysRev.92.833.

[5] Kazuhiko Nishijima. "Charge Independence Theory of V Particles". In: *Progress of Theoretical Physics* 13.3 (1955), pp. 285–304. DOI: 10.1143/PTP.13.285.

[6] Murray Gell-Mann. "Symmetries of Baryons and Mesons". In: *Phys. Rev.* 125 (3 Feb. 1962), pp. 1067–1084. DOI: 10.1103/PhysRev.125.1067.

[7] M. Gell-Mann and Ne'eman Y. "The eightfold way". In: *Nuclear Physics* 79.2 (1966), pp. 477–478. DOI: 10.1016/0029-5582(66)90165-9.

[8] M. Gell-Mann. "A schematic model of baryons and mesons". In: *Physics Letters* 8.3 (1964), pp. 214–215. DOI: 10.1016/S0031-9163(64)92001-3.

[9] G Zweig. "An SU_3 model for strong interaction symmetry and its breaking; Version 2". In: CERN-TH-412 (Feb. 1964). Version 1 is CERN preprint 8182/TH.401 Jan. 17 1964, 80 p. URL: http://cds.cern.ch/record/570209.

[10] O. W. Greenberg and M. Resnikoff. "Symmetric Quark Model of Baryon Resonances". In: *Phys. Rev.* 163 (5 Nov. 1967), pp. 1844–1851. DOI: 10.1103/PhysRev.163.1844.

[11] David Faiman and Archibald W. Hendry. "Harmonic-Oscillator Model for Baryons". In: *Phys. Rev.* 173 (5 Sept. 1968), pp. 1720–1729. DOI: 10.1103/PhysRev.173.1720.

[12] C. P. Forsyth and R. E. Cutkosky. "A quark model of baryons with natural flavor". In: *Zeitschrift für Physik C Particles and Fields* 18.3 (1983), pp. 219–227. DOI: 10.1007/BF01571363.

[13] D. B. Lichtenberg, L. J. Tassie, and P. J. Keleman. "Quark-Diquark Model of Baryons and SU(6)". In: *Phys. Rev.* 167 (5 Mar. 1968), pp. 1535–1542. DOI: 10.1103/PhysRev.167.1535.

[14] Mauro Anselmino et al. "Diquarks". In: *Rev. Mod. Phys.* 65 (4 Oct. 1993), pp. 1199–1233. DOI: 10.1103/RevModPhys.65.1199.

[15] C.P. Forsyth and R.E. Cutkosky. "Evidence against diquarks from baryon resonance decays". In: *Nuclear Physics B* 178.1 (1981), pp. 35–44. DOI: 10.1016/0550-3213(81)90496-X.

[16] S. Capstick and W. Roberts. "Quark models of baryon masses and decays". In: *Progress in Particle and Nuclear Physics* 45 (2000), S241–S331. DOI: 10.1016/S0146-6410(00)00109-5.

[17] Eberhard Klempt and Jean-Marc Richard. "Baryon spectroscopy". In: *Rev. Mod. Phys.* 82 (2 Apr. 2010), pp. 1095–1153. DOI: 10.1103/RevModPhys.82.1095.

[18] St. Goertz, W. Meyer, and G. Reicherz. "Polarized H, D and 3He targets for particle physics experiments". In: *Progress in Particle and Nuclear Physics* 49.2 (2002), pp. 403–489. DOI: 10.1016/S0146-6410(02)00159-X.

[19] Iu. A. Skorodumina et al. "Nucleon resonances in exclusive reactions of photo- and electroproduction of mesons". In: *Moscow University Physics Bulletin* 70.6 (2015), pp. 429–447. DOI: 10.3103/S002713491506017X.

[20] Jannes Nys, Tom Vrancx, and Jan Ryckebusch. "Amplitude extraction in pseudoscalar-meson photoproduction: towards a situation of complete information". In: *Journal of Physics G: Nuclear and Particle Physics* 42.3 (2015), p. 034016. URL: http://stacks.iop.org/0954-3899/42/i=3/a=034016.

[21] C. Patrignani and Particle Data Group. "Review of Particle Physics". In: *Chinese Physics C* 40.10 (2016), p. 100001. URL: http://stacks.iop.org/1674-1137/40/i=10/a=100001.

[22] I. Larin et al. "New Measurement of the π^0 Radiative Decay Width". In: *Phys. Rev. Lett.* 106 (16 Apr. 2011), p. 162303. DOI: 10.1103/PhysRevLett.106.162303.

[23] A. M. Bernstein and Barry R. Holstein. "Neutral pion lifetime measurements and the QCD chiral anomaly". In: *Rev. Mod. Phys.* 85 (1 Jan. 2013), pp. 49–77. DOI: 10.1103/RevModPhys.85.49.

[24] A. Beddall and A. Beddall. "Measurement of the Dalitz-decay branching ratio of the π0". In: *The European Physical Journal C* 54.3 (2008), pp. 365–370. DOI: 10.1140/epjc/s10052-008-0539-0.

[25] T. A. Armstrong et al. "Total Hadronic Cross Section of γ Rays in Hydrogen in the Energy Range 0.265-4.215 GeV". In: *Phys. Rev. D* 5 (7 Apr. 1972), pp. 1640–1652. DOI: 10.1103/PhysRevD.5.1640.

[26] H. Meyer et al. "Total cross section for photoproduction of hadrons on hydrogen and deuterium between 1.0 and 6.4 GeV". In: *Physics Letters B* 33.2 (1970), pp. 189–192. DOI: 10.1016/0370-2693(70)90298-4.

[27] H.G. Hilpert et al. "Total cross section for photoproduction of hadrons on protons up to 5 GeV". In: *Physics Letters B* 27.7 (1968), pp. 474–476. DOI: 10.1016/0370-2693(68)90244-X.

[28] G. Breit and E. Wigner. "Capture of Slow Neutrons". In: *Phys. Rev.* 49 (7 Apr. 1936), pp. 519–531. DOI: 10.1103/PhysRev.49.519.

[29] F.A. Berends, A. Donnachie, and D.L. Weaver. "Photoproduction and electroproduction of pions (I) dispersion relation theory". In: *Nuclear Physics B* 4.1 (1967), pp. 1–53. DOI: 10.1016/0550-3213(67)90196-4.

[30] Nils A. Törnqvist and Matts Roos. "Confirmation of the Sigma Meson". In: *Phys. Rev. Lett.* 76 (10 Mar. 1996), pp. 1575–1578. DOI: 10.1103/PhysRevLett.76.1575.

[31] A. Fix and H. Arenhövel. "Double-pion photoproduction on nucleon and deuteron". In: *The European Physical Journal A - Hadrons and Nuclei* 25.1 (2005), pp. 115–135. DOI: 10.1140/epja/i2005-10067-5.

[32] H. Tanabe and K. Ohta. "Dynamical model for pion photoproduction in the Δ region". In: *Phys. Rev. C* 31 (5 May 1985), pp. 1876–1884. DOI: 10.1103/PhysRevC.31.1876.

[33] I.S. Barker, A. Donnachie, and J.K. Storrow. "Complete experiments in pseudoscalar photoproduction". In: *Nuclear Physics B* 95.2 (1975), pp. 347–356. DOI: 10.1016/0550-3213(75)90049-8.

[34] D. Drechsel, S. S. Kamalov, and L. Tiator. "Unitary isobar model –MAID2007". In: *The European Physical Journal A* 34.1 (2007), pp. 69–97. DOI: 10.1140/epja/i2007-10490-6.

[35] I.S. Barker, A. Donnachie, and J.K. Storrow. "Analysis of π^0 photoproduction at intermediate and high energies". In: *Nuclear Physics B* 79.3 (1974), pp. 431–460. DOI: 10.1016/0550-3213(74)90561-6.

[36] G. F. Chew et al. "Relativistic Dispersion Relation Approach to Photomeson Production". In: *Phys. Rev.* 106 (6 June 1957), pp. 1345–1355. DOI: 10.1103/PhysRev.106.1345.

[37] R. Beck et al. "Determination of the $E2/M1$ ratio in the $\gamma N \to \Delta(1232)$ transition from a simultaneous measurement of $p\gamma \to p\pi^0$ and $p\gamma \to \pi^+ n$". In: *Phys. Rev. C* 61 (3 Feb. 2000), p. 035204. DOI: 10.1103/PhysRevC.61.035204.

[38] J. Ahrens et al. "Helicity Amplitudes $A_{1/2}$ and $A_{3/2}$ for the $D_{13}(1520)$ Resonance Obtained from the $\vec{\gamma}\vec{p} \to p\pi^0$ Reaction". In: *Phys. Rev. Lett.* 88 (23 May 2002), p. 232002. DOI: 10.1103/PhysRevLett.88.232002.

[39] D. Drechsel and M. Vanderhaeghen. "Magnetic dipole moment of the $\Delta^+(1232)$ from the $\gamma\vec{p}\gamma\pi^0 p$ reaction". In: *Phys. Rev. C* 64 (6 Nov. 2001), p. 065202. DOI: 10.1103/PhysRevC.64.065202.

[40] Biplab Dey et al. "Polarization observables in the longitudinal basis for pseudo-scalar meson photoproduction using a density matrix approach". In: *Phys. Rev. C* 83 (5 May 2011), p. 055208. DOI: 10.1103/PhysRevC.83.055208.

[41] W. Roberts and T. Oed. "Polarization observables for two-pion production off the nucleon". In: *Phys. Rev. C* 71 (5 May 2005), p. 055201. DOI: 10.1103/PhysRevC.71.055201.

[42] A. V. Anisovich et al. "Properties of baryon resonances from a multichannel partial wave analysis". In: *The European Physical Journal A* 48.2 (2012), pp. 1–13. DOI: 10.1140/epja/i2012-12015-8.

[43] Darrell J. Drickey and Robert F. Mozley. "Neutral Meson Production with Polarized X Rays". In: *Phys. Rev.* 136 (2B Oct. 1964), B543–B557. DOI: 10.1103/PhysRev.136.B543.

[44] D. Hornidge et al. "Accurate Test of Chiral Dynamics in the $\vec{\gamma}p \to \pi^0 p$ Reaction". In: *Phys. Rev. Lett.* 111 (6 Aug. 2013), p. 062004. DOI: 10.1103/PhysRevLett.111.062004.

[45] R. L. Anderson et al. "High-Energy π^0 Photoproduction from Hydrogen with Unpolarized and Linearly Polarized Photons". In: *Phys. Rev. D* 4 (7 Oct. 1971), pp. 1937–1946. DOI: 10.1103/PhysRevD.4.1937.

[46] R. Beck et al. "Measurement of the $E2/M1$ Ratio in the $N \to \Delta$ Transition using the reaction $p(\vec{\gamma}, p)\pi^0$". In: *Phys. Rev. Lett.* 78 (4 Jan. 1997), pp. 606–609. DOI: 10.1103/PhysRevLett.78.606.

[47] O. Bartalini et al. "Measurement of πphotoproduction on the proton from 550 to 1500 MeV at GRAAL". In: *The European Physical Journal A - Hadrons and Nuclei* 26.3 (2005), pp. 399–419. DOI: 10.1140/epja/i2005-10191-2.

[48] F. V. Adamian et al. "Measurement of the cross section asymmetry of the reaction $\gamma p \rightarrow \pi^0 p$ in the resonance energy region $E_\gamma = 0.5 - 1.1$ GeV". In: *Phys. Rev. C* 63 (5 Apr. 2001), p. 054606. DOI: 10.1103/PhysRevC.63.054606.

[49] D. Elsner et al. "Linearly polarised photon beams at ELSA and measurement of the beam asymmetry in π^0 photoproduction off the proton". In: *The European Physical Journal A* 39.3 (2009), pp. 373–381. DOI: 10.1140/epja/i2008-10708-1.

[50] N. Sparks et al. "Measurement of the beam asymmetry Σ in the forward direction for $\vec{\gamma}p \rightarrow p\pi^0$". In: *Phys. Rev. C* 81 (6 June 2010), p. 065210. DOI: 10.1103/PhysRevC.81.065210.

[51] R. Beck. "Experiments with photons at MAMI". In: *Eur. Phys. J. A* 28.1 (2006), pp. 173–183. DOI: 10.1140/epja/i2006-09-018-1.

[52] G. Audit et al. "DAPHNE: a large-acceptance tracking detector for the study of photoreactions at intermediate energies". In: *Nuclear Instruments and Methods in Physics Research Section A: Accelerators, Spectrometers, Detectors and Associated Equipment* 301.3 (1991), pp. 473–481. DOI: 10.1016/0168-9002(91)90013-G.

[53] R. Crawford et al. "Two-body photodisintegration of the deuteron from 100 to 800 MeV". In: *Nuclear Physics A* 603.3 (1996), pp. 303–325. DOI: 10.1016/0375-9474(96)80004-B.

[54] R. Leukel. "Photoproduktion neutraler Pionen am Proton mit linear polarisierten Photonen im Bereich der $\Delta(1232)$ Resonanz". PhD thesis. Institut für Kernphysik, Mainz, 2001.

[55] J.P. Bocquet et al. "GRAAL: a polarized γ-ray beam at ESRF". In: *Nuclear Physics A* 622.1 (1997), pp. c124–c129. DOI: 10.1016/S0375-9474(97)00337-0.

[56] E. Gutz et al. "High statistics study of the reaction $\gamma p \to p\pi^0\eta$". In: *The European Physical Journal A* 50.4 (2014), pp. 1–27. DOI: 10.1140/epja/i2014-14074-1.

[57] A Braghieri et al. "Total cross section measurement for the three double pion photoproduction channels on the proton". In: *Physics Letters B* 363.1 (1995), pp. 46–50. DOI: 10.1016/0370-2693(95)01189-W.

[58] F. Härter et al. "Two neutral pion photoproduction off the proton between threshold and 800 MeV". In: *Physics Letters B* 401.3 (1997), pp. 229–233. DOI: 10.1016/S0370-2693(97)00423-1.

[59] M. Wolf et al. "Photoproduction of neutral pion pairs from the proton". In: *The European Physical Journal A - Hadrons and Nuclei* 9.1 (2000), pp. 5–8. DOI: 10.1007/s100500070048.

[60] Y. Assafiri et al. "Double π^0 Photoproduction on the Proton at GRAAL". In: *Phys. Rev. Lett.* 90 (22 June 2003), p. 222001. DOI: 10.1103/PhysRevLett.90.222001.

[61] V. Sokhoyan et al. "High-statistics study of the reaction γ p$\to$ p2π0". In: *The European Physical Journal A* 51.8 (2015), pp. 1–29. DOI: 10.1140/epja/i2015-15095-x.

[62] Laget J.M. Murphy L.Y. "Reaction mechanisms in two-pion photoproduction on the proton : I - Meson exchange picture". In: *DAPNIA-SPHN* (95-42) (1995). URL: http://www.iaea.org/inis/collection/NCLCollectionStore/_Public/28/038/28038791.pdf.

[63] J.A. Gómez Tejedor and E. Oset. "Double pion photoproduction on the nucleon: study of the isospin channels". In: *Nuclear Physics A* 600.4 (1996), pp. 413–435. DOI: 10.1016/0375-9474(95)00492-0.

[64] D. Drechsel et al. "A unitary isobar model for pion photo- and electroproduction on the proton up to 1 GeV". In: *Nuclear Physics A* 645.1 (1999), pp. 145–174. DOI: 10.1016/S0375-9474(98)00572-7.

[65] A. Fix. *2π MAID code*. Private Comminication. 2016.

[66] P. Adlarson et al. "Measurement of π^0 photoproduction on the proton at MAMI C". In: *Phys. Rev. C* 92 (2 Aug. 2015), p. 024617. DOI: 10.1103/PhysRevC.92.024617.

[67] W.J. Briscoe, I.I. Strakovsky, and R.L. Workman. *SAID world database*. Data from SAID world database: Last accessed January 2016. URL: http://gwdac.phys.gwu.edu/.

[68] A. V. Anisovich et al. "Photoproduction of pions and properties of baryon resonances from a Bonn-Gatchina partial-wave analysis". In: *The European Physical Journal A* 44.2 (2010), pp. 203–220. DOI: 10.1140/epja/i2010-10950-x.

[69] M. H. Sikora et al. "Measurement of the ${}^1H(\vec{\gamma}, \vec{p})\pi^0$ Reaction Using a Novel Nucleon Spin Polarimeter". In: *Phys. Rev. Lett.* 112 (2 Jan. 2014), p. 022501. DOI: 10.1103/PhysRevLett.112.022501.

[70] K.-H. Kaiser et al. "The 1.5 GeV harmonic double-sided microtron at Mainz University". In: *Nuclear Instruments and Methods in Physics Research Section A: Accelerators, Spectrometers, Detectors and Associated Equipment* 593.3 (2008), pp. 159–170. DOI: 10.1016/j.nima.2008.05.018.

[71] A. Jankowiak. "The Mainz Microtron MAMI –Past and future". In: *The European Physical Journal A - Hadrons and Nuclei* 28.1 (2006), pp. 149–160. DOI: 10.1140/epja/i2006-09-016-3.

[72] M. Dehn et al. "The MAMI C accelerator". In: *The European Physical Journal Special Topics* 198.1 (2011), pp. 19–47. DOI: 10.1140/epjst/e2011-01481-4.

[73] P. Drescher et al. "Photoemission of spinpolarized electrons from strained GaAsP". In: *Applied Physics A* 63.2 (1996), pp. 203–206. DOI: 10.1007/BF01567651.

[74] Y.M. Tsipenyuk and S.P. Kapitza. *The Microtron: Development and Applications*. Taylor & Francis, 2002.

[75] D. Lohmann et al. "Linearly polarized photons at MAMI (Mainz)". In: *Nuclear Instruments and Methods in Physics Research Section A: Accelerators, Spectrometers, Detectors and Associated Equipment* 343.2 (1994), pp. 494–507. DOI: 10.1016/0168-9002(94)90230-5.

[76] H. Bilokon et al. "Coherent bremsstrahlung in crystals as a tool for producing high energy photon beams to be used in photoproduction experiments at CERN SPS". In: *Nuclear Instruments and Methods in Physics Research* 204.2 (1983), pp. 299–310. DOI: 10.1016/0167-5087(83)90061-3.

[77] J.D. Kellie et al. "The selection and performance of diamond radiators used in coherent bremsstrahlung experiments". In: *Nuclear Instruments and Methods in Physics Research Section A: Accelerators, Spectrometers, Detectors and Associated Equipment* 545.1-2 (2005), pp. 164–180. DOI: 10.1016/j.nima.2004.12.042.

[78] D. Howdle. "Measurement of Polarisation Observables using Linearly Polarised Photons with the Crystal Ball at MAMI". PhD thesis. University of Glasgow, United Kingdom, 2012.

[79] J. C. McGeorge et al. "Upgrade of the Glasgow photon tagging spectrometer for Mainz MAMI-C". In: *The European Physical Journal A* 37.1 (2008), pp. 129–137. DOI: 10.1140/epja/i2007-10606-0.

[80] I. Anthony et al. "Design of a tagged photon spectrometer for use with the Mainz 840 MeV microtron". In: *Nuclear Instruments and Methods in Physics Research Section A: Accelerators, Spectrometers, Detectors and Associated Equipment* 301.2 (1991), pp. 230–240. DOI: 10.1016/0168-9002(91)90464-2.

[81] S.J Hall et al. "A focal plane system for the 855 MeV tagged photon spectrometer at MAMI-B". In: *Nuclear Instruments and Methods in Physics Research Section A: Accelerators, Spectrometers, Detectors and Associated Equipment* 368.3 (1996), pp. 698–708. DOI: 10.1016/0168-9002(95)00661-3.

[82] F. Rambo et al. "Enhancement of the linear polarization of coherent bremsstrahlung by collimation of the photon beam". In: *Phys. Rev. C* 58 (1 July 1998), pp. 489–501. DOI: 10.1103/PhysRevC.58.489.

[83] J. Mancell. "A Study of η Photoproduction on the Proton at MAMI". PhD thesis. University of Glasgow, United Kingdom, 2012.

[84] M. Oreglia et al. "Study of the reaction $\psi' \to \gamma\gamma\frac{J}{\psi}$". In: *Phys. Rev. D* 25 (9 May 1982), pp. 2259–2277. DOI: 10.1103/PhysRevD.25.2259.

[85] E D Bloom and C W Peck. "Physics with the Crystal Ball Detector". In: *Annual Review of Nuclear and Particle Science* 33.1 (1983), pp. 143–198. DOI: 10.1146/annurev.ns.33.120183.001043.

[86] A. Starostin et al. "Measurement of $K^-\vec{p}\eta\Lambda$ near threshold". In: *Phys. Rev. C* 64 (5 Oct. 2001), p. 055205. DOI: 10.1103/PhysRevC.64.055205.

[87] M. J. Oregelia. "A study of the reactions $\psi' \to \gamma\gamma\psi$". PhD thesis. SLAC, USA, 1980.

[88] M.H. Sikora. "Coherent π^0 Photoproduction on Nuclei". PhD thesis. University of Edinburgh, United Kingdom, 2011.

[89] A.R. Gabler et al. "Response of TAPS to monochromatic photons with energies between 45 and 790 MeV". In: *Nuclear Instruments and Methods in Physics Research Section A: Accelerators, Spectrometers, Detectors and Associated Equipment* 346.1 (1994), pp. 168–176. DOI: 10.1016/0168-9002(94)90701-3.

[90] R. Novotny. "The BaF2 spectrometer taps: A system for high energy photon and neutral meson detection". In: *Nuclear Tracks and Radiation Measurements* 21.1 (1993), pp. 23–26. DOI: 10.1016/1359-0189(93)90039-C.

[91] R Novotny et al. "Scintillators for photon detection at medium energies-a comparative study of BaF2, CeF3 and PbWO4". In: *Nuclear Instruments and Methods in Physics Research Section A: Accelerators, Spectrometers, Detectors and Associated Equipment* 486.1-2 (2002). Proceedings of the 6th International Conference on Inorganic Scintillators and their Use in Scientific and

Industrial Applications, pp. 131–135. DOI: 10.1016/S0168-9002(02)00689-7.

[92] C. Collicott. "Probing proton structure through single polarisation observables of compton scattering and π^0 photoproduction within the $\Delta(1232)$ region". PhD thesis. Dalhousie University Halifax, Canada, 2015.

[93] DI Glazier. *A Geant4 Simulation of the Crystal Ball@ MAMI Setup*. 2012.

[94] S. Agostinelli et al. "Geant4-a simulation toolkit". In: *Nuclear Instruments and Methods in Physics Research Section A: Accelerators, Spectrometers, Detectors and Associated Equipment* 506.3 (2003), pp. 250–303. DOI: 10.1016/S0168-9002(03)01368-8.

[95] J. Allison et al. "Geant4 developments and applications". In: *IEEE Transactions on Nuclear Science* 53.1 (Feb. 2006), pp. 270–278. DOI: 10.1109/TNS.2006.869826.

[96] H. Berghäuser. "Determination of the formfactor of the eta". PhD thesis. Justus-Liebig-Universität, Gießen, 2010.

[97] U. Timm. "Coherent Bremsstrahlung of Electrons in Crystals". In: *Fortschritte der Physik* 17.12 (1969), pp. 765–808. DOI: 10.1002/prop.19690171202.

[98] G. R. Stewart. "Measurement of low-temperature specific heat". In: *Review of Scientific Instruments* 54.1 (1983), pp. 1–11. DOI: 10.1063/1.1137207.

[99] Ken Livingston. "The Stonehenge technique. A method for aligning coherent bremsstrahlung radiators". In: *Nucl. Instrum. Methods A* 603.3 (2009), pp. 205–213. DOI: 10.1016/j.nima.2009.02.010.

[100] F.A Natter et al. "Monte Carlo simulation and analytical calculation of coherent bremsstrahlung and its polarisation". In: *Nuclear Instruments and Methods in Physics Research Section B: Beam Interactions with Materials and Atoms* 211.4 (2003), pp. 465–486. DOI: 10.1016/S0168-583X(03)01420-4.

[101] K. Livingston. *Polarization from Coherent Bremsstrahlung Enhancement*. 2011. URL: http://nuclear.gla.ac.uk/~clasg8/CbremJlab/enhFitting.html.

[102] D.I. Glazier et al. "Angular distribution of coherent bremsstrahlung". In: *Nuclear Instruments and Methods in Physics Research Section A: Accelerators, Spectrometers, Detectors and Associated Equipment* 664.1 (2012), pp. 132–139. DOI: 10.1016/j.nima.2011.10.053.

[103] Strakovsky. I. *SAID Errors*. Private Comminication. 2016.

[104] M. Pivk and F.R. Le Diberder. "sPlot: A statistical tool to unfold data distributions". In: *Nuclear Instruments and Methods in Physics Research Section A: Accelerators, Spectrometers, Detectors and Associated Equipment* 555.1-2 (2005), pp. 356–369. DOI: 10.1016/j.nima.2005.08.106.

[105] J.R.M. Annand. *Data analysis within an AcquRoot Framework*. 2005. URL: http://www.nuclear.gla.ac.uk/~acqusys/doc/AcquRoot.11.08.pdf.

[106] Rene Brun and Fons Rademakers. "ROOT - An object oriented data analysis framework". In: *Nuclear Instruments and Methods in Physics Research Section A: Accelerators, Spectrometers, Detectors and Associated Equipment* 389.1 (1997), pp. 81–86. DOI: 10.1016/S0168-9002(97)00048-X.

[107] I. Antcheva et al. "ROOT - A C++ framework for petabyte data storage, statistical analysis and visualization". In: *Computer Physics Communications* 180.12 (2009). 40 YEARS OF CPC: A celebratory issue focused on quality software for high performance, grid and novel computing architectures, pp. 2499–2512. DOI: 10.1016/j.cpc.2009.08.005.

[108] S. Gardner et al. "Photon asymmetry measurements of $\overrightarrow{\gamma}p \to \pi^0 p$ for $E_\gamma =$ 320-650 MeV". In: *The European Physical Journal A* 52.11 (2016), p. 333. DOI: 10.1140/epja/i2016-16333-5.

[109] S. S. Kamalov et al. "Recent results from the MAID and Dubna-Mainz-Taipei PWA analysis". In: *NSTAR 2007: Proceedings of The 11th Workshop on The Physics of Excited Nucleons, 5–8 September 2007, Bonn, Germany*. Ed. by Hans-Werner Hammer et al. Berlin, Heidelberg: Springer Berlin Heidelberg, 2008, pp. 115–120. DOI: 10.1007/978-3-540-85144-8_21.

[110] R.A. Arndt, I.I. Strakovsky, and R.L. Workman. "The Said PWA Program". In: *International Journal of Modern Physics A* 18.3 (2003), pp. 449–456.

[111] A.A. Belyaev et al. "Experimental studies of the Σ, T, P polarization parameters and the $\gamma p \to p\pi^0$ reaction multipole analysis in the first resonance region". In: *Nuclear Physics B* 213.2 (1983), pp. 201–222. DOI: 10.1016/0550-3213(83)90509-6.

[112] G. Blanpied et al. "$\vec{N}\Delta$ transition and proton polarizabilities from measurements of $p(\vec{\gamma},\gamma)$, $p(\vec{\gamma},\pi^0)$, and $p(\vec{\gamma},\pi^+)$". In: *Phys. Rev. C* 64 (2 July 2001), p. 025203. DOI: 10.1103/PhysRevC.64.025203.

[113] G. Barbiellini et al. "Photoproduction of π^0 on Protons by Polarized γ Rays". In: *Phys. Rev.* 184 (5 Aug. 1969), pp. 1402–1413. DOI: 10.1103/PhysRev.184.1402.

[114] R. W. Zdarko and E. B. Dally. "Asymmetry measurements for π^0 and π^+ photoproduction by linearly polarized γ-rays in the energy range (400→900) MeV". In: *Il Nuovo Cimento A (1971-1996)* 10.1 (1972), pp. 10–18. DOI: 10.1007/BF02895969.

[115] VG Gorbenko et al. "Measurement of recoil-proton polarization in the reaction $\gamma p \to \pi^0 p$ with polarized photons at energies 360, 400, 450, and 500 MeV". In: *Sov. J. Nucl. Phys.(Engl. Transl.);(United States)* 27.5 (1978), p. 1204.

[116] VG Gorbenko et al. "Double polarization experiment in investigation of the reaction $\gamma p \to \pi^0 p$ with a beam of linearly polarized photons". In: *Sov. J. Nucl. Phys.(Engl. Transl.);(United States)* 26.2 (1977), p. 167.

[117] VG Gorbenko et al. "Proton polarization from the γ+ p2̆192 π 0+ p reaction on a linearly-polarized photon beam". In: (1974).

[118] G. Knies et al. "Measurement of asymmetries in polarized $\gamma N \to \pi N$, with E_γ from 600 to 900 MeV". In: *Phys. Rev. D* 10 (9 Nov. 1974), pp. 2778–2784. DOI: 10.1103/PhysRevD.10.2778.

[119] Y. Wunderlich et al. *Determining the dominant partial wave contributions from angular distributions of single- and double-polarization observables in pseudoscalar meson photoproduction*. arXiv: 1611.01031 [physics.data-an].

[120] M. Dugger et al. "Beam asymmetry Σ for π^+ and π^0 photoproduction on the proton for photon energies from 1.102 to 1.862 GeV". In: *Phys. Rev. C* 88 (6 Dec. 2013), p. 065203. DOI: 10.1103/PhysRevC.88.065203.

[121] Wunderlich. Y and R. Beck. ℓ_{max} *fit*. Private Comminication. 2016.

[122] Yuehong Xie. *sFit: a method for background subtraction in maximum likelihood fit*. arXiv: 0905.0724 [physics.data-an].